Coating of Macroporous Materials with Graphitic Carbon Nitrides: New Materials for Visible Light Photocatalysis

Sha Qiao

MSc by Research

University of York
Chemistry

January 2014

Abstract

Solar energy conversion is significant to future energy needs if current challenges can be overcome. Photocatalysis of water to H_2 and O_2 is one solar energy technology that could be used if the efficient conversion from light to chemical fuel (hydrogen and oxygen) could be achieved. However, many photocatalysts can only utilise ultraviolet light, degrade under illumination, mediate only oxidation or reduction, or are too costly.

Some metal silicides have a narrow range of band gap energy, allowing the absorption of visible light and they have been suggested as photocatalysts for hydrogen generation without a sacrificial reductant. A report describes inexpensive commercial $TiSi_2$ as a photocatalyst for water splitting operating under visible light. However in our hands we did not observe *catalytic* formation of hydrogen. We found that $TiSi_2$ undergoes photocorrosion under visible light to give substoichiometric amounts of hydrogen.

There are many reports of graphitic carbon nitride (g-C_3N_4) acting as a stable visible-light-driven photocatalyst for H_2 generation using a sacrificial reductant. A limitation is the surface area of bulk g-C_3N_4. To increase the active surface area, we have coated carbon nitride (CN) onto macroporous (3DOM) SiO_2 and ZrO_2 by thermal polymerisation of cyanamide. A range of loadings have been obtained and the products characterised using SEM, TEM, PXRD, BET, FT-IR, UV-vis, SSNMR and, then for the SiO_2 composites, tested for photocatalytic hydrogen production. It has been found that the in common with bulk (g-C_3N_4) the true composition contains hydrogen due to incomplete polymerisation of cyanamide and overall is closer to C_2N_3H. Nevertheless the composites show excellent activity for hydrogen production which is over 20 times greater in comparison to the bulk material. The sample with 6.6% C_xN_y by mass shows the best performance for H_2 evolution. The increase in activity can largely be attributed to the increase in surface area.

Contents

List of Figures

Chapter 1

Chapter 2

List of Tables

Acknowledgements

First of all, I would like to express my great gratitude to my supervisor Dr. Richard E Douthwaite for his kind help and patient guidance throughout this year. His advice and support towards the problem solving and experimental work made me gain a lot, not only in terms of knowledge, but also scientific way of thinking.

I would also like to thank my mentor Menglong Zhang, for his kindly care in both of my life and study. He usually discussed with me about the difficulties in lab and gave me suggestions. His help made me eased in the lab, especially in the first a few months.

Moreover, I want to thank my research group mate Robert Mitchell. He offered considerable help on my research and brought me inspirations. I also appreciate Natalie Pridmore for her patient guidance and warm care. Also thanks to Danielle Jowett and Nathan Allen for the help of lab issues. When I had questions, they were always there to help and answered in enthusiasm.

Furthermore, I would like to thank Ian Wright for his training and kind help with operating the SEM. Thanks to Adrain Whitwood for the training of PXRD. Also thanks to Graeme Mcallister for offering support to the CHN combustion elemental analysis. Also EPSRC National Solid-State NMR service at Durham for solid-state NMR test and Institute of Materials Research, University of Leeds for the elemental mapping.

Finally, I want to give thanks to my friends and family who gave me spiritual support and enlightened me when I was in depression. It is their company that makes this year of my life smooth and meaningful.

Author's Declaration

I certify that the work presented in this thesis was conducted by myself at the University of York, and I am the sole author.

This work has not previously been presented for any other award at any other institute. All sources are acknowledged as References.

Introduction

Chapter 1

1.1 Solar Energy Conversion and the Energy Crisis

As the world's population grows and develops, more energy is consumed, especially fossil fuels like coal and oil. Consequently, large amounts of greenhouse gas and hazardous substance are emitted, which causes seriously harmful effects on the ecosystem and humanities' well-being. In addition, the overall reserves of fossil fuels are limited. It is estimated that oil utilisation can only be maintained for no more than 80 years and that of coal for no more than 300 years. Therefore, it is of great urgency to develop clean and renewable energy sources.

Solar energy, as a clean and widespread alternative, has been given great attention worldwide. Numerous applications have been developed, such as solar concentrators, photovoltaic (solar) cells, and dye-sensitized solar cells, which directly convert photons to electricity. However, solar energy is provided inconsistently and is diurnal so that energy storage is needed. Additionally, the cost of high purity silicon for solar cells is high, although with continuous mass production the price continues to fall.[1]

Whilst several storage methods have been proposed such as batteries and pumping water uphill, storage of energy in chemical bonds (solar fuels) is one of the most attractive, because it is potentially cheap and environmentally benign. The two reactions that have attracted the most attention are reduction of carbon dioxide to formic acid or methanol, and the decomposition of water to hydrogen and oxygen. The latter reaction is the focus of this work.

Conventionally, the water splitting reaction is achieved by electrolysis. However, this

route is very expensive since the electricity consumed is more than the energy stored in the product. As a result, photocatalytic water splitting has become a promising alternative. With the development of photocatalytic research in the past thirty years, hydrogen has become a promising option to store solar energy.

Hydrogen energy possesses a variety of benefits. To start with, it is a completely clean energy. Since the combustion product is water, the pollution level is approaching zero. Moreover, its energy storage is quite high. The energy density of hydrogen is 2.68 times as much as that of petrol in weight. Furthermore, hydrogen is easily transported. Compared with other sources, when the same amount of energy is transported, hydrogen makes the least loss.[2]

However, some drawbacks should be noted as well. Hydrogen is a permanent gas, the storage and transportation becomes an issue. Hydrogen is flammable and the safety in the storage and transportation is a technological challenge.

1.2 Basic Principles of Semiconductor-Based Photocatalytic Water Splitting

Semiconductor-based materials occupy a large proportion of the photocatalysts for both pollutant degradation and hydrogen evolution. The band structure of a semiconductor is shown in Fig. 1.1. In a semiconductor, the energy levels are divided into a valence and a conduction band. The electrons exist in the valence band under normal conditions. When external stimulation such as electric field and light is applied to the semiconductor, electrons can be excited to the conduction band, and act as charge carriers with the positive hole in the valence band, respectively. The energy between the conduction band and valence band is called the band gap (E_g).

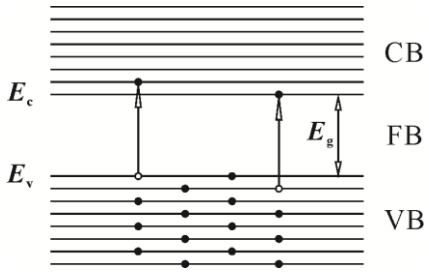

Figure 1.1: Band structure of a semiconductor at a certain temperature, when electrons from the valence band are excited to the conduction band. CB, FB and VB represent conduction, forbidden and valence band, respectively. E_c and E_v refer to the energy at the bottom of conduction band and the top of valence band, respectively. E_g is the band gap energy.[3]

1.2.1 The Discovery of Photocatalytic Water-Splitting

The phenomenon of hydrogen generation from water splitting was first discovered by Fujishima and Honda in 1971, using a monocrystal n-type TiO_2 photoelectrode, as shown in Fig. 1.2.[4] The relevant reactions are shown in Equation 1.1-1.3.

Cathode: $2H^+ + 2e^- = H_2$ E^{Θ}=0 (1.1)

Anode: $2H_2O = O_2 + 4H^+ + 4e^-$ E^{Θ}=1.23eV (1.2)

Overall reaction: $2H_2O = 2H_2 + O_2$ ΔG^0=+237 kJ/mol (1.3)

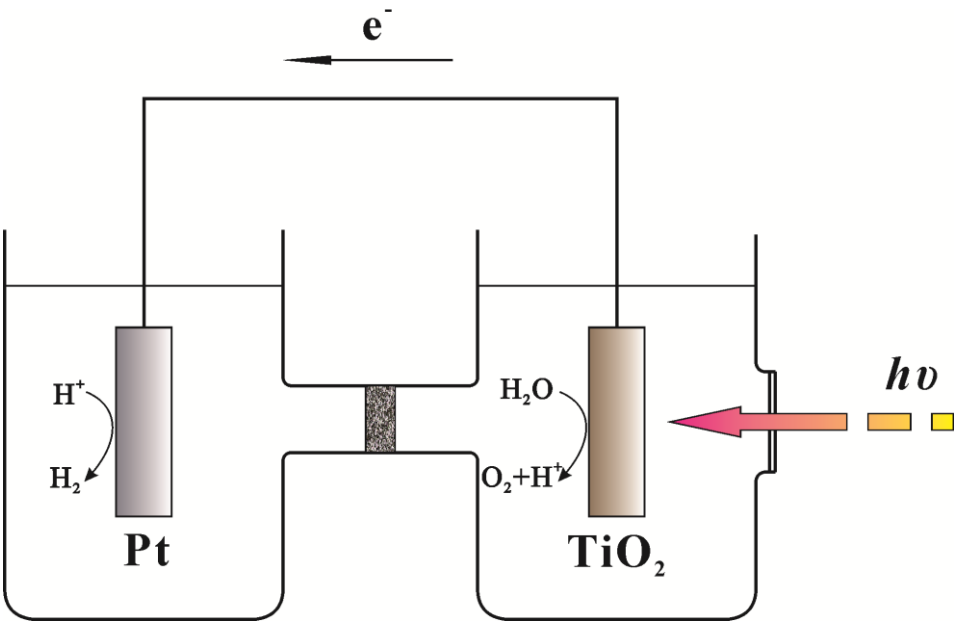

Figure 1.2: Scheme of photoelectrochemical solar cell in Fujishima and Honda's experiment.[4, 5]

In Fujishima and Honda's work, the TiO_2 electrode was irradiated by ultraviolet (UV) light and mediated the oxidation (anodic) reaction. Thus oxygen was produced on the TiO_2 electrode. Meanwhile, hydrogen generation occurred as a result of the reduction on a Pt electrode.[4] As shown in Fig. 1.1, a semiconductor catalyst is irradiated by a certain wavelength range of light. If the energy were equal to or greater than E_g, the electrons in the valence band would be excited to the conduction band, and the hole left in the valence band would become positive. Therefore, electron-hole pairs are formed, and then separate and migrate to the surface of the Pt and TiO_2 catalyst, performing the reduction and oxidation reactions, respectively.

1.2.2 Main Steps of a Photocatalytic Water-Splitting Reaction

Generally, there are three main steps in a photocatalytic reaction of water splitting, as shown in Fig. 1.3. First of all, photons are absorbed by photocatalysts to form electron-hole pairs. To excite electrons to the conduction band, the energy of photons should be higher than the band gap of the photocatalyst. The band gap of a photocatalyst can be equated to the wavelength of irradiation by Equation 1.4.

$$\mathrm{E(band\ gap)(eV)} = \mathrm{h}\nu = \mathrm{hc}/\lambda \approx \frac{1240}{\lambda}(nm) \qquad (1.4)$$

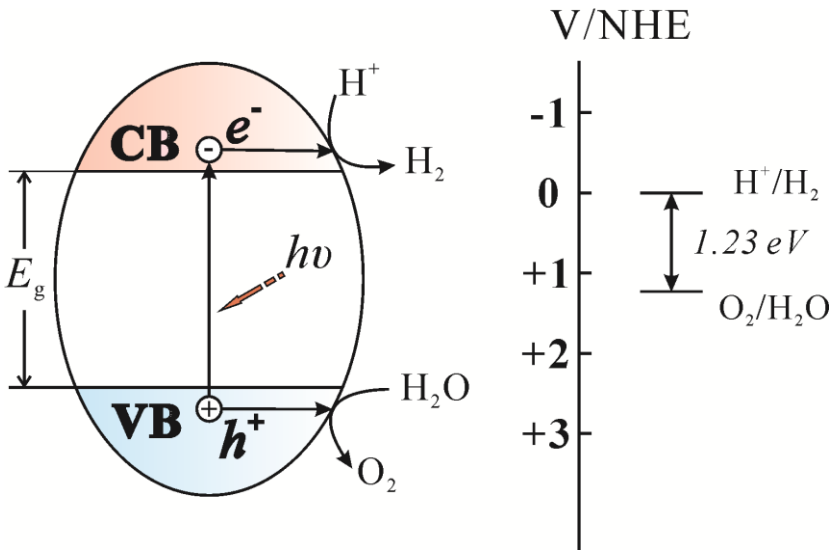

Figure 1.3: Scheme illustration of hydrogen generation by photocatalytic water splitting.[5]

Most research on photocatalytic hydrogen evolution focused on visible light utilisation. Since ultraviolet (UV) accounts for a mere 5% of the solar light incident at the surface of the earth, it is important to adjust the band gap structure to match the wavelength of visible light.

Secondly, the charge carriers should separate and migrate to the surface of photocatalysts to undergo chemical reactions, and the recombination of excited electron-holes pairs on the bulk and surface should be minimised. In this step, the efficiency is related to the crystallinity and the particle size.[6] In the process of the migration, defects in the crystal can trap the charge carriers and act as recombination centres.[6] As a result, by reducing bulk defects, the photocatalytic activity can be increased. Small particles such as materials with nanoscale structures help raise the activity. Since it takes less time and shorter route for charge carriers to migrate to the surface, the rate of recombination can be reduced.

Finally, the available electrons and holes should selectively perform chemical reactions on the surface, acting as reduction and oxidation agent respectively. In this step, the active sites and surface area play important roles.[6] The photocatalytic activity increased with increasing active sites and surface area. Cocatalyst can also introduce active sites when the photocatalyst is not capable to producing hydrogen or oxygen.[6]

1.2.3 Requirements for Efficient Photocatalysts

For visible-light driven photocatalytic water-splitting, the band gap should be between 3.0 and 1.23 eV (400~1000 nm).[5] Because water splitting is an up-hill (endoenergetic) reaction, the energy absorbed has to be greater than ΔG^0 (1.23 eV). In order to use visible light, the wavelength of light should be above 400 nm (3.0 eV). To achieve a complete water-splitting reaction, the band structure of the photocatalyst should be suitable. Specifically, the bottom of the conduction band (E_c) should be more negative

than 0 eV vs NHE while the top of the valence band (E_v) should be more positive than 1.23eV vs NHE, otherwise hydrogen or oxygen would not be produced, respectively.[7] In addition, the back reaction of H_2 and O_2 to form water should be suppressed by either physically separating the products or using catalysts that do not catalyse this reaction.[6]

For an efficient photocatalyst, it should ideally possess a number of demanding physical and chemical properties, which include thermal and chemical stability, inertness in water, alcohol and various pH environments, photocorrosion resistance, high visible light harvesting efficiency and long life-time of electron-hole pairs.

To date, a large number of photocatalysts have been intensively studied for photocatalytic reactions including water splitting, environmental remediation (particularly water), and organic synthesis. Common materials for photocatalytic water splitting reaction are the binary oxide and chalcogenides such as TiO_2,[4] WO_3,[8] Nb_2O_5,[9, 10] Ta_2O_5,[11] ZrO_2,[12] and CdS.[13] Among them, TiO_2 is the most typical oxide, which is stable in aqueous solutions and can be prepared with high surface area.[14, 15] However, since its band gap is 3.2 eV, pure TiO_2 cannot be used under visible light. However, Ta_2O_5 cannot produce O_2 from pure water, but the efficiency of Ta_2O_5 can be improved with NiO or RuO_2 acting as cocatalysts.[16] WO_3 is a good material for photocatalysis, but H_2 cannot be produced using it, because the conduction band is at too high a potential.[5] CdS has narrow band gap and high efficiency of photocatalysis, however the photocorrosion of CdS is serious and significantly affects the lifetime of the catalyst.[6]

Hydrogen generation from water splitting with photocatalysts is likely to have a broad prospect of application, but so far the limited efficiency makes it far from economically viable. A number of approaches have been made to improve the efficiency, such as

heterogeneous composites, constructing special structure materials, optimising synthesis procedure, and searching for new photocatalyst materials.

1.2.4 Cocatalysts and Sacrificial Agent

With a view to reducing the photogenerated charge recombination, cocatalysts are used to trap electrons, so that the charge carriers can be separated efficiently.[5] Furthermore, for the two half reactions of water splitting, loading cocatalyst can lower the energy barriers.[17] For example, it is reported that the photocatalytic activity of graphitic carbon nitride (g-C_3N_4) can be greatly enhanced by adding Pt cocatalyst, but it cannot eliminate O_2. Using RuO_2 instead of Pt, both of two half reactions of water splitting can be achieved.[18] Transition metals (e.g. Pt) and their oxides (e.g. RuO_2 and NiO) are usually employed as cocatalysts.[5] Fig. 1.4 shows the process of the charge carriers transferring between the surface of semiconductor and the Pt cocatalyst.[5]

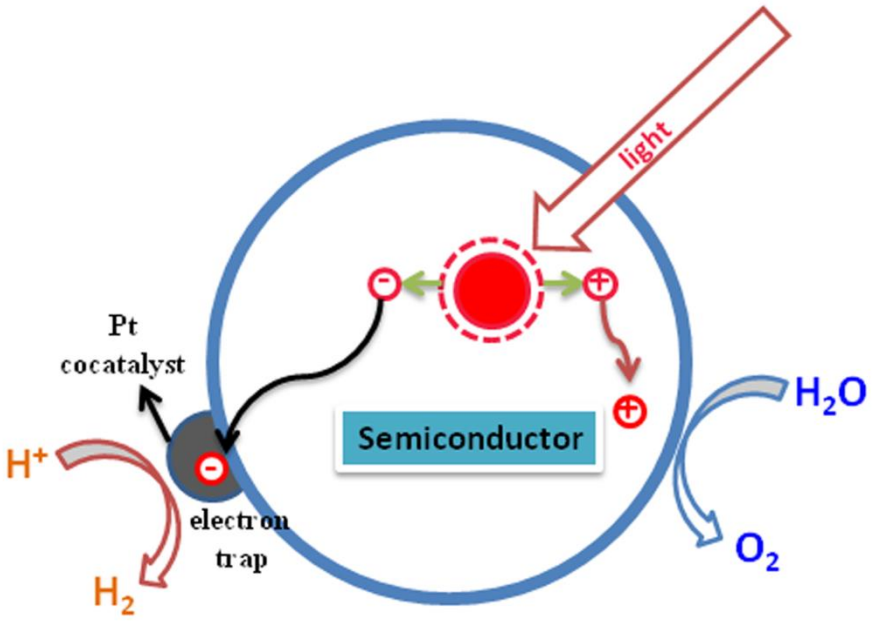

Figure 1.4: The scheme of charge carries transferring to the semiconductor and cocatalyst. Pt is taken as an example.[5]

In many cases sacrificial agents are used as electron donors or acceptors for water splitting reaction, to investigate the potential of a material for a half reaction (H_2 or O_2 production).[5] Fig. 1.5 shows the mechanism of the two half reactions in the presence

of sacrificial agent. In the presence of a sacrificial reductant, the positive holes oxidise the sacrificial reagent irreversibly rather than water.[5] Among the sacrificial agents, S^{2-}/SO_3^{2-} system, methanol and triethanoalamine(TEA) are the most widely used.

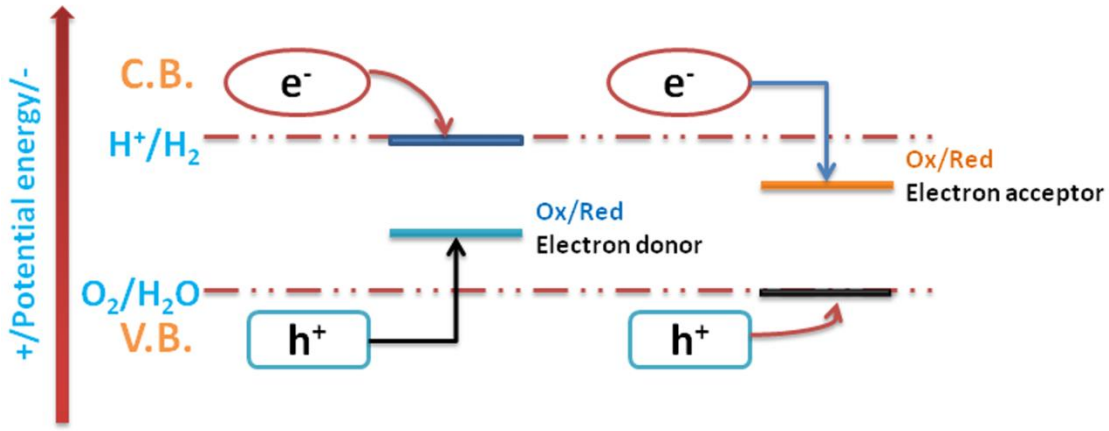

Figure 1.5: The mechanism of two half reactions in the presence of sacrificial agents.[5, 19]

1.3 Increasing the Efficiency of Water-Splitting

In order to enhance the efficiency of the water splitting reaction, a variety of measures are taken to control band gap structure, especially in heterogeneous composites, e.g. modification with metal and non-metal ions and making solid solution between narrow and wide band gap semiconductors.[20] By doping a wide band gap material can be modified to absorb visible light.[21] Impurity levels are introduced into the band gap through metal ion doping (e.g. V, Ni, Cr, Mo, Fe, Sn, Mn),[22-25] whereas non-metal ion doping (e.g. C, N, S) moves the valence band edge upward.[26] Furthermore, forming solid solutions is another promising approach. By adjusting the ratio of the materials, in principal, the desired band gap structure can be achieved.[22]

Other strategies include controlling the morphology of materials to increase active surface area and reduce electron-hole recombination. This is the strategy taken in this thesis, where the aim is to coat a non-metal photocatalyst g-C_3N_4 onto macroporous SiO_2 and ZrO_2, to increase the active surface area of the photocatalytically active materials.

1.3.1 Carbon-Based Materials for Photocatalysis

Nanotubes: Carbon nanotubes (CNT's) are nano-scale graphitic carbons, discovered by Iijima[27] in 1991. Since their discovery, intensive research has been focused on them because of the outstanding electrical and mechanical properties.[26, 28] Baughman *et al.*[28] reviewed two main types of carbon nanotubes, single-walled nanotubes (SWNTs) and multi-walled nanotubes (MWNTs). For photovoltaic and photocatalytic applications, the delocalised π-electron system within the CNT contributes to charge transfer and transportation when combined with other materials, e.g. nanoparticles, as electron donors.[29] Some metals, such as Au, Pt, Ru, Ag etc., have been loaded on CNT as catalysts.[30-32] Lee and Sigmund[30] successfully formed anatase phase TiO_2 nanoparticles with the size range of 2 to 10 nm onto CNTs in aqueous media. Most research focuses on the applications of photocatalytic degradation and solar cells, but few of them study the hydrogen generation. Dai *et al.*[33] reported a nanocomposite photocatalyst of Pt/MWNT-TiO_2, which can produce hydrogen under visible light (Fig.1.6).

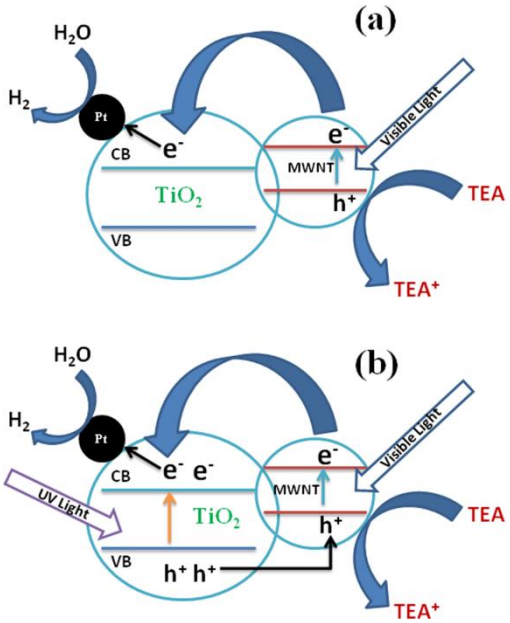

Figure 1.6: Schematic illustration of the mechanism of MWNT-TiO_2 for photocatalytic H_2 evolution in the presence of TEA (triethanolamine) as a sacrificial agent under (a) visible light or (b) the full spectrum of a Xe-lamp. MWNT represents multi-walled carbon nanotube. VB and CB refer to valance band and conduction band, respectively.[33]

Graphene: Graphene, a two-dimensional crystal of hybrised carbon, has been considered as one of the most promising nano-scale materials because of its thermal stability, large surface area, strong adsorptivity, and excellent electrical conductivity. It was first discovered by Geim and Novoselov in 2004.[34] Graphene has been employed in a variety of research fields, such as electronics, super capacitors, chemical and biological sensing, photocatalysis and photovoltaics, becoming a hot topic in physics, chemistry and material science.[35-37] For example, Li *et al.*[38] has reported that CdS-cluster-decorated graphene nanosheets become efficient photocatalysts for hydrogen evolution which absorb visible light, and the surface area of CdS clusters can be promoted by the graphene nanosheets, resulting in an enhancement in the photocatalytic activity with a high H_2-production rate of 1.12 mmol h^{-1}. Xiang *et al.*[39] prepared the TiO_2/MoS_2/graphene composite by a two-step hydrothermal process, and a high H_2 production rate was obtained.

1.3.2 Graphitic Carbon Nitrides for Visible Light Driven Hydrogen Evolution

Apart from "pure" carbon materials, and of direct relevance to this thesis, carbon nitrides have also become an appealing alternative for energy conversion and storage, catalysis and photocatalysis, and the electronics industry.[40] Graphitic carbon nitride (g-C_3N_4) is a two-dimensional sheet consisting of tri-s-triazine groups (Fig.1.7 (b)), and is the most stable allotrope. Fig. 1.7(a) and (b) illustrates two different units consisting of g-C_3N_4.

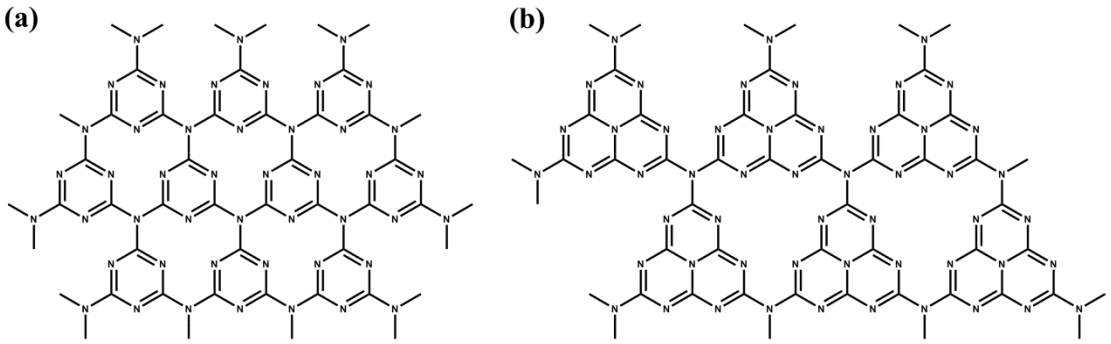

Figure 1.7: Scheme of (a) triazine and (b) tri-*s*-triazine based connection in g-C_3N_4.[18]

It has been reported that g-C_3N_4 can be used as an efficient photocatalyst for hydrogen evolution under visible light.[18] The graphitic phase is more stable than the other allotropes of polymeric C_3N_4 under ambient conditions.[18] The band structure of g-C_3N_4 is shown in Fig 1.8. As can be seen from the scheme, g-C_3N_4 possesses the required band positions of the valence and conduction band (VB=1.4eV, CB=-1.3eV vs NHE, pH=7).[41] The band gap of g-C_3N_4 is 2.7eV, which is in the visible light range. The UV-vis diffuse absorbance spectrum is shown in Fig. 1.9.

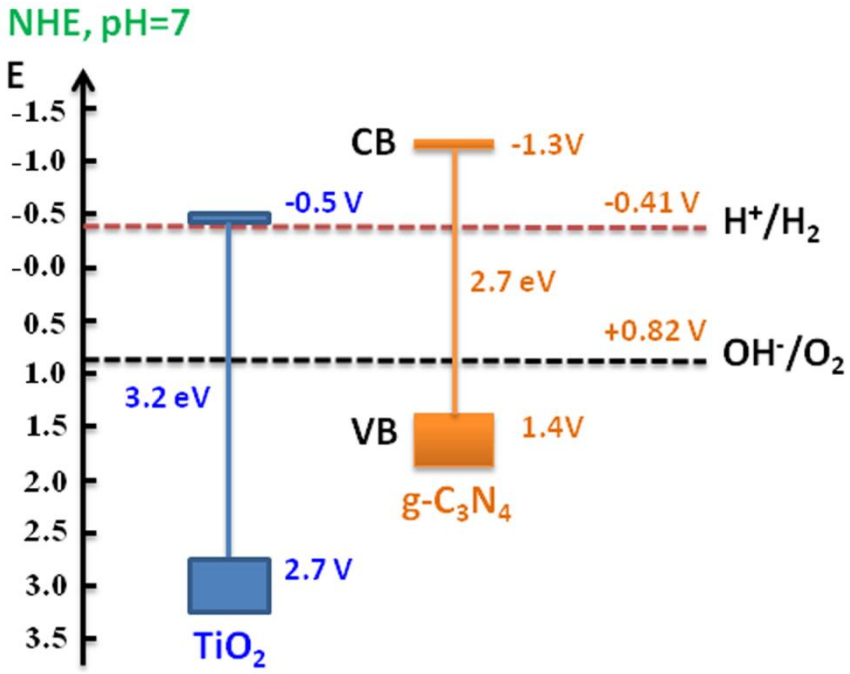

Figure 1.8: The band energies of g-C_3N_4 and TiO_2, a relative to the redox reactions of water and photoemission energies.[42]

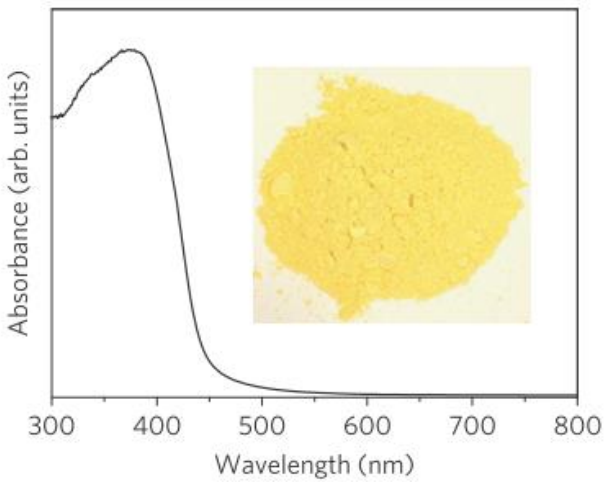

Figure 1.9: UV-vis diffuse reflectance spectrum of the g-C_3N_4 in Wang's work. Inset is the photograph of the synthesised g-C_3N_4.[18]

The synthesis of polymeric carbon nitride was first achieved by Berzelius and Liebig in 1834.[43] Since then research has focused on the synthesis of g-C_3N_4 using a variety of methods. Among them, an easy and efficient way is the pyrolysis of nitrogen-rich precursors. Preparation of high-quality g-C_3N_4 by directly heating precursors such as cyanamide and dicyandiamide was described by Thomas and Antonietti *et al.*[44-46] The polycondensation procedure occurs as follows: 1) at about 240 ^{o}C, the precursors condense to melamine; 2) at about 390 ^{o}C, melamine reorganises to melem, with the release of ammonia; 3) furthermore, the melem condenses to melon, eliminating more ammonia; 4) at around 520 ^{o}C, g-C_3N_4 sheets are formed by polymerisation of melon groups, as shown in Fig. 1.10.[44]

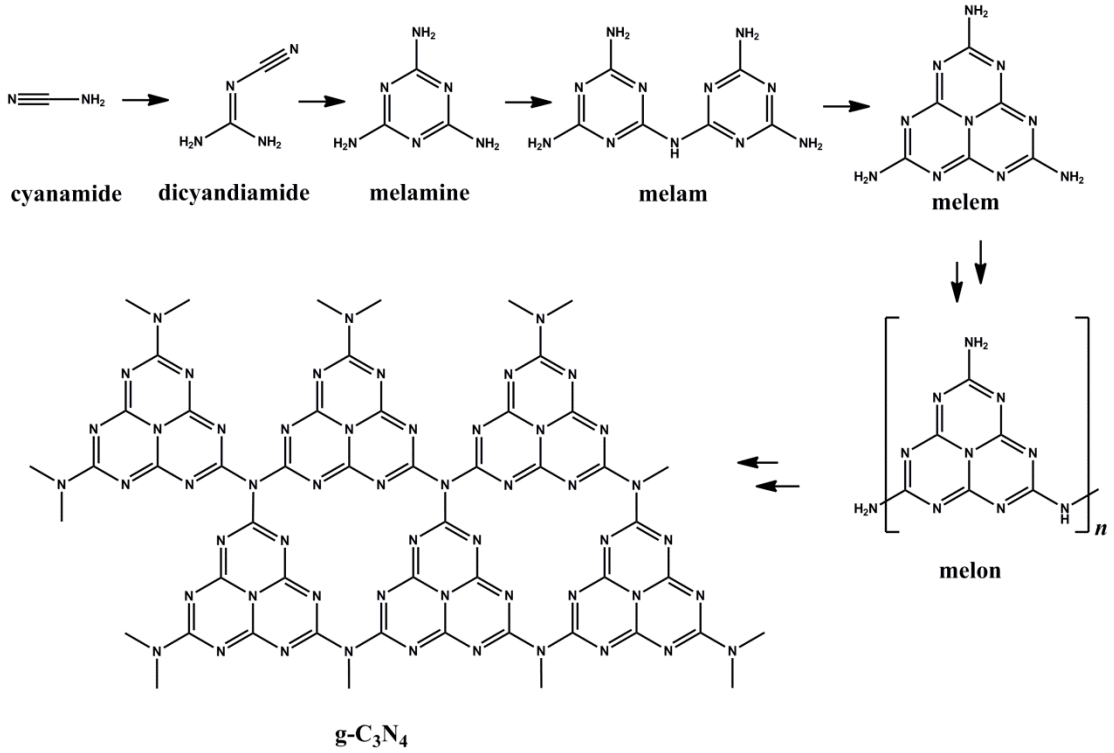

Figure 1.10: Procedure of polymerization starting from cyanamide.[46]

However, there are some drawbacks of this method. First of all, the high volatility of the nitrogen-rich precursors reduces the yield, especially cyanamide (melting point 42 ^{o}C, boiling point 70 ^{o}C). Specifically, during the initial condensation to melamine, large amounts of the precursors evaporate. Since ammonia is generated and needs to be eliminated throughout the progress of g-C_3N_4 synthesis, the system should not be

sealed, especially for cyanamide, which needs a flow of N_2 during the calcination. It is suggested that using dicyandiamide or melamine instead of cyanamide and accelerate the formation of the melamine phase, reducing the evaporation and increasing the yield.[44]

Importantly, the polymerisation is usually incomplete. A C/N atomic ratio of approximately 0.67 is found in synthesised graphitic carbon nitrides using nitrogen-rich precursors, which is far from the theoretical ratio 0.75.[47-49] It is noted that g-C_3N_4 with the final structure in Fig. 1.10 is an ideal model for graphitic carbon nitrides. In fact, with various synthesis methods and degree of polymerisation, the real structures for the products are slightly different from the theoretical g-C_3N_4 infinite sheet. As a result, graphitic carbon nitrides are commonly a mixture of $C_xN_yH_z$ compounds with a variety of degrees of polymerisation. This also indicates that g-C_3N_4 is just an abbreviation for graphitic carbon nitrides rather than an accurate description of structure and elemental ratio.

During polymerisation, polymeric melon, consisting of tri-s-triazine (heptazine) units, is a relatively stable intermediate. This compound was the first synthesised polymeric carbon nitride by Berzelius and Liebig in 1834, known as "Liebig's melon".[43] The empirical formula of melon is $C_6N_9H_3$ although there is not a unique structure for it. Incomplete polymerisation of tri-s-triazine units could lead to many possible structures. Two models were put forward, as shown in Fig.1.11.[50] One is a tri-heptazine molecule (Fig.1.11a) and the other an infinite chain (Fig.1.11b), both of which could potentially be further polymerised to g-C_3N_4. These structures are commonly referred to as melon which is an ill-defined material used as a fire retardant. Recent work has aimed to clarify the structure of carbon nitrides and in most cases it appears that polymeric carbon nitride is in fact a mixture of motifs. Lotsch *et al*. firstly proved the structure of melon.[48] 2D structure of melon consists of 1D infinite chains

rather than 2D atomic arrays (Fig. 1.11b), as shown in Fig. 1.12. It also suggested that some of the "g-C_3N_4" reported in the literatures may be melon or relative materials.[48]

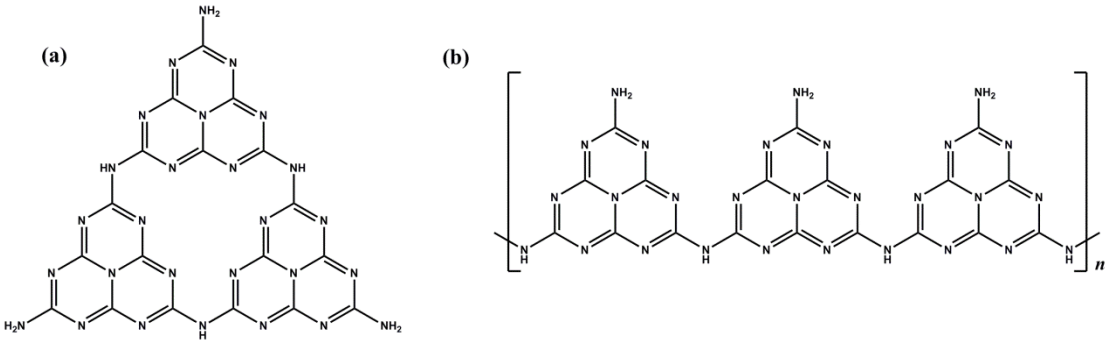

Figure 1.11: Hypothetical structure models for the formula $C_6N_9H_3$. [50]

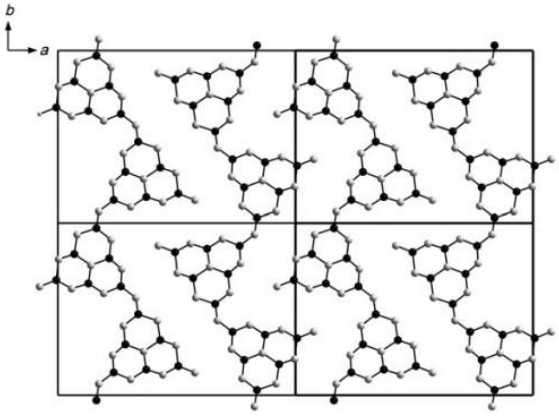

Figure 1.12: Projection of the structure of melon by Lotsch *et al.*.[48]

It has been shown that "g-C_3N_4" is an efficient photocatalyst for H_2 evolution. Bulk g-C_3N_4 produces approximately 250 μmol H_2 in 24 h with 0.1 g catalyst (Fig. 1.13 a).[18] The reaction is fulfilled by 3 wt % Pt as a cocatalyst and triethanolamine as sacrificial reductant. g-C_3N_4 nanosheets made by liquid phase exfoliation shows higher photoacitivity, generating more than 300 μmol H_2 in 4 h with 0.05 g catalyst (Fig. 1.13b).[51]

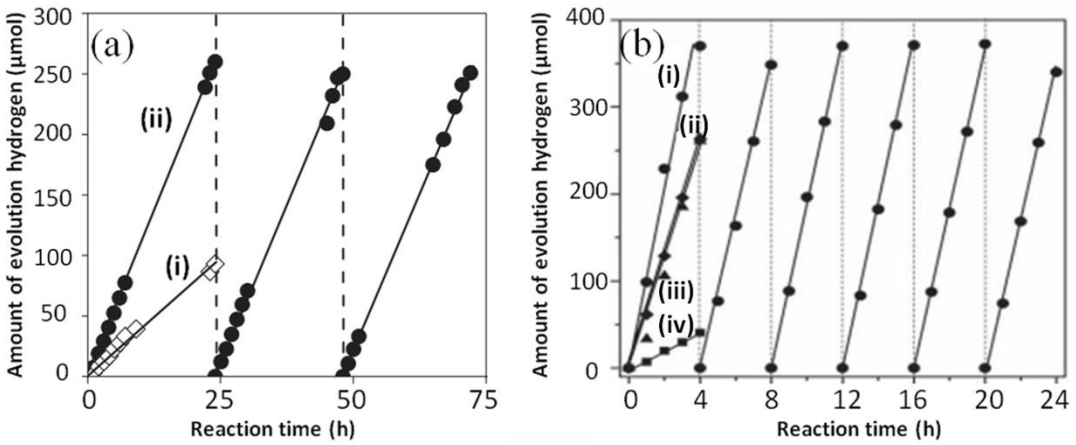

Figure 1.13: H_2 evolution from water by g-C_3N_4: (a) 0.1 g bulk g-C_3N_4 in 100 mL 10 vol % triethanolamine aqueous solution under visible light by (I) bare g-C_3N_4 and (II) 3 wt % Pt-loading g-C_3N_4;[18] (b) (I) exfoliated g-C_3N_4 nanosheets, (II) g-C_3N_4 nanosheets synthesized by thermal exfoliation, (III) highly ordered mesoporous g-C_3N_4, and finally (IV) bulk g-C_3N_4. 50 mg of catalyst loaded with 3 wt % of Pt cocatalyst; 100 mL 10 vol % triethanolamine aqueous solution under visible light.[51]

Compared with bulk g-C_3N_4, nanoporous g-C_3N_4 has larger surface area and higher porosity, improving the photocatalytic efficiency by enhancing the light-harvesting and reducing the recombination of charge carriers.[40, 52, 53] Macroporous and mesoporous g-C_3N_4 were prepared by soft- and hard-templating methods, as shown in Fig. 1.14.[40] Ordered macroporous g-C_3N_4 has been obtained by colloidal silica templating. Hwang *et al.*[54] reported well-ordered macroporous g-C_3N_4 with the C/N atomic ratio of 0.72 and 0.74, which is close to the stoichiometric ratio (as shown in Fig.1.15). As for mesoporous g-C_3N_4, some distortion makes the C/N ratio far less than the theoretical value of 0.75 probably because the 2D structure of g-C_3N_4 cannot fit the curvature of the nanopores.[55] Groenewolt *et al.*[56] synthesised mesoporous g-C_3N_4 with different diameters by using different templates. Lee *et al.*[57] fabricated cubic mesoporous ordered g-C_3N_4 by a nanocasting method. The TEM pattern is shown in Fig 1.16. The precursors are mostly cyanamide and its solution or molten state is used to immerse the silica template.[56, 57] So far, for ordered macroporous g-C_3N_4 materials no photonic properties have been described. Fig. 1.17 shows the H_2 evolution by mesoporous and macroporous g-C_3N_4, respectively. As can be seen from the graph,

the photoactivity of the catalyst has been dramatically enhanced.

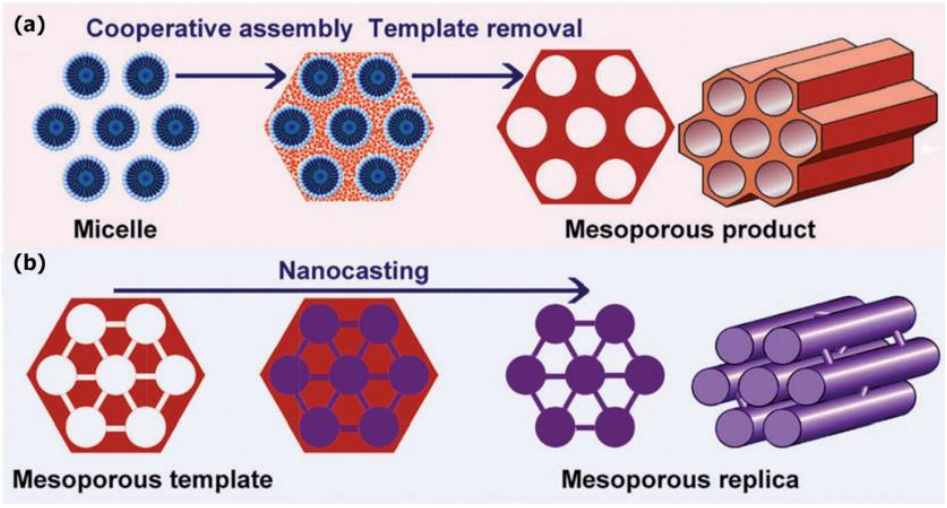

Figure 1.14: Scheme of two major routes for the synthesis of meso-g-C_3N_4: (a) soft-templating and (b) hard-templating method.[40]

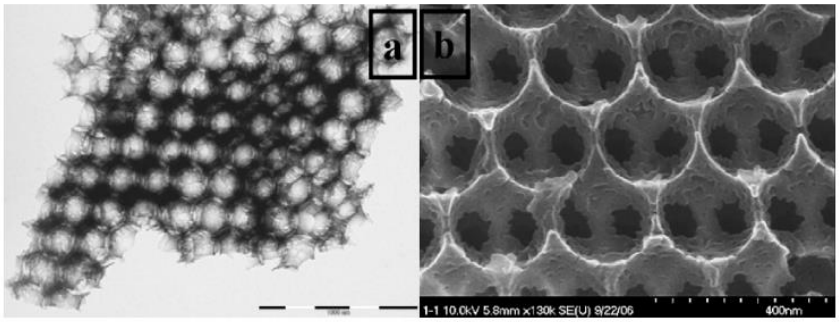

Figure 1.15: TEM image (a) and SEM image (b) of macroporous g-C_3N_4 in Hwang's work.[54]

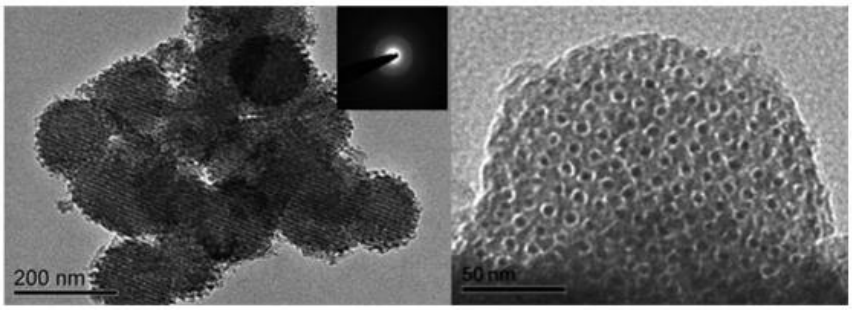

Figure 1.16: TEM images and an electron diffraction pattern of cubic mesoporous g-C_3N_4.[57]

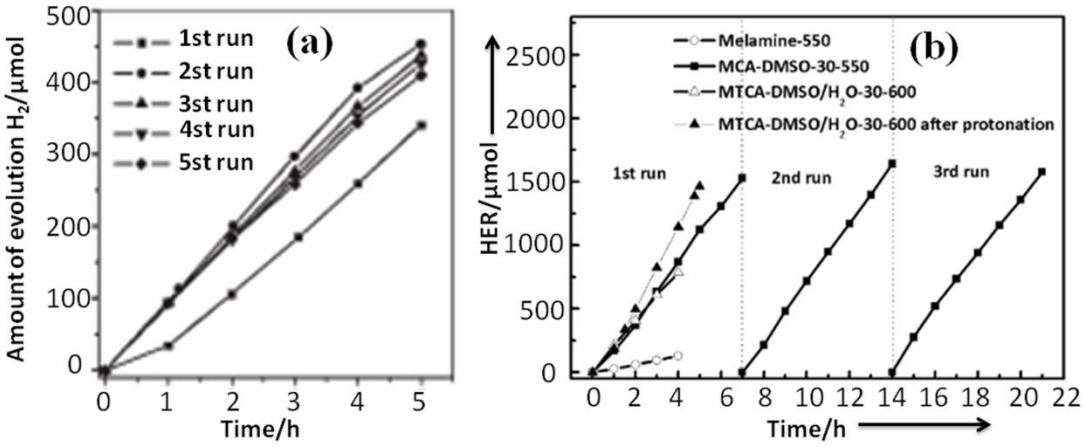

Figure 1.17: H_2 evolution (a) ordered mesoporous g-C_3N_4 (0.1 g);[58] (b) three dimensional ordered macroporous g-C_3N_4 (50 mg) made with various donor-acceptor pairs, solvents (mixing at 30 ^oC) and calcination temperatures.[59] Both of the photocatalysts in the reactions are loaded with 3 wt % Pt and the solution is 100 mL 10 vol % triethanolamine aqueous solution irradiated under visible light.

To enhance the properties of g-C_3N_4 in photocatalytic water splitting further, g-C_3N_4-based heterogeneous system has recently been developed. g-C_3N_4 has been modified by doping non-metal elements including B, F, P and S,[40] and moreover metallic elements are also doped into it by adding metal chlorides at 600 ^oC.[60, 61] In addition to adding these ions slightly changing the photocatalyitc efficiency, charge-transfer units have also been designed into the system. Graphene sheets have similar 2D structure with g-C_3N_4, thus making the composite lead to unique physical and chemical properties.[40] Xiang *et al.*[62] reported graphene/g-C_3N_4 composites, in which graphene sheets are acting as electron transport channel, can help separate the electron-hole pairs efficiently (Fig. 1.18a). It is reported that g-C_3N_4 coupled with CdS quantum dots has better photocatalytic activity than both pure g-C_3N_4 and CdS quantum dots (Fig. 1.18b).[63]

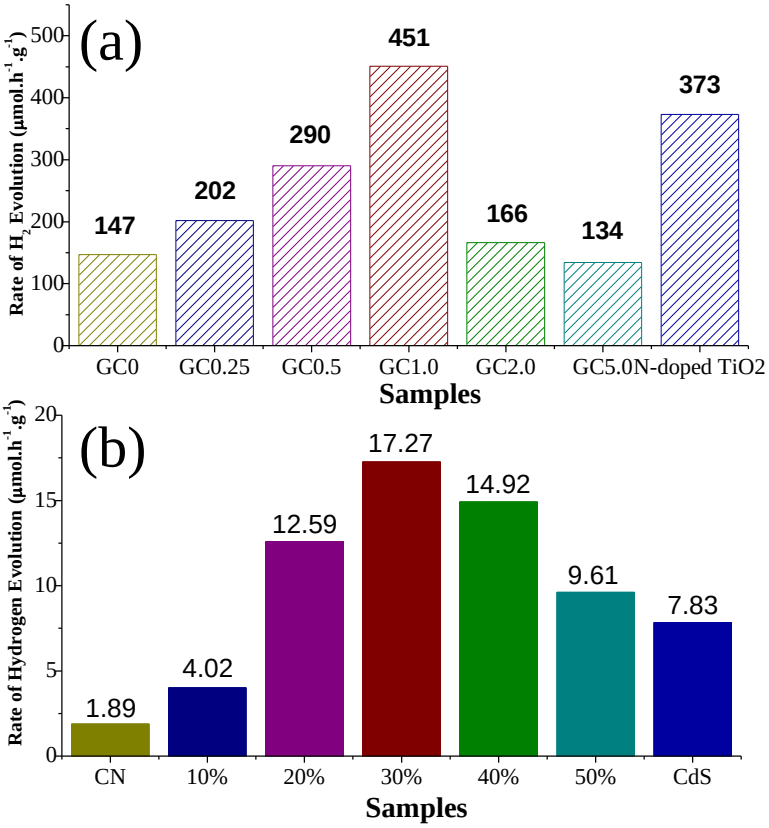

Figure 1.18: H_2 evolution of g-C_3N_4-based heterogeneous system: (a) graphene/g-C_3N_4 composites[62] and (b) g-C_3N_4 coupled with CdS quantum dots. g-C_3N_4 was acting as the host material, and graphene and CdS with various weight percentages (0, 0.25, 0.5, 1.0, 2.0, 5.0 wt % graphene), respectively.[63] Graphene/g-C_3N_4 composites (80 mg) photocatalytist and CdS/g-C_3N_4 composites (100 mg) were put into methanol aqueous solution, respectively, irradiated under visible light.

1.3.3 Highly Ordered Macroporous Materials in Photocatalytic Reactions

Three dimensional ordered macroporous (3DOM) materials with a periodic modulation have become an active area of research.[64] The 3DOM structure is derived from the opal crystal structure, which consists of close-packed periodic array of silica particles with uniform size.[65] Because of this structure, visible light with a similar wavelength range is reflected by the periodic array.[65] 3DOM materials are also called inverse opals, since they are templated from the opaline structure.[65] These materials possess high surface area and interconnected macropores, as well as unique photonic properties. Similar with opal crystal, the photonic band gap (stop band) in 3DOM materials can inhibit incident light in a certain wavelength range from propagating

through the material in all directions, when the refractive index of the material is relatively large.[64] This phenomenon results in reflection of this wavelength range, hence macroporous materials usually show bright colours. For photocatalytic application, these properties facilitate the process of H_2 evolution. Specifically, high surface area increases the active catalytic sites and the interconnected macropores provide a channel for the transportation of the protolyte or electrolyte (in solar cell devices) solution.[65] Furthermore, the photonic properties can reduce the electron-hole pairs' recombination at the wavelength of the stop band or increase the pathlength of wavelengths in the vicinity of the stop band effectively.

When a photon is absorbed by a photocatalyst, the electron in the valence band would be excited to the conduction band. After that, the electron could relax back to the valence band and release a photon, which is the recombination of electron-hole pairs. However, when the wavelength of incident visible light is close to the stop band wavelength, the photon cannot pass through the materials, thus inhibiting the electron from jumping back to the valance band.[64] The photonic properties can be tuned by controlling the size of macropores and filling the pores with fluids with different refractive indexes, as shown in Equation 1.4 and 1.5.[64]

$$\lambda = 2d_{hkl}/m[\varphi n_{wall} + (1-\varphi)n_{void}] \quad (1.4)$$

$$d_{hkl} = D(2)^{\frac{1}{2}}/(h^2+k^2+l^2)^{1/2} \quad (1.5)$$

λ: wavelength

d_{hkl} : interplanar spacing

m: order of Bragg diffraction

n_{wall}: refractive index of wall material

n_{void}: refractive index of void space (solvent)

D: pore spacing

Macroporous materials are used in the photocatalytic water-splitting. 3DOM TiO_2/CdS is reported with higher photocatalytic efficiency compared with

conventional TiO_2/CdS composite.[66] CdS nanoparticles were loaded onto macroporous TiO_2 and high photocurrent was achieved. The 3DOM skeleton of TiO_2 facilitates higher loading of CdS because of its high surface area, and reduces the recombination of electron-hole pairs.[65, 66]

A common and straightforward scheme to synthesis macroporous materials is colloidal crystal templating, which is applied in this thesis, as shown in Fig. 1.19.[65, 67] Monodispersed colloidal particles are assembled to close-packed arrays, followed by an infiltration of fluid precursor into the voids between the spheres. After the template is removed by calcination or acid corrosion, 3DOM structure is formed as an inverse template with interconnected windows. The commonly used colloidal crystal templates are silica, polystyrene (PS), poly(methyl methacrylate) (PMMA), and poly(styrene-methyl methacrylate-acrylic acid) (p(St-MMA-AA)).[65] Polystyrene spheres are employed in this thesis as replicates since they can be easily removed by calcination below 500 ^oC.

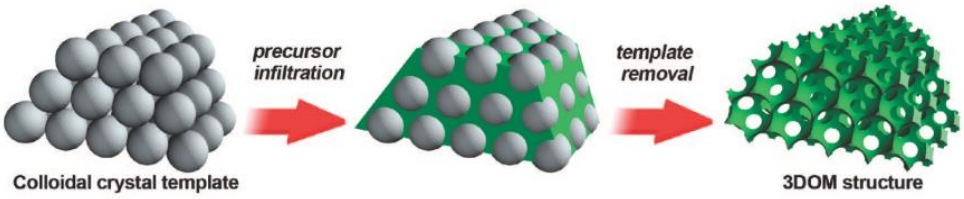

Figure 1.19: Scheme illustration of colloidal crystal templating.[67]

3DOM can also act as a host material, not only for confinement of nanoparticles but also a mold for making opal structure with other compositions.[65] The scheme can be described as the back process shown in Fig. 1.19 (the order of infiltration and template removal keeps the same). In this thesis, we take advantage of this phenomenon, trying to add precursor to the 3DOM skeleton and adjust the concentration of precursor solution to achieve variable loading g-C_3N_4.

1.4 Aim of Project

Since g-C_3N_4 is a promising photocatalyst and 3DOM materials can provide a skeleton with high surface area and photonic properties, the combination of these two materials should result in an enhancement of photocatalytic activity of H_2 evolution. Coating thin layers of g-C_3N_4 onto the wall of the macropores can be a desirable idea. Macroporous silica (Mac-SiO_2) and zirconia (Mac-ZrO_2) are easy to synthesise, so they are used as host materials for g-C_3N_4 in this thesis. Due to time restrictions the work describing Mac-ZrO_2 is less complete than Mac-SiO_2. More generally, this strategy could also potentially be applied to any layered bulk photocatalyst or catalytically active material, where an increase in surface area is required. Locating one or a few layers into a porous material will prevent aggregation and lead to higher activity.

Also included in this thesis is a short description of using metal silicides as visible light active photocatalysts. This was the initial aim of the project. However, it was found that a lead reference in this area could not be repeated. A short description of this work and our findings is provided in Chapter 3.

Result and discussion

Chapter 2

In this section, the coating of graphitic carbon nitrides onto macroporous SiO_2 and ZrO_2 is described. Macroporous materials not only show unique periodic structure and photonic properties, but also provide large surface area for photocatalysts loaded onto their surface. As described in Section 1.3.3, g-C_3N_4 shows outstanding photocatalytic activity for H_2 evolution from half reaction of water splitting in the presence of a sacrificial agent. Coating g-C_3N_4 on to a macroporous material could increase the active sites of g-C_3N_4 and potentially the photonic properties could enhance light absorption or inhibit electron-hole recombination.

In our experiment, the synthesis, structure and performance of bulk g-C_3N_4 and g-C_3N_4/Mac-SiO_2 composites are discussed, including optimising the g-C_3N_4 synthetic conditions, making comparison of the structure and properties between bulk g-C_3N_4 and g-C_3N_4/Mac-SiO_2 composites, and searching the best g-C_3N_4 content for H_2 evolution. Scanning Electron Microscopy (SEM), Transmission Electron Microscopy (TEM), Powder X-ray diffraction (PXRD), surface area measurement (BET), Fourier Transform Infrared Spectroscopy (FT-IR), Nuclear Magnetic Resonance Spectroscopy (NMR) and UV-Vis Diffuse Reflectance and Absorbance Spectroscopy and will be used to characterise the structure of bulk g-C_3N_4 and g-C_3N_4/Mac-SiO_2 composites. The Mac-SiO_2 composites have also been tested for their activity toward photocatalytic H_2 evolution under visible light illumination. In this thesis, the C/N ratio of carbon nitrides synthesised in this thesis is not 0.75 (see Section 2.1.2 and 2.6.1). Hence, we will use "C_xN_y" instead of "g-C_3N_4" to describe this material in the contents below.

2.1 Synthesis and Characterisation of Bulk C_xN_y

A variety of methods have been used to make graphitic carbon nitrides. Heating nitrogen-rich precursors such as cyanamide, dicyandiamide and melamine is an efficient way to synthesise C_xN_y, avoiding the introduction of other elements.[44] In this thesis, C_xN_y is used to coat onto macroporous materials; therefore, the solubility of these precursors should be taken into consideration. Since the project requires the precursor molecule to enter the macropores, it is becomes important to choose an easily soluble precursor. Cyanamide can be easily dissolved in water and ethanol while the solubility of dicyandiamide is relatively low. Melamine has very low solubility in all common solvents. The structure of these precursors is shown in Fig. 1.10 (see Section 1.3.2).

2.1.1 Comparison between Different Precursors

To synthesise C_xN_y, 150 mg cyanamide (CA) and dicyandiamide (DCDA) were put into 2 mL vials, respectively, and calcined to 550 ^oC for 4 h with a flow of nitrogen. During the polycondensation where cyanamide and dicyandiamide become melamine, large amounts of the raw materials evaporated. The yield from cyanamide is less than 50%, e.g., 300 mg cyanamide produces 120 mg C_xN_y. The products are orange (from CA) and light yellow (from DCDA) chunks, respectively. The chunks were ground into powders and then characterised by PXRD, FT-IR and NMR spectroscopies.

Fig. 2.1 shows the PXRD pattern of C_xN_y made from CA and DCDA, respectively. Only two typical peaks are observed in both of the samples, which are indistinguishable to those reported in the literature for g-C_3N_4,[18] indicating that the products are graphitic carbon nitrides. The peaks are indexed using Jade 5.0. The strongest peak at ~27^o, which is indexed as (002), corresponds to the interlayer spacing of the graphitic structure, and the d-spacing values are 0.329 nm (from CA) and 0.325 nm (from DCDA), respectively, which are both very close to the value 0.326 nm reported in the

literature.[18] The small peak at ~13°, corresponds to the inter-plane spacing of 0.672 nm (from CA) and 0.660 nm (from DCDA), respectively, due to the tri-s-triazine moiety (Fig. 1.7b) and is indexed as (100).[68] C_xN_y made from DCDA has better crystallinity indicated by a narrower peak width at 27°.

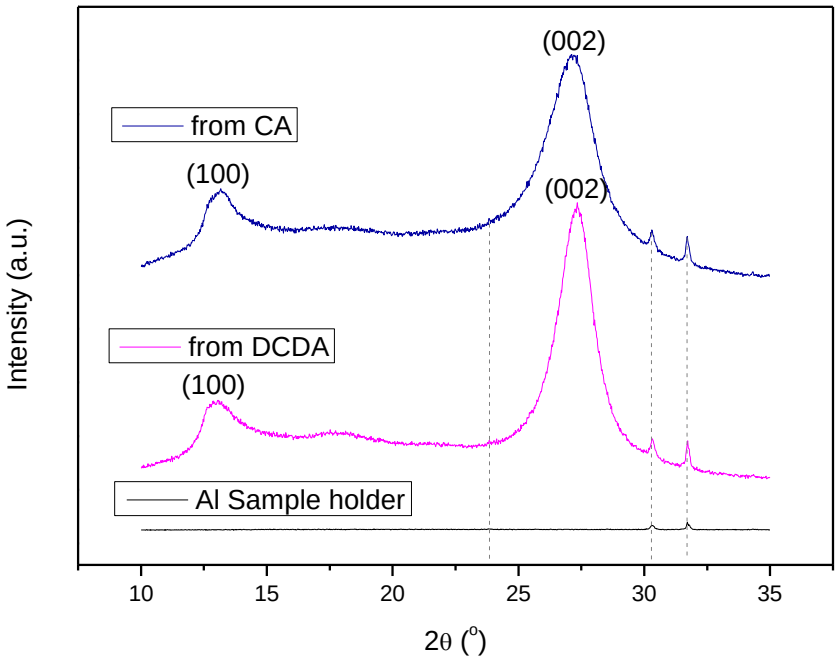

Figure 2.1: PXRD pattern of C_xN_y made from CA and DCDA. The two small peaks at 30.3 and 31.7° are both from the slightly contaminated aluminium sample holder.

The diffuse reflectance and absorbance spectra are shown in Fig. 2.2. As can be seen from the spectra, C_xN_y made from CA can absorb more visible light. The absorbance spectra of C_xN_y are generally similar with described in some literature (Fig. 1.9).[18] However, the broad declining ranges between 450-600 nm indicate that C_xN_y made from CA has a lower band gap compared with that in the Wang's work,[18] as shown in Fig. 2.2(b).

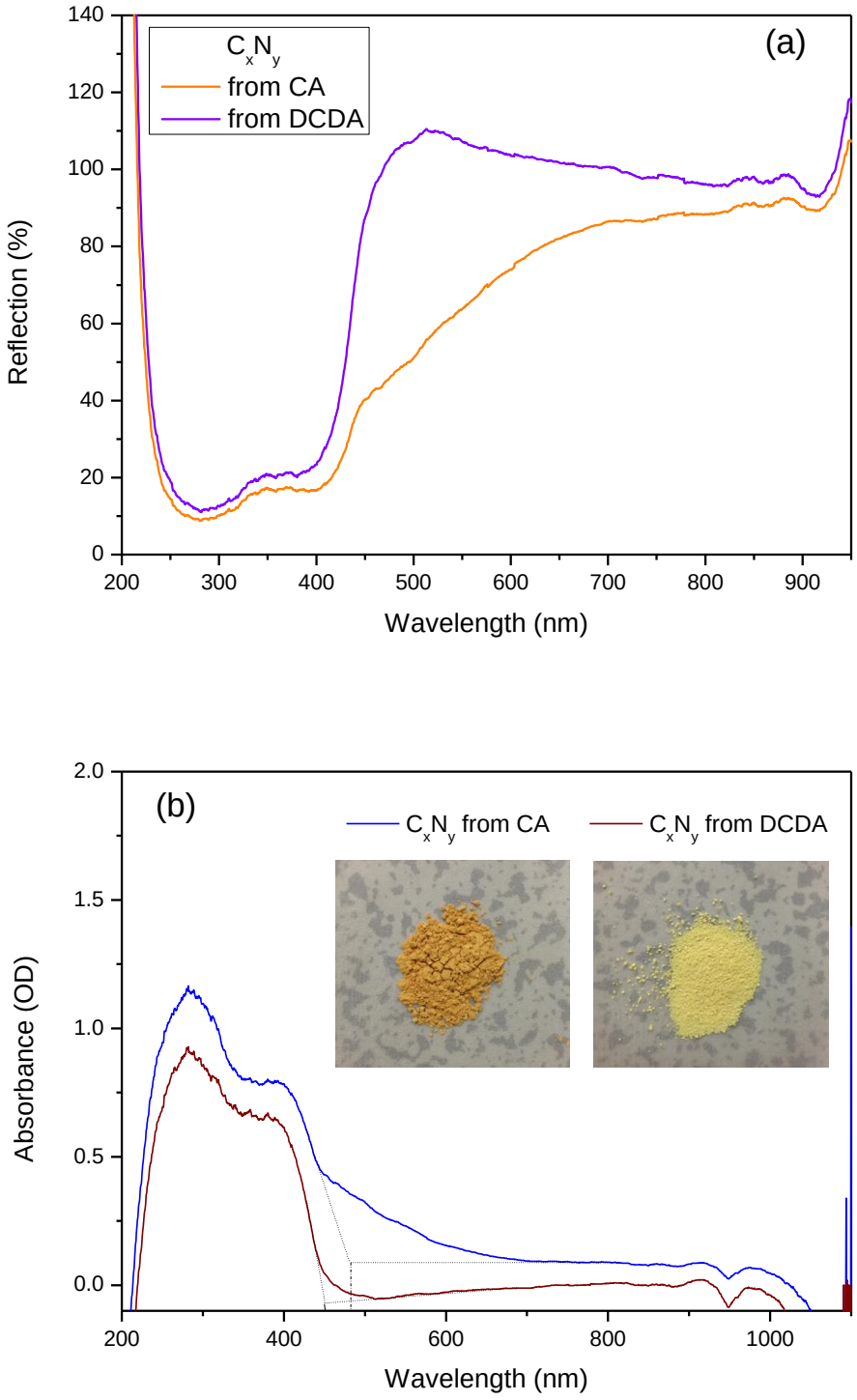

Figure 2.2: Diffuse (a) reflectance and (b) absorbance spectra of C_xN_y made from CA and DCDA, respectively. The dotted lines (b) are the tangent lines of the absorbance spectra. The abscissae of their intersection points are the estimated absorption edges.

The band gap energy can be estimated by analysing the absorbance spectra. The

absorption edge is determined as shown in Fig. 2.2b. According to the equation $E=h\nu=hc/\lambda$, the estimated band gap energy can be calculated. The results are listed in Table 2.1, which are close to the value 2.6 eV determined in other reports.[18]

Table 2.1: Estimation of the band gap energy of C_xN_y from the experimental values

	C_xN_y from CA	C_xN_y from DCDA
Absorption edge (nm)	482.5 ±10	449.8 ±10
Band gap energy (eV)	2.57 ±0.06	2.76 ±0.06

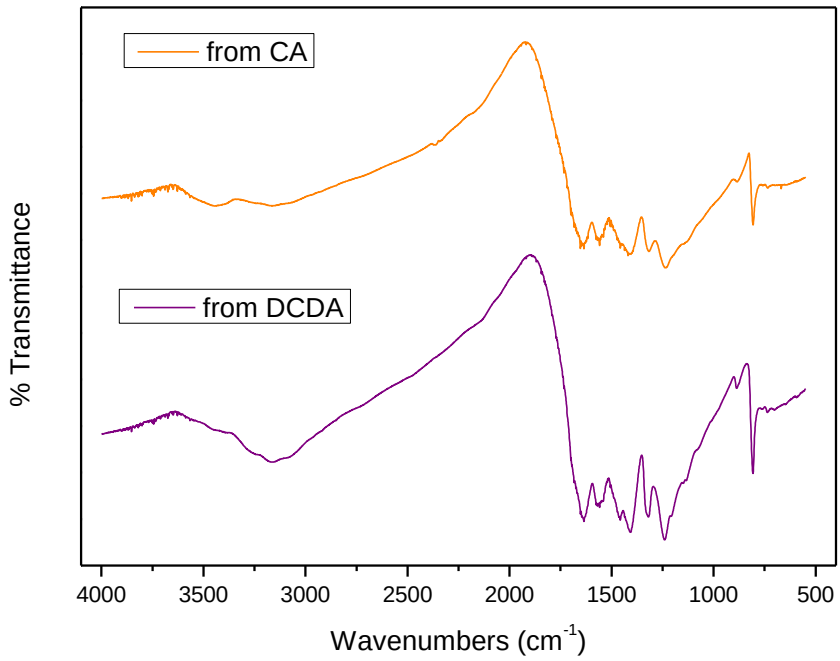

Figure 2.3: FT-IR spectra of C_xN_y made from CA and DCDA, respectively.

FT-IR spectroscopy is used to probe the local structure via the bond vibrations. Fig. 2.3 shows the FT-IR spectra of C_xN_y made from CA and DCDA, respectively. The strong peak at 800 nm^{-1} corresponds to the C–N hexagon rings (tri-s-triazine or triazine units) (Fig. 1.7). The C–N(H)–C bonds which connect the rings are shown in the 1200-1400 nm^{-1} region.[69] The vibration within 1200-1600 nm^{-1} is assigned to aromatic CN heterocycles.[46] These characteristics are similar between the two spectra. However, the difference is the broad vibration at about 3200 nm^{-1}, which is assigned to the N–H

bonds. The N–H bonds indicate that amino group still exists in the products.[70] C_xN_y made from DCDA possesses a more intense peak than that from CA, indicating that the degree of polymerisation of the latter one is higher because of less N–H bond. In the region 2200 cm^{-1} there is no significant signal, where the C≡N and –CN=C=N– bonds is shown, indicating that no cyanamide or DCDA are left after the polymerisation.[69]

2.1.2 Optimisation of Calcination Conditions

From the above comparison, cyanamide is the best option to synthesis C_xN_y, since C_xN_y from CA absorbs more visible light (Fig. 2.2). To investigate the effect of heating, CA was heated to a range of temperatures between 550 and 650 ^oC. By increasing the temperature, the colour of the samples changes from orange to red. The results are analysed by FT-IR spectroscopy, as shown in Fig. 2.4. For the samples calcined at 550 and 600 ^oC, the spectra do not show any difference. As 650 ^oC, the shape of spectrum has been slightly changed. Furthermore, the results of bulk elemental combustion analysis show that 13.5% and 16.2% (by mass) of impurity elements are introduced into C_xN_y by increasing the calcination temperature to 600 and 650 ^oC, respectively (Table 2.2). From the EDX result (for C_xN_y calcined to 650 ^oC), among the elements, O accounts for the largest percentage, followed by Na and Si, which are the elements present in the glass vials (Fig. 2.5).

Table 2.2: CHN results of C_xN_y made by heating CA to various temperatures (by mass).

T/^oC	% C	% H	% N	% Rest	C/N (atomic)	H/N (atomic)
550	34.149	1.622	59.202	5.03	0.673	0.384
600	31.213	1.537	53.754	13.50	0.677	0.400
650	31.05	1.76	50.99	16.20	0.710	0.483

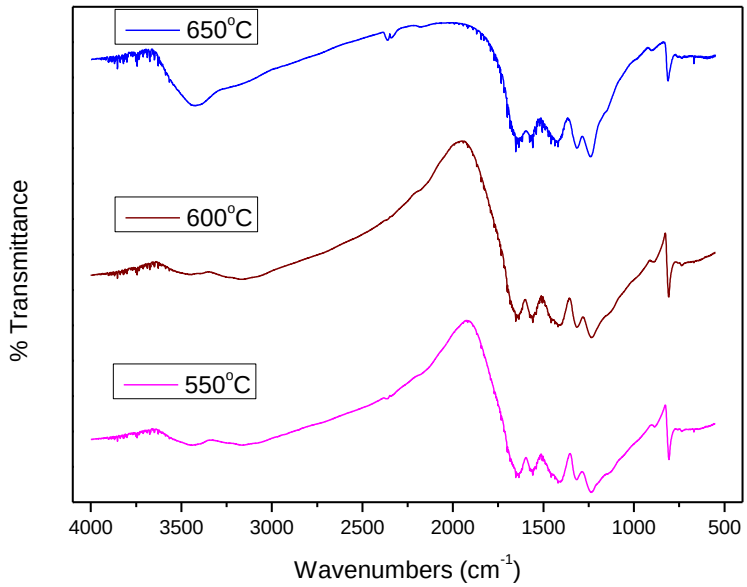

Figure 2.4: FT-IR spectra of bulk C_xN_y made from CA with various heating temperatures.

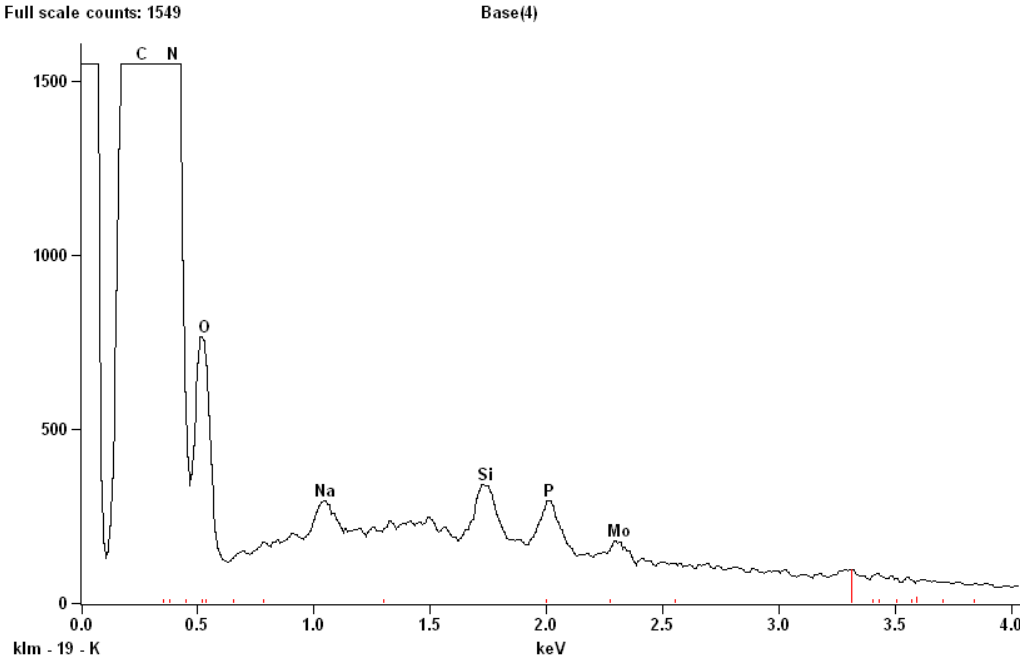

Quantitative Results for: C_xN_y

Element Line	***Net Counts***	***K-Ratio***	***K-Ratio Error***	***Norm. Wt.%***	***Atom %***	***Atom % Error***
C K	55738	0.56C	+/-0.00	34.39	38.58	+/- 0.29
N K	24245	0.39C	+/-0.01	57.44	55.26	+/- 0.76
O K	4095	0.03C	+/-0.00	6.60	5.56	+/- 0.17
Na K	812	0.00	+/-0.00	0.22	0.13	+/- 0.01
Si K	1733	0.01	+/-0.00	0.45	0.21	+/- 0.02
P K	1567	0.01	+/-0.00	0.42	0.18	+/- 0.02
Mo L	935	0.01	+/-0.00	0.48	0.07	+/- 0.01
Total				100.00	100.00	

Figure 2.5: EDX spectrum and quantitative result of bulk C_xN_y made from CA calcined to 650 ^oC for 4 h.

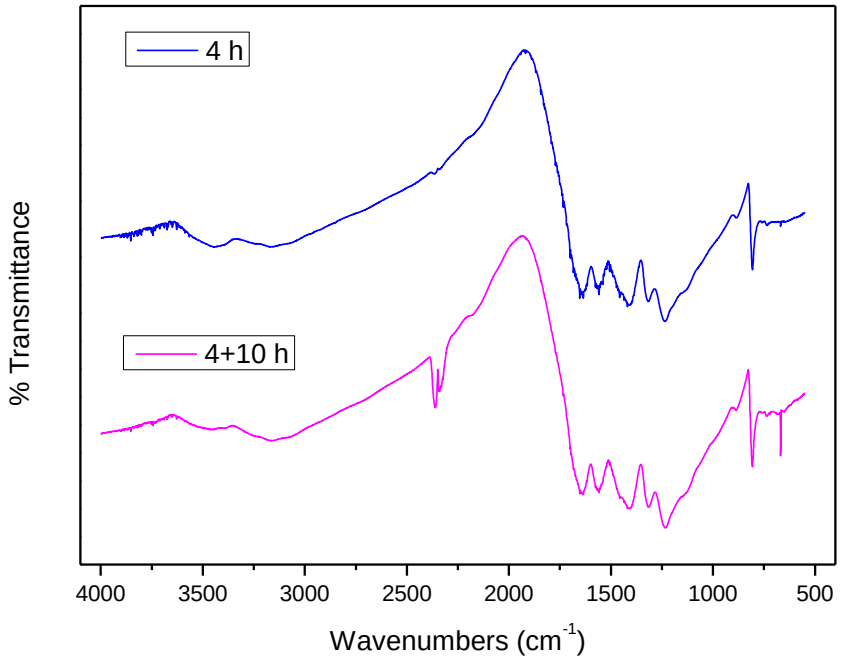

Figure 2.6: FT-IR spectra of C_xN_y made by heating CA to 550 ^oC for 4 h and 14 h, respectively. (The peaks at 2300 cm^{-1} are CO_2.)

To test if the polymerisation has completed after heating for 4 hours, the C_xN_y sample heated to 550 ^oC for 4 hours was heated for a further 10 hours. From the FT-IR spectra

(Fig. 2.6) and elemental analysis (Table 2.3), no big difference is found in the two samples. It can be concluded that the polymerisation has completed after heating for 4 hours.

Table 2.3: CHN results of C_xN_y made by heating CA to 550 ^oC with different dwelling times.

t/h	% C	% H	% N	% Rest	C/N (atomic)	H/N (atomic)
4	34.149	1.622	59.202	5.03	0.673	0.384
4+10	33.918	1.496	59.14	5.45	0.669	0.354

From the above mentioned experiments and characterisation, the optimal calcination condition for directly heating nitrogen-rich precursors should be heating CA to 550 ^oC for 4 h under nitrogen and it is clear that the product is not pure C_xN_y.

2.1.3 Structural Characterisation of C_xN_y

Bulk C_xN_y made by heating CA to 550 ^oC for 4 hours under nitrogen was also characterised by SEM, EDX and SSNMR (Solid-State Nuclear Magnetic Resonance Spectroscopy). As has already been noted C_xN_y is an ideal molecular formula, and is used as an abbreviation for graphitic carbon nitrides. The formula and structure of the graphitic carbon nitrides made in this thesis is discussed below.

The SEM image shows the macrostructure of polymeric carbon nitrides (Fig. 2.7). C_xN_y appears as a porous structure, which could be attributed to the elimination of gas during polymerisation. Some sheets are observed for the C_xN_y sample, in accordance with the graphitic structure.

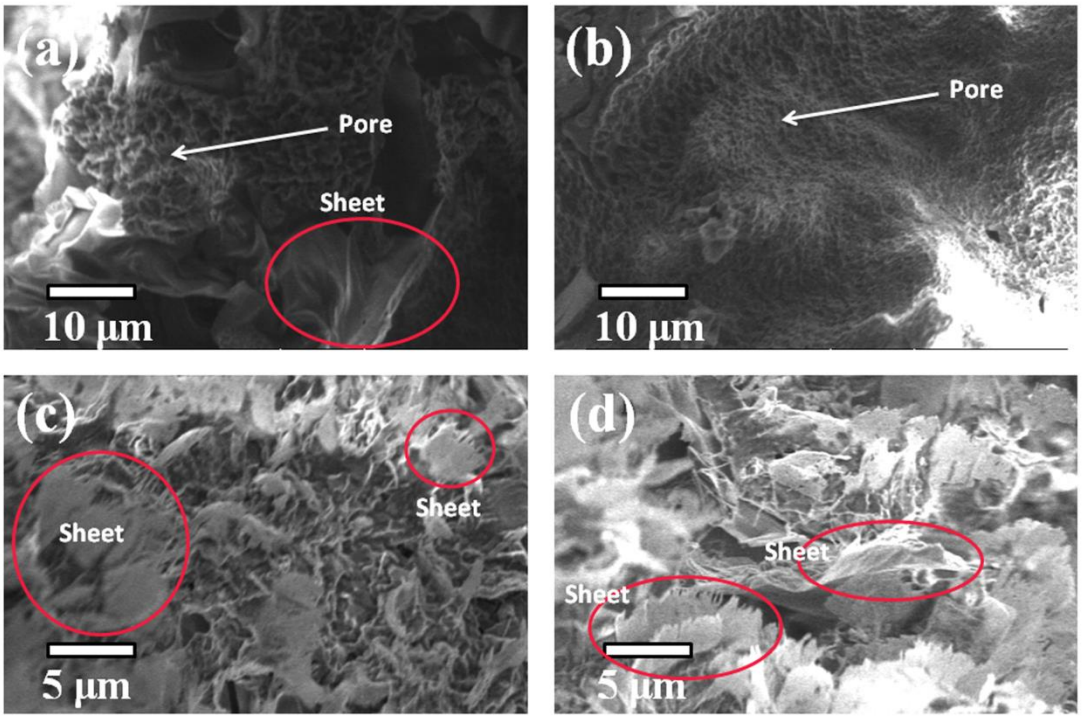

Figure 2.7: SEM images of C_xN_y, taken from different sample regions.

There have been debates on whether the unit of C_xN_y is tri-s-triazine or triazine (Fig.1.7). Solid state NMR spectroscopy can provide local structural information and a sample was analysed at the EPSRC Centre for NMR at the University of Durham. The experiments were natural abundance ^{13}C NMR and cross polarisation magic angle spinning (CPMAS). Direct detection resulted in very low intensity and no signals were detected. However, CPMASNMR gave two signals of very similar intensity at δ 157 and 164 ppm shown in Fig. 2.8. These signals are consistent with those in the literature that are assigned to CN_3 and $CN_2(NH_x)$ moieties, respectively indicating that hydrogen is present and the structure is based on tri-s-triazine rings.[48] The signals at δ 90 and 230 ppm are spinning sidebands, which are commonly observed.

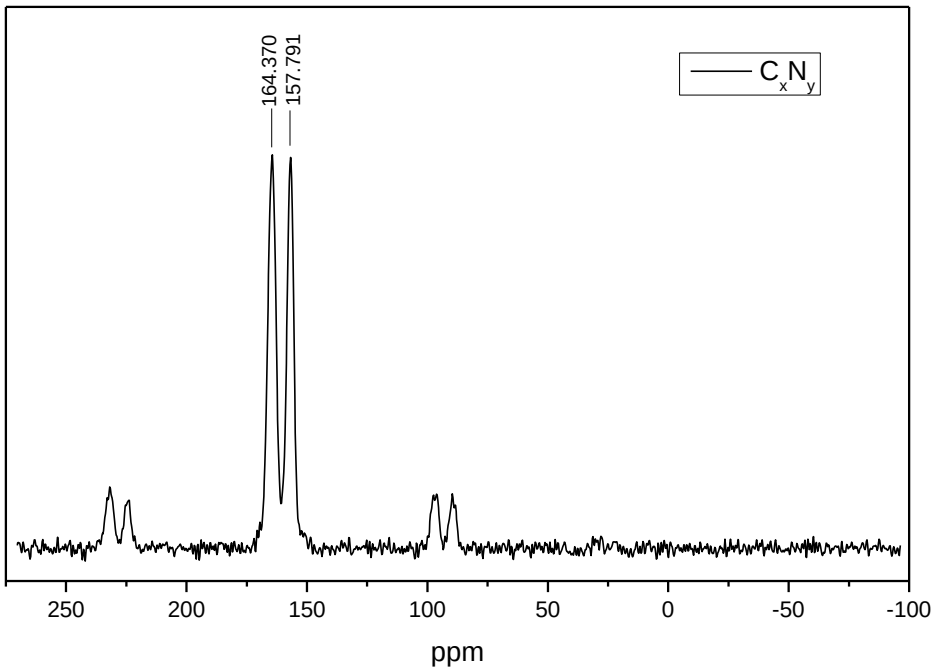

Figure 2.8: NMR spectrum of bulk C_xN_y sample. Nuclei observed: C-13.

The elemental analysis and EDX both suggest that the atomic C/N ratio is approaching 2/3, as shown in Table 2.4 and Fig. 2.9. As the experimental ratio is far from the theoretical ratio of 0.75, the structure of C_xN_y in this thesis is not the same as the infinite model shown in Fig 1.7(b), although all other data (e.g. XRD pattern, FT-IR spectrum, E_g value, UV-Vis absorbance spectrum and appearance) is consistent with the literature characterisation of "g-C_3N_4". The excess of N atoms suggests that the polymerisation process has not completed in terms of all the amino groups on the tri-s-triazine (heptazine) unit. The H/N atomic ratio is approaching 1/3, indicating that the molecular formula is C_2N_3H. In case that possible residues of carbon was taken into account, combustion aid was added. However, no big difference was made. This formula is in line with the polymeric melon (see Section 1.3.2), which is consistent with the elemental analysis data and CPMAS NMR. Although the structure of melon has been proved,[48] it is still possible that the carbon nitride in this thesis is a mixture of motifs with various degrees of polymerisation.

Table 2.4: CHN test of bulk C_xN_y in this thesis

Precursor	% C	% H	% N	% Rest	C/N (atomic)	H/N (atomic)
cyanamide	34.129	1.417	59.704	4.75	0.667	0.332
dicyandiamide	34.171	1.614	61.074	3.14	0.653	0.370

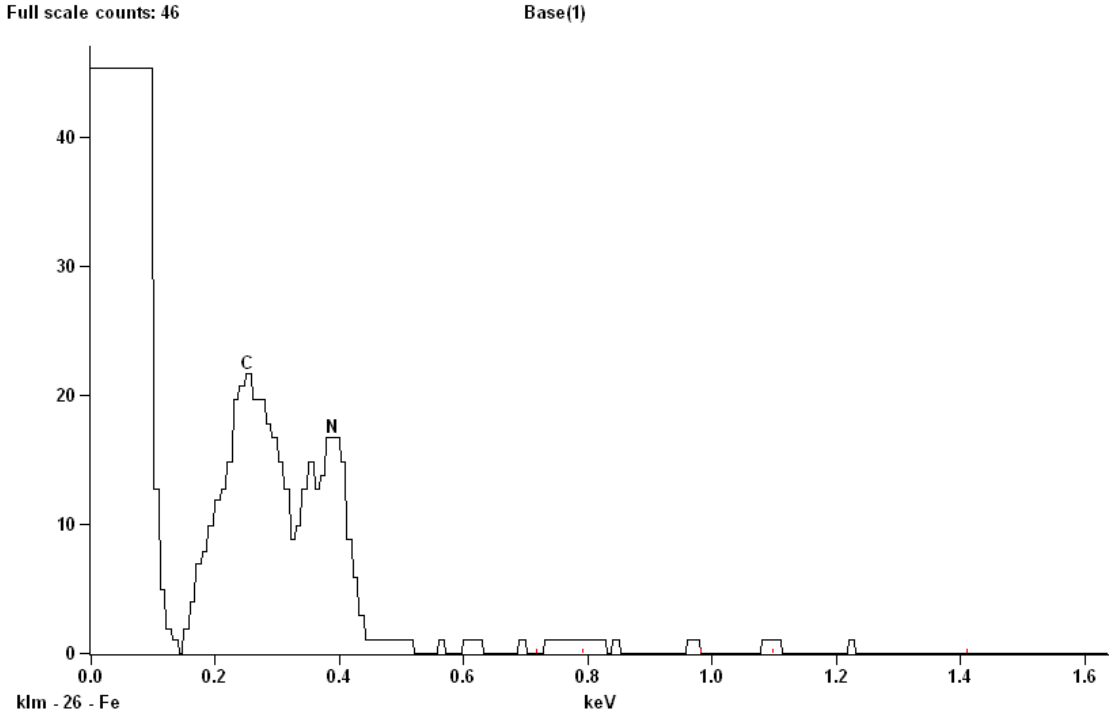

Quantitative Results for: C_xN_y

Element Line	***Net Counts***	***K-Ratio***	***K-Ratio Error***	***Norm. Wt.%***	***Atom %***	***Atom % Error***
C K	135	0.47C	+/-0.09	36.43	40.05	+/- 7.71
N K	82	0.53C	+/-0.11	63.57	59.95	+/-11.70
Total				100.00	100.00	

Figure 2.9: EDX spectrum and quantitative result for C_xN_y (from CA, 550 ^oC, 4 h).

2.2 Synthesis of Macroporous SiO_2 and ZrO_2

In this thesis, Mac-SiO_2 and Mac-ZrO_2 were synthesised by a templating method.[64] Briefly, polystyrene spheres are close-packed into face-centred cubic (FCC) structure

using a centrifuge, for that FCC structure is preffered thermodynamically. The interstitial volume of the polystyrene sphere array is filled with a silica or zirconia precursor solution, respectively. Finally, the polystyrene is burnt off during calcination to give a three-dimensional ordered macroporous (3DOM) materials with the inverse structure of opal-structured polystyrene sphere array. Opal is a semiprecious stone that comprises face-centred cubic (fcc) packed spheres of silica. Therefore 3DOM structures are also commonly referred to as inverse opals.

Polystyrene is chosen as a template because it is easy to synthesise as homogeneously sized spheres and remove, and the size of the spheres is tunable. The polystyrene spheres are synthesised by an emulsion polymerisation method.[71]

The synthesised Mac-SiO_2 and Mac-ZrO_2 both have bright colours. This is because macroporous materials can reflect light in a certain wavelength range (stop band) which can be tuned by changing the pore size (Section 1.3.4). Mac-SiO_2 is pink-white with blue-green light in air and transparent in liquid (e.g. water and ethanol) while Mac-ZrO_2 is a mixture of light and dark green with green light and brown in liquid (e.g. water and ethanol). The UV-Vis diffuse reflectance spectra, PXRD patterns and SEM images are shown in Section 2.6.

2.3 Coating C_xN_y onto Macroporous SiO_2 and ZrO_2

Coating C_xN_y onto Mac-SiO_2 and Mac-ZrO_2 was achieved using a wet impregnation method. Specifically, macroporous materials are soaked in cyanamide ethanol solution of various concentrations. After evaporating the solvent under ambient conditions, the mixture was calcined to 550 ^oC under N_2 at a rate of 2.3 ^oC/min. During the calcination, polymerisation of cyanamide occurred and layers of C_xN_y coating were formed on the surface of the macroporous materials. The procedure is shown in Fig. 2.10.

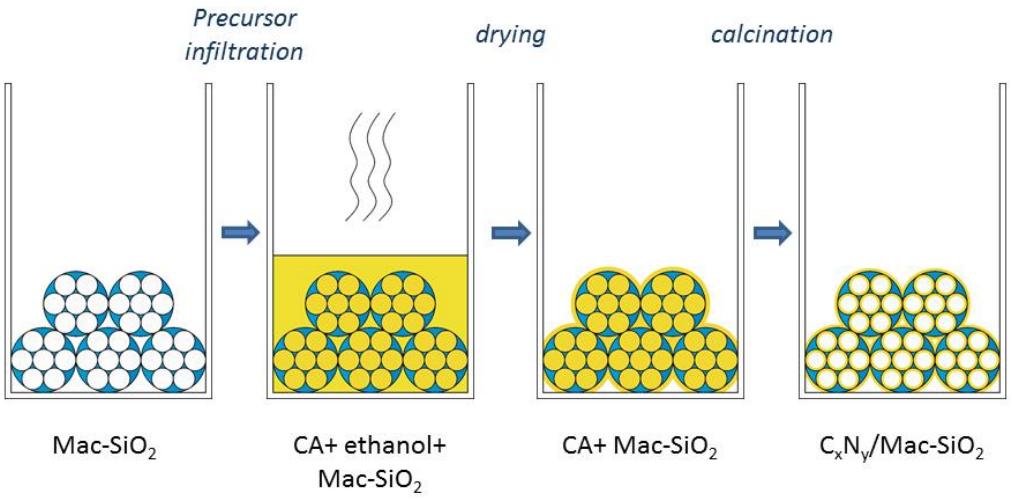

Figure 2.10: The procedure of coating C_xN_y onto macroporous SiO_2 and ZrO_2.

2.4 Addition of Pt Cocatalyst

Platinum was chosen as the cocatalyst for H_2 generation in this thesis because it acts to trap photogenerated electrons and is an excellent catalyst for the reduction of H^+ to H_2.[17] The most common way to deposit Pt onto the surface of the photocatalyst is the in-situ photodeposition method. However, the main drawback of this method is that the Pt nanoparticles are relatively easy to fall off.

In this thesis the Pt nanoparticles are loaded by a simple method. The photocatalyst is dispersed into an aqueous solution of H_2PtCl_6 hydrate, which is used as the precursor. The mixture is heated to 90 ^oC to form the H_2PtCl_6/C_xN_y composite. After the solvent has been evaporated, the mixture is heated to 200 ^oC with a flow of H_2. The role of H_2 is to reduce H_2PtCl_6 to Pt nanoparticles. The disadvantage of this method is the inhomogeneous dispersion of Pt nanoparticles.

Fig. 2.11 shows the PXRD pattern of bulk C_xN_y loaded with Pt nanoparticles. Typical C_xN_y peaks (13.2^o and 26.3^o) were obvious in the pattern, which showed that C_xN_y did not change after heating under H_2. Characteristic peaks of Pt were observed at 40 ^{o}, 46 ^{o} and 67.5 ^{o}, indicating that Pt was generated.

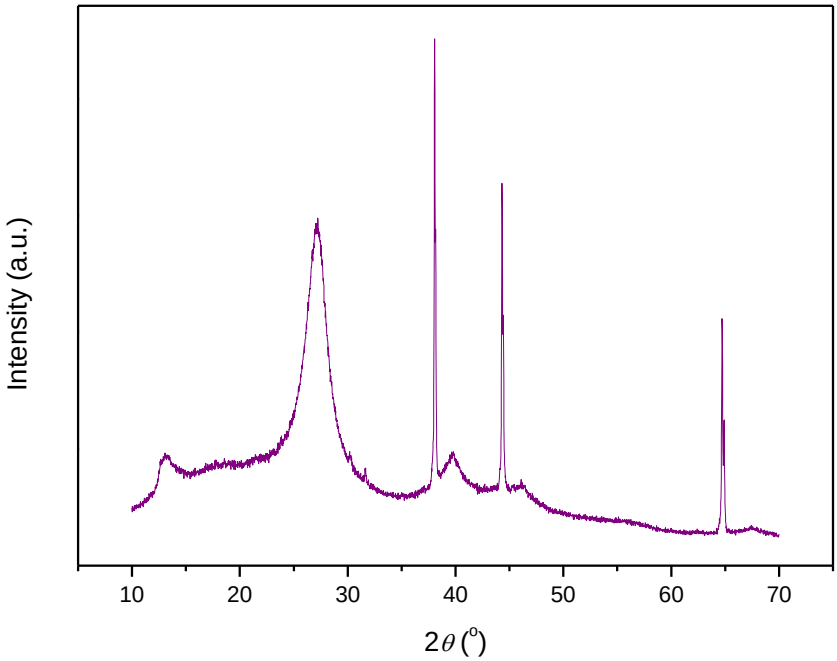

Figure 2.11: PXRD pattern of Pt loaded C_xN_y (on an Al sample holder).

2.5 Sacrificial Reagent in Photocatalytic Reaction

For the measurement of H_2 evolution, triethanolamine (TEA) is used as the sacrificial reagent in the reaction. TEA acts as an electron donor and is oxidised by the photogenerated holes instead of water so that O_2 formation is suppressed and the oxidation progress becomes irreversible.[19] Compared with some other commonly used sacrificial reagents, such as methanol, ethanol and ethylenediaminetetraacetic acid (EDTA), TEA shows the highest efficiency in terms of hydrogen evolution rate.[18]

2.6 Characterisation

2.6.1 Elemental Analysis

Since the amount of evaporated cyanamide during calcination far exceeds that remaining as polymerised product on the macropores, the amount of C_xN_y percentage was determined by elemental analysis.

The elemental analysis results are shown in Table 2.5. It is obvious that the amount of

carbon and nitrogen is increasing with increasing the amount of the precursor. As there was carbon in both pure Mac-SiO_2 and Mac-ZrO_2, the polystyrene was not fully decomposed. The C/N atomic ratio in Table 2.5 is recalculated eliminating the trace amounts of carbon in the Mac-SiO_2 which remain as a consequence of the calcination of the polystyrene template. The analysed C/N atomic ratio is close to 0.67 in all cases, which is in accordance with the pure bulk C_xN_y described in Section 2.1. It is interesting to see that when relatively low concentration of cyanamide is impregnated into Mac-SiO_2, the nitrogen mass is zero and the carbon mass is close to that of pure Mac-SiO_2 (the slight difference is due to the fact that the Mac-SiO_2 used in the samples are not always made from the same batch). It suggests that almost nothing is coating onto Mac-SiO_2 when little amount of cyanamide is employed. Presumably this is due to the low probability of polymerisation at very low concentration resulting in complete evaporation of the precursor. Loadings between 6.6 and 28.2 wt % (C_xN_y/Mac-SiO_2) were achieved as shown in Table 2.5.

Table 2.5: CHN test of C_xN_y/Mac-SiO_2 and C_xN_y/Mac-ZrO_2 composites. Samples S0~S3 are C_xN_y/Mac-SiO_2 composites with different loadings, and Sample Z1 and Z2 are C_xN_y/Mac-ZrO_2 composites. "Raw materials" column refers to the amount of CA and macroporous materials used for synthesis. For example, Sample S0 was synthesised using 20 mg CA and 120 mg Mac-SiO_2.

Name (C_xN_y %)	C %	H %	N %	Rest %	Analysed C/N atomic ratio	Raw materials (CA /Mac) (mg)
Mac-SiO_2 (-)	0.13	0	0	99.87	-	-
S0 (0%)	0.063	0	0	99.94	-	20/120
S1 (6.6%)	2.597	0	4.113	93.29	0.632	40/120
S2 (12.8%)	4.765	0.457	7.992	86.79	0.642	52.5/90
S3 (28.2%)	10.62	0.66	17.68	71.04	0.676	90/90
Mac-ZrO_2 (-)	0.837	0	0	99.163	-	-
Z1 (3.6%)	2.06	0	2.26	95.68	0.650	30/90
Z2 (22.7%)	8.886	0.315	14.223	76.58	0.663	75/90

2.6.2 Powder X-ray Diffraction

Fig. 2.12 shows the PXRD patterns of the samples that C_xN_y coating on macroporous silica (Mac-SiO_2). Pure Mac-SiO_2 show characteristic peak at ~22°, indicating that SiO_2 was obtained. As can be seen from the patterns, C_xN_y peaks cannot be observed for the samples with low concentration infiltration (below 12.8%). Since C_xN_y has graphitic structure, the signal can only appear when the quantity of layers is adequate for PXRD detection. This phenomenon should be attributed to the fact that large amount of cyanamide are lost during calcination and only a small quantity of C_xN_y are formed, limiting the layers of C_xN_y graphitic structure which cannot be detected by PXRD. The sample with 28.2% and 47.5% C_xN_y possesses a low intenity peak at 26.3°, which overlaps the SiO_2 peak at 22° and makes the C_xN_y peak at 26.3° difficult to distinguish. Besides the loading at 12.8 % shows evidence of peak broadening at 13.2° and 26.3° (signals for C_xN_y), indicating that above *ca* 10% layer formation is occurring.

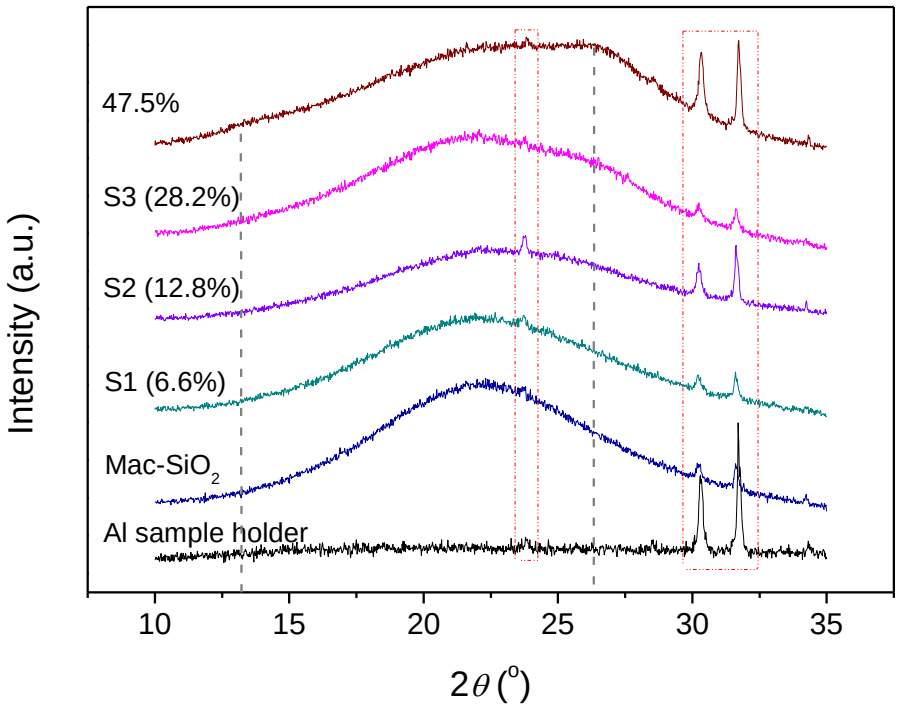

Figure 2.12: PXRD patterns of Mac-SiO_2 and C_xN_y/Mac-SiO_2 composites. The three peaks circled by red dot lines are from the slightly contaminated Al sample holder.

Fig. 2.13 shows the PXRD patterns of Mac-ZrO_2 and C_xN_y/Mac-ZrO_2 composites with different loadings. Pure Mac-ZrO_2 show characteristic peak at 30°, 35°, 50.5°, 60° and 62.5°, indicating that single phase of ZrO_2 was obtained. The C_xN_y peaks at 13.2° and 26.3° is not obvious in the patterns, similar to C_xN_y/Mac-SiO_2 samples S1 and S2 (C_xN_y wt %≤12.8%).

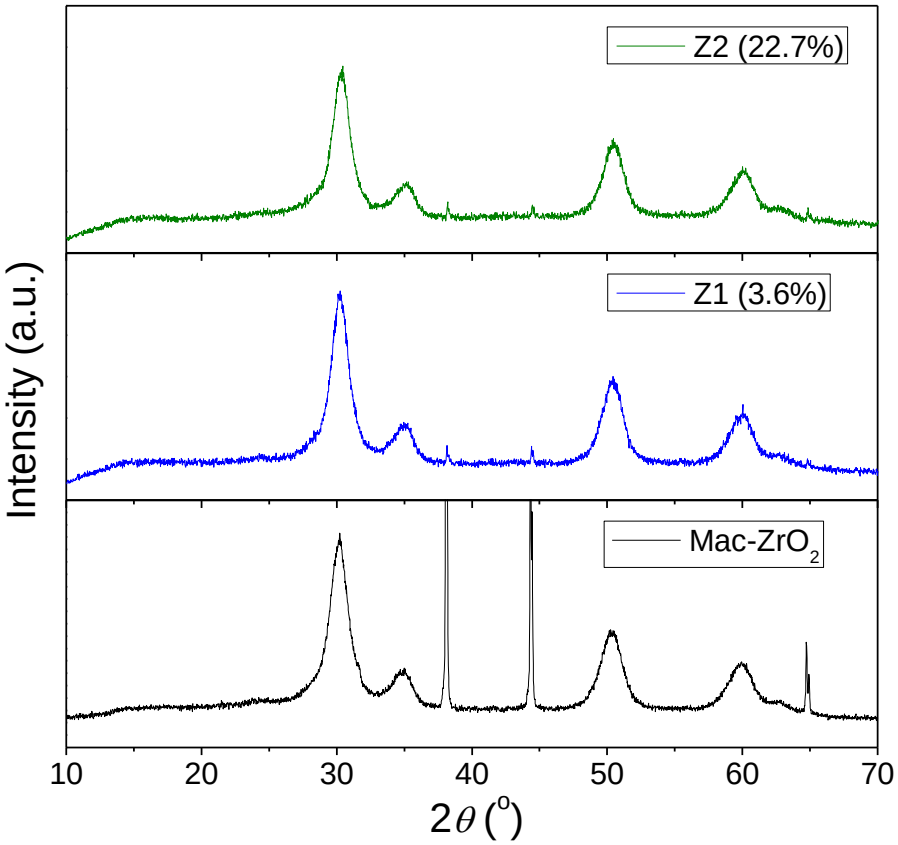

Figure 2.13: P XRD patterns of Mac-ZrO_2 and C_xN_y/Mac-ZrO_2 composites.

2.6.3 Fourier Transform Infrared Spectroscopy

Fig. 2.14 plots the FT-IR spectra of Mac-SiO_2 and C_xN_y/Mac-SiO_2 composites with various C_xN_y contents. For the Mac-SiO_2, there are several typical features: the bending vibration at around 800 cm^{-1}, the Si–O–Si asymmetric stretching at around 1100 cm^{-1}, the –OH bonding at 3500 cm^{-1}.[72] The peak at around 1600 cm^{-1} is the H–O–H group.[73] Significant feature of C_xN_y, i.e. the vibrations at 1200-1600 cm^{-1}, starts to appear for Sample S1 (beyond 6.6%).

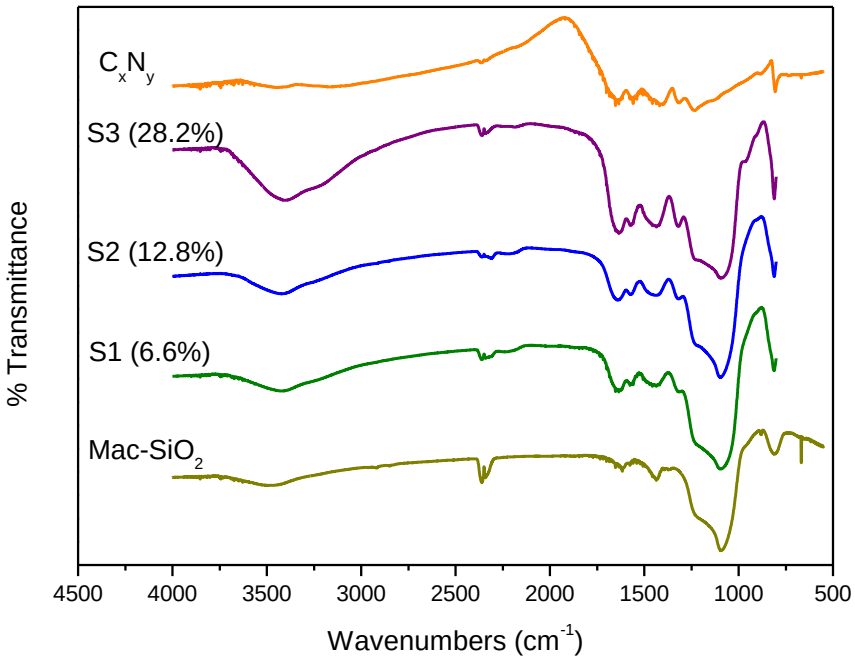

Figure 2.14: FT-IR spectra of C_xN_y/Mac-SiO_2 composites, compared with Mac-SiO_2 and C_xN_y.

Fig. 2.15 plots the FT-IR spectra of Mac-ZrO_2 and C_xN_y/Mac-ZrO_2 composites with various C_xN_y contents, compared with C_xN_y. As can be seen from the spectra, Sample Z2 (22.7 wt % of loading) start to show vibrations at 1200-1600 cm^{-1} and 800 cm^{-1}, which are in line with the spectrum of C_xN_y. It is interesting to see that the loading on Mac-ZrO_2 is different from that onto Mac-SiO_2. An absorption peak at 2050 cm^{-1} exists in Sample Z1 and Z2, which is assumed to be N=C=N stretching (from 'The Sadtler Handbook of Infrared Spectra'). This phenomenon should be attributed to the incomplete polymerisation of cyanamide. However, it is still possible that ZrO_2 is involved in the reaction and formed complexes. As the time limitation, the reason and conclusion for this have not been investigated in this thesis.

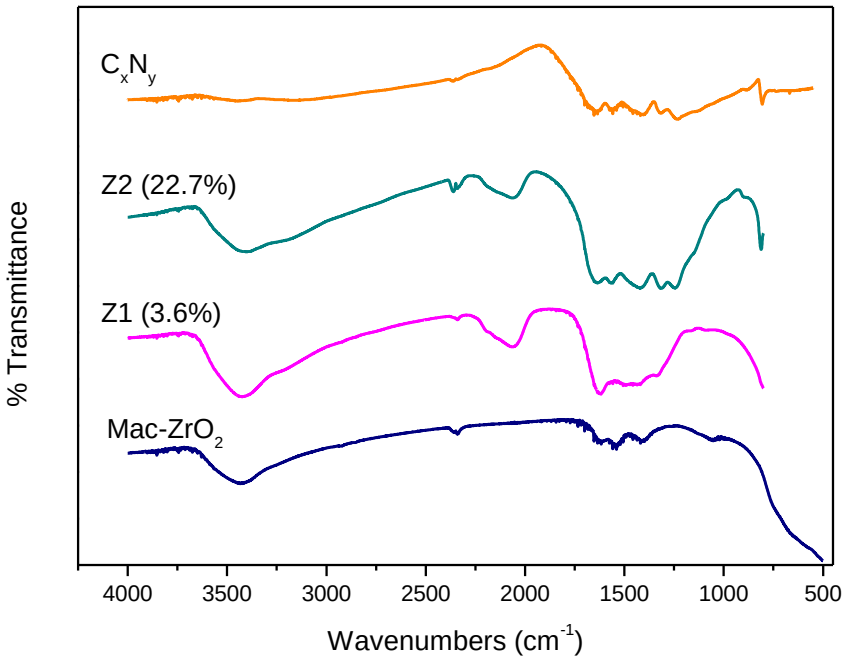

Figure 2.15: FT-IR spectra of C_xN_y/Mac-ZrO_2 composites, compared with Mac-ZrO_2 and C_xN_y.

2.6.4 Nuclear Magnetic Resonance Spectroscopy

CPMAS NMR spectroscopy was performed on a sample with 15.9 wt % and the results are shown in Fig. 2.16(a). It is clear that the main features are again signals at δ 157 and 164 ppm which correspond to the tri-s-triazine type motif shown in Fig. 1.7b. There is also evidence of trace impurities at 20 and 60 ppm that are likely to originate from incomplete combustion of polystyrene as evidenced in trace carbon content in the elemental analysis of Mac-SiO_2. What is clear is that polymerisation has occurred and that the local structure of the 'carbon nitride' in the composites is very similar to bulk 'carbon nitride' described in Section 2.1 (Fig. 2.16b).

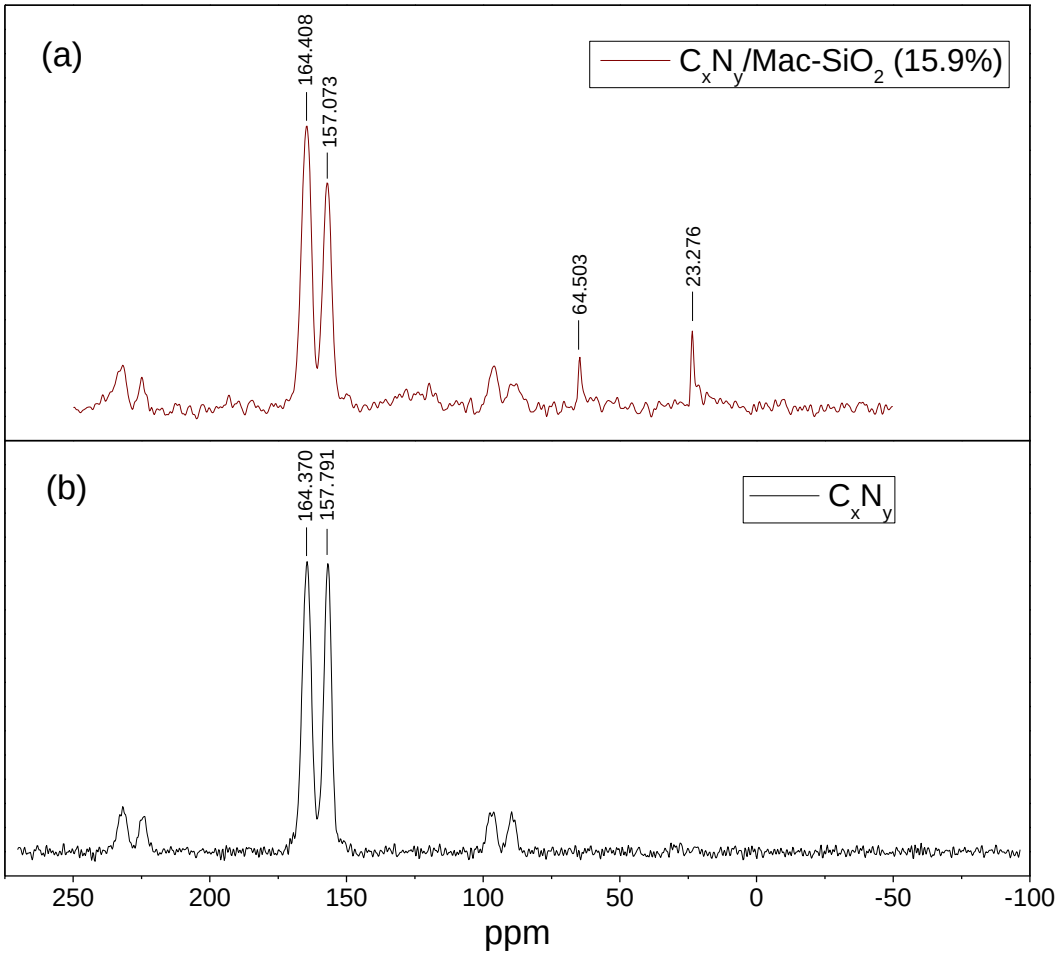

Figure 2.16: NMR spectra of (a) C_xN_y/Mac-SiO_2 composite (15.87%) and (b) C_xN_y.

2.6.5 Electron Microscopy

The morphology of the C_xN_y/M-SiO_2 composites was characterised by a variety of microscopy techniques including SEM, TEM, EDX and EELS. The TEM and EELS was performed at the University of Leeds by Prof Rik Brydson. Fig. 2.17 shows the SEM images of pure Mac-SiO_2 and the coated samples. The 3DOM structure is clearly seen. Comparing the composite images to that of Mac-SiO_2 it can be seen that as the loading of C_xN_y increases there is greater evidence of extra material on the surface and in the surface pores. C_xN_y for the higher loaded samples S2 and S3 images from different regions show areas where extra material is absent or present indicating that the distribution of carbon nitride is not totally homogeneous.

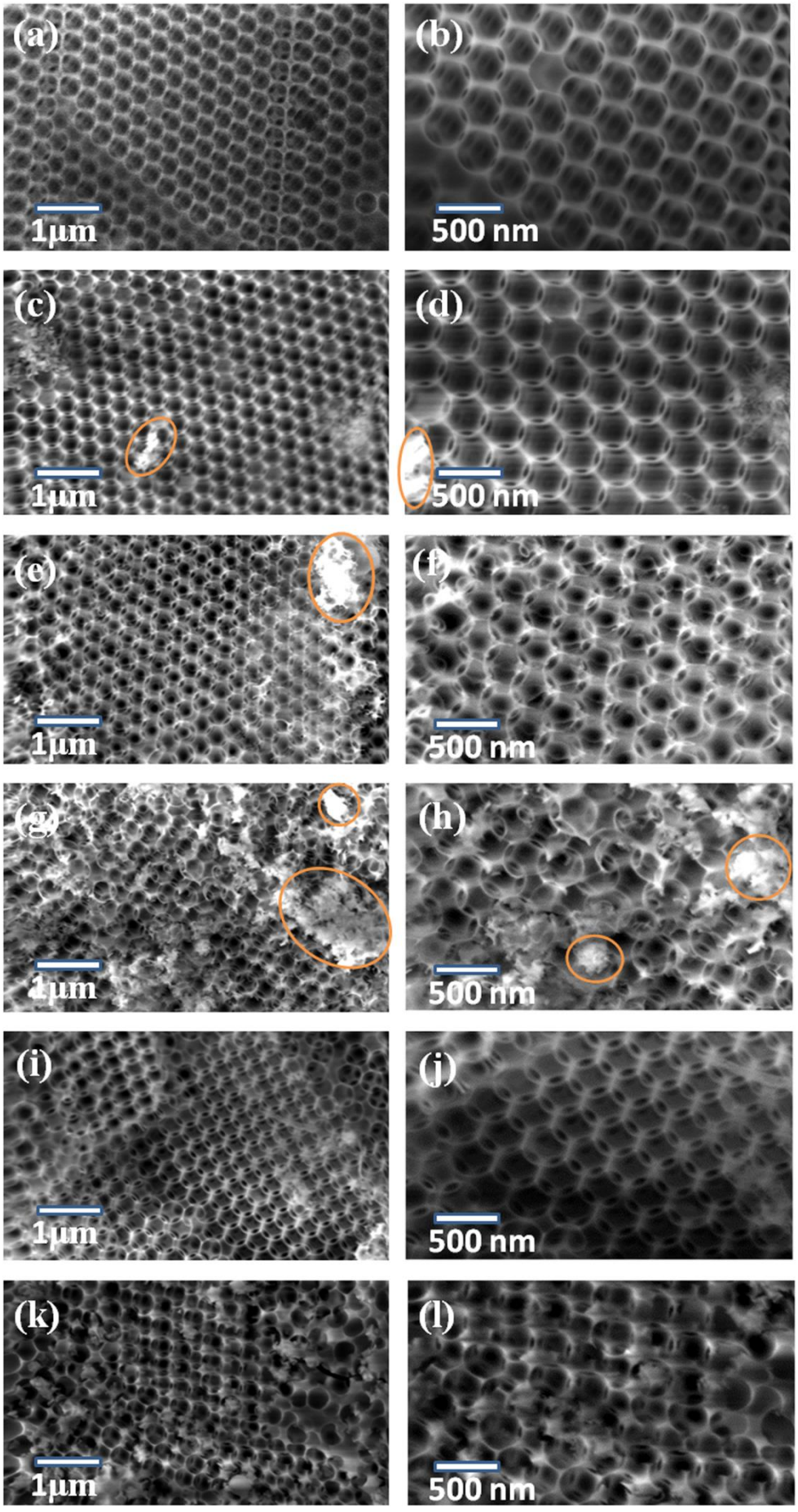
(a)
1μm
(b)
500 nm
(c)
1μm
(d)
500 nm
(e)
1μm
(f)
500 nm
(g)
1μm
(h)
500 nm
(i)
1μm
(j)
500 nm
(k)
1μm
(l)
500 nm

Figure 2.17: SEM images of (a) Mac-SiO_2 (low mag.); (b) Mac-SiO_2 (high mag.); C_xN_y/Mac-SiO_2 composites (c) S1 (low mag.); (d) S1 (high mag.); (e) and (g) S2 (low mag.); (f) and (h) S2 (high mag.); (i) and (k) S3 (low mag.); (j) and (l) S3 (high mag.). Circled in orange are the extra materials (C_xN_y) on the surface of Mac-SiO_2.

Fig. 2.18 shows the SEM images of Mac-ZrO_2 and C_xN_y/Mac-ZrO_2 composites. All the samples show macroporous structure with interconnected windows. The morphology of these samples is the same, and in the region detected, no blockage was found. However, taking Mac-SiO_2 as a reference, the absence of C_xN_y clusters cannot be used for a proof of homogeneous coating since blocked regions may still exist in regions not analysed.

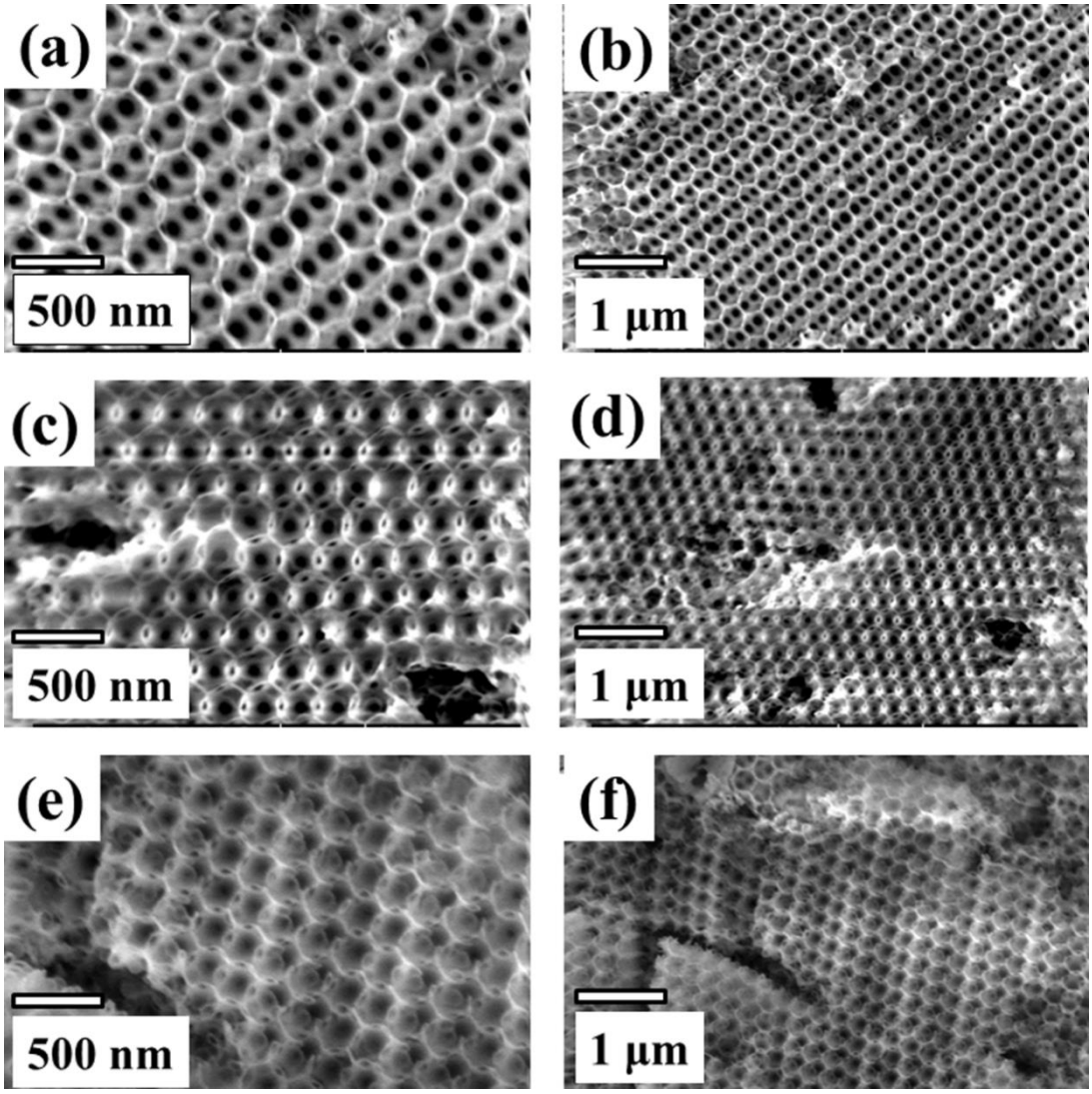

Figure 2.18: SEM images of (a) Mac-ZrO_2 (low mag.); (b) Mac-ZrO_2 (high mag.); C_xN_y/Mac-ZrO_2 composites (c) Z1 (low mag.); (d) Z1 (high mag.); (e) Z2 (low mag.); (f) Z2 (high mag.).

Fig. 2.19 shows the TEM images of C_xN_y/Mac-SiO_2 composite S1 before and after photocatalysis. The TEM samples were prepared by crushing a composite and dispersing the material in methanol before evaporating onto a copper TEM grid. Analysis of several areas showed that carbon nitride material is distributed through the volume of the macroporous powders but that the coating is not homogeneous as shown in Fig. 2.19 (a) and (d) C_xN_y. Pt nanoparticles are observed in the TEM images (Fig. 2.19 b, c, e and f) and the average size of Pt nanoparticles is approximately 2.0 nm (analysed by DigitalMicrograph) (Fig. 2.20). No big difference is found between the samples before and after photocatalysis indicating that the composites are stable to photocorrosion.

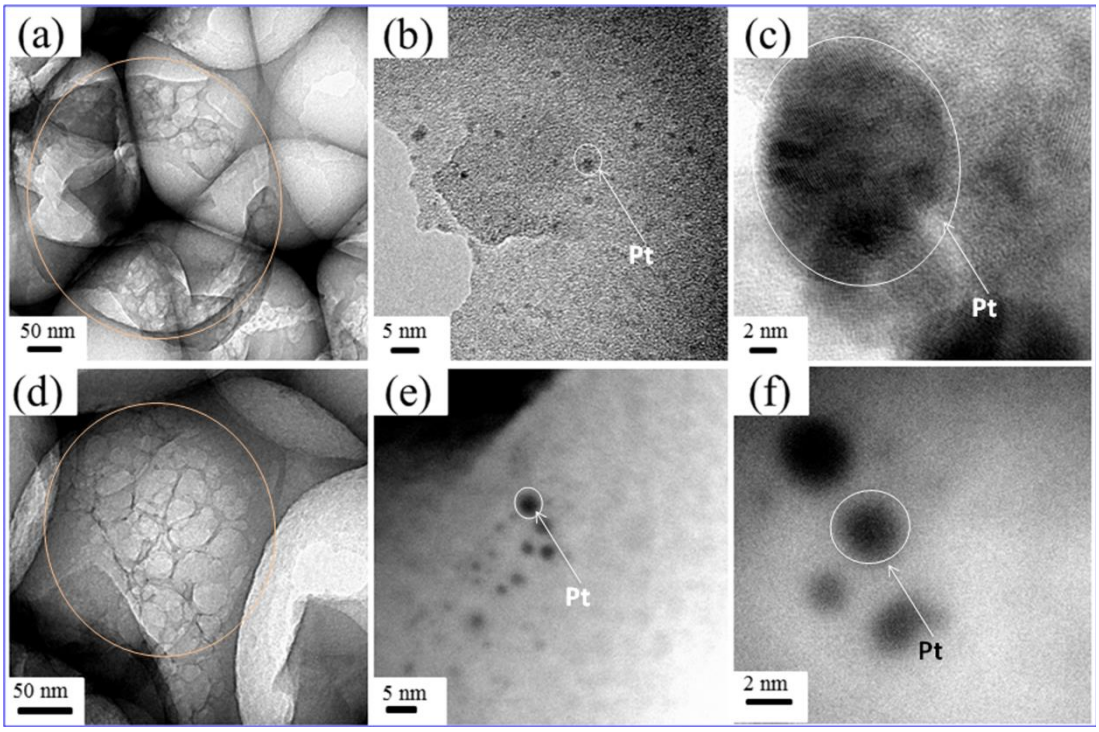

Figure 2.19: TEM images of C_xN_y/Mac-SiO_2 composite S1: (a), (b) and (c) before photocatalysis (in different mag.); (d), (e) and (f) after photocatalysis (in different mag.). C_xN_y coatings are shown in the circled regions.

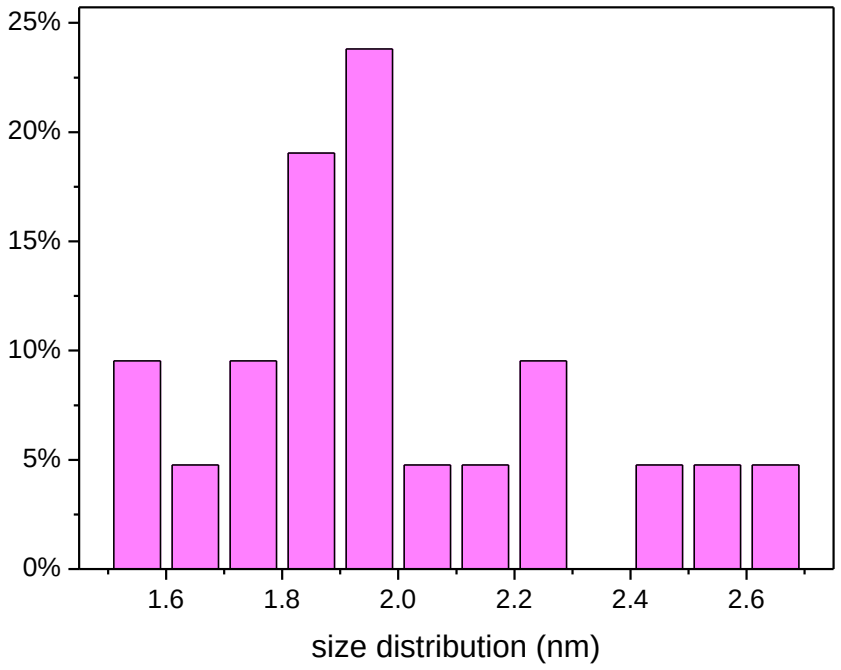

Figure 2.20: Size distribution of Pt nanoparticles on C_xN_y/Mac-SiO_2 composite (S1).

Electron energy loss spectroscopy (EELS) was also used to analyse the distribution of carbon and nitrogen on Mac-SiO_2. Fig. 2.21 shows the EDX and elemental map images of a C_xN_y/Mac-SiO_2 (15.4%) composite. It is obvious that the shapes in elemental mappings of C and N are the same while those of O and Si look similar. In other words, the positions of C_xN_y and Mac-SiO_2 in the fragment are corresponding to Fig. 2.21 (c) and (e), respectively. As can be seen from the two figures, C_xN_y does not cover the entire region in Mac-SiO_2, indicating an inhomogeneous coating of thin sheets.

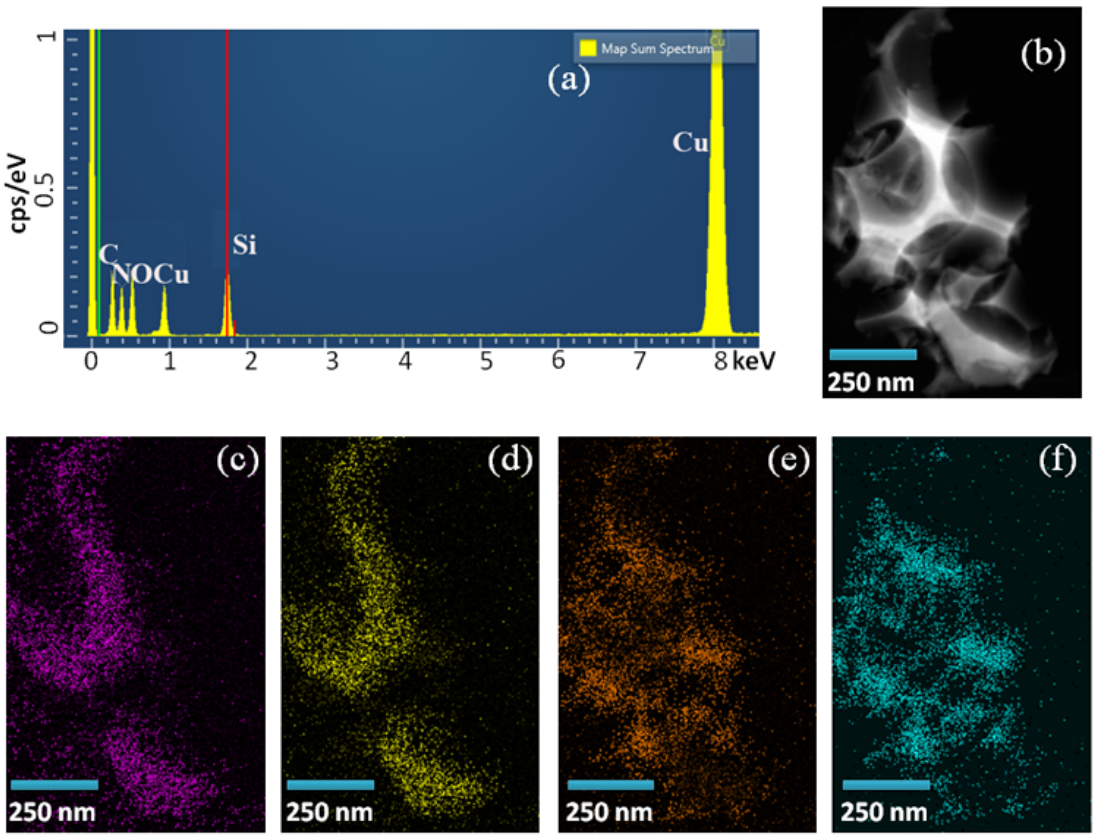

Figure 2.21: C_xN_y/Mac-SiO_2 (15.4%) : (a) EDX image; (b) electron micrograph of a fragment of the sample; elemental mapping images of (c) carbon, (d) nitrogen, (e) oxygen, (f) silicon.

2.6.6 Surface Area Measurement

The surface area was measured using nitrogen adsorption and analysed using Brunauer–Emmett–Teller (BET) theory. Table 2.6 shows the surface area of Mac-SiO_2, Mac-ZrO_2 and their composites with C_xN_y. As can be seen from the table, Mac-SiO_2 has a high surface area which reduces on addition of carbon nitride. The walls of Mac-SiO_2 are known to be amorphous when made from solution and exhibit a higher surface area than macroporous materials made from crystalline material, since silica is less dense so that nitrogen used to measure surface area can penetrate the walls. For example, Mac-ZrO_2 exhibits a lower surface area (Table 2.6). Generally, the macroporous structure supports a carbon nitride with large surface area. The macropores will prevent agglomeration of the carbon nitride sheets. Presumably the reduction in surface area for Mac-SiO_2 is due to partial coverage of the amorphous walls. For Mac-ZrO_2 the surface area increases slighty with a small addition of C_xN_y.

Although at high loadings the presence of C_xN_y in the macroporous structure is likely to block some of the pores, the surface area values of C_xN_y/Mac-SiO_2 and C_xN_y/Mac-ZrO_2 are still approximately 100 times larger than that of bulk C_xN_y.

Table 2.6: BET surface area of Mac-SiO_2 and Mac-ZrO_2 and their composites with C_xN_y

BET surface area measurement (m^2/g)	
Mac-SiO_2	94.15 ±1.36
C_xN_y /Mac-SiO_2 (S1)	56.35 ±0.54
C_xN_y /Mac-SiO_2 (S2)	53.46 ±0.60
C_xN_y /Mac-SiO_2 (S3)	49.58 ±0.82
Mac-ZrO_2	25.62 ±0.34
C_xN_y /Mac-ZrO_2 (Z1)	28.22 ±0.70
C_xN_y /Mac-ZrO_2 (Z2)	17.87 ±0.31
Bulk C_xN_y	0.61 ±0.19

2.6.7 Diffuse Reflectance and Absorbance UV-Vis Spectroscopy

For ordered macroporous materials, stop bands detected by solid-state UV-Vis diffuse reflectance spectroscopy are typical features to determine the photonic properties. Equation 2.1 (see section 1.3.4), is used to calculate the volume fraction of Mac-SiO_2.

$$\lambda = 2d_{hkl}/m[\varphi n_{wall} + (1-\varphi)n_{void}] \qquad (2.1)$$

Fig. 2.22 shows the two stop bands of Mac-SiO_2 material shifting on filling with different fluids, and the positions of them are shown in Table 2.7. The two bands can be indexed to (111) and (220) Bragg reflections using Equation 2.1, respectively.[64] It is observed that the stop bands are shifted to longer wavelengths when filled with fluid with higher refractive index, which is in accordance with the Equation 2.1. The volume fraction can be calculated using Equation 2.1, as shown in Table 2.8. The values calculated with the two fluids are different, due to different wettings between

the Mac-SiO_2 and solvents.

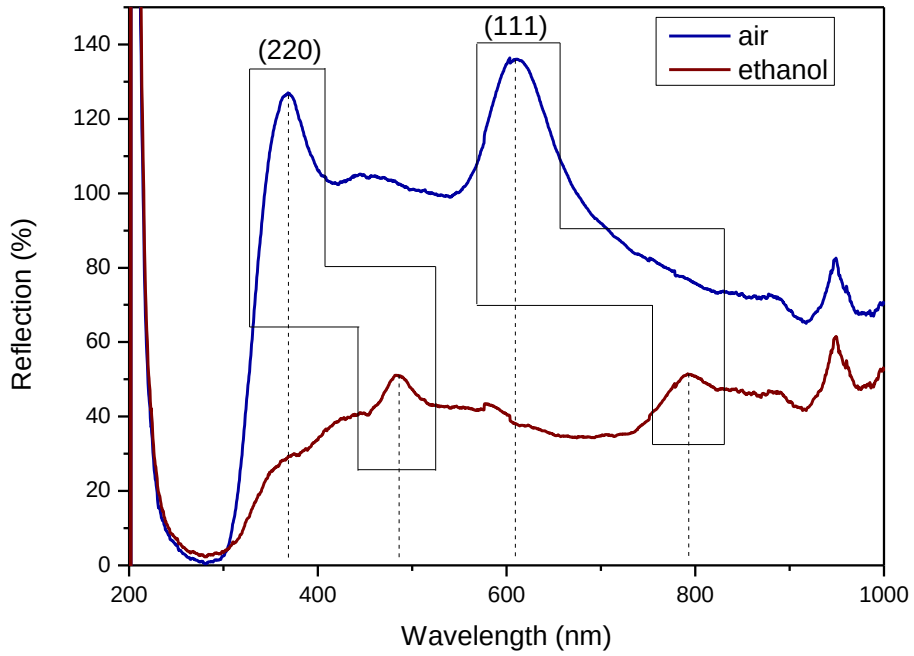

Figure 2.22: Diffuse reflectance spectra of Mac-SiO_2 filled with air and ethanol, respectively.

Table 2.7: The stop band positions of Mac-SiO_2 filled with different fluids.

	(220)	(111)
air	369 nm	611 nm
ethanol	484 nm	793 nm

Table 2.8: Theoretical refractive index of air and ethanol and the corresponding calculated volume fraction of Mac-SiO_2

	Refractive index (n_{void})	Volume fraction (φ)
air	1.00	0.14
ethanol	1.36	0.25

Fig. 2.23 plots the diffuse reflectance of Mac-SiO_2 and C_xN_y/Mac-SiO_2 composites with various C_xN_y contents. As can be seen from the spectra, the stop bands still exist after coating with C_xN_y. The stop band at 369 nm shows an apparent drop in intensity

which is due to the superposition of the absorption edge of C_xN_y. The drop in intensity of the stop band peak at 610 nm indicates that some inhomogeneous coating of C_xN_y disorders the periodicity of 3DOM structure, which is consistent with the SEM and TEM. When the C_xN_y content is higher than 12.1%, the stop band begins to disappear, indicating that the macropores contain an inhomogeneous distribution of C_xN_y. No obvious red shift is observed with increasing the C_xN_y content again indicative of inhomogeneous coverage. If there were homogeneous coating of an adequate thickness on the wall of the macroporous materials, the volume percentage of wall material (φ) would be changed and the stop band position would shift according to Equation 2.1. However, this phenomenon does not occur in this thesis.

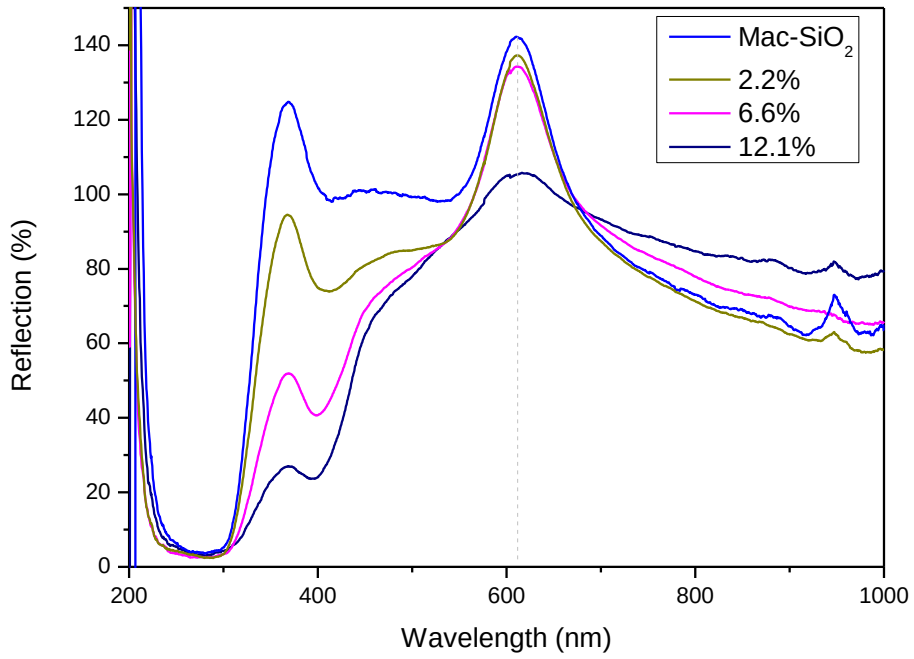

Figure 2.23: Diffuse reflectance of Mac-SiO_2 and C_xN_y/Mac-SiO_2 composites with various C_xN_y contents.

Fig. 2.24 shows the diffuse reflectance spectra of Mac-ZrO_2 and C_xN_y/Mac-ZrO_2 composites with various C_xN_y contents. As shown in the graph, the stop band of Mac-ZrO_2 is not as sharp as that of Mac-SiO_2 due to a less ordered periodic structure. The stop band position of Mac-ZrO_2 is also red shifted compared with that of Mac-SiO_2, because of a different shrinkage during calcination. With increasing the

content of C_xN_y, the only obvious (111) stop band at 541 nm reduces without blue or red shift, presenting the same trend as the C_xN_y/Mac-SiO_2 composites.

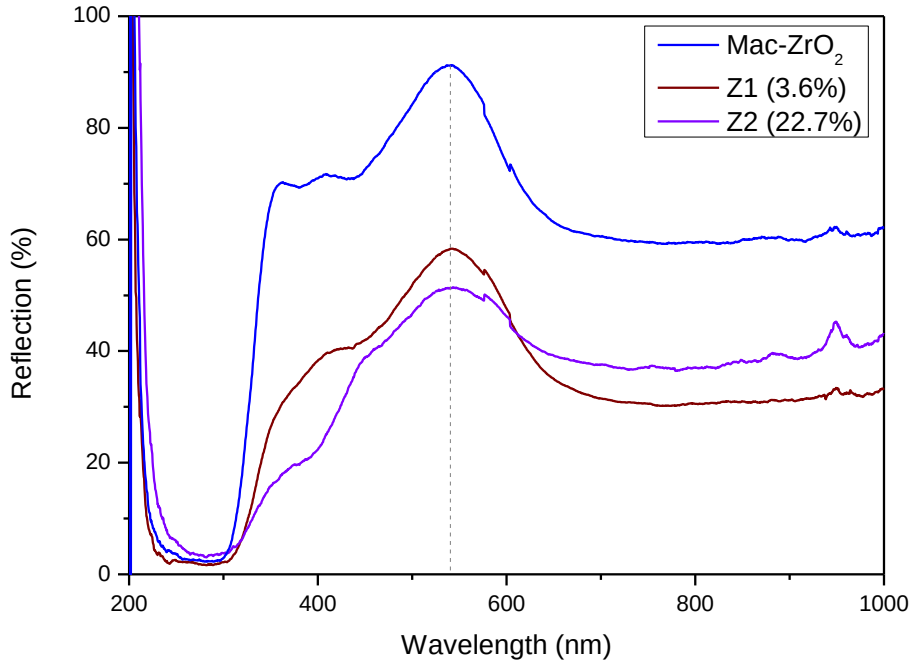

Figure 2.24: Diffuse reflectance of Mac-ZrO_2 and C_xN_y/Mac-ZrO_2 composites with various C_xN_y contents.

2.7 Photocatalytic Testing

As described in Section 1.3.3, C_xN_y shows photocatalytic activity in the bulk phase for hydrogen production using a sacrificial electron donor. Enhanced rates have been reported for g-C_3N_4 in exfoliated nanosheets and mesoporous materials due to an increase in the surface area.[49, 51, 58] The band structure of C_xN_y spans the reduction and oxidation electrode potentials of water, suggesting that it can at least achieve the half reactions of water splitting in the presence of sacrificial agent. In this thesis, triethanolamine is used as the sacrificial agent in the hydrogen evolution reactions. 3 wt % Pt was loaded onto the surface of bulk C_xN_y and C_xN_y/Mac-SiO_2 samples corresponding to the C_xN_y content determined by elemental analysis. All the samples were irradiated under visible light > 400 nm.

First of all, the photocatalytic activity was tested for bulk C_xN_y. 40 mg bulk C_xN_y powder with 3 wt % Pt under visible light was irradiated (Fig. 2.25a Curve ii) and also 40 mg bulk g-C_xN_y without Pt loading for comparison (Fig. 2.25a Curve i). As can be seen from the graph, C_xN_y with Pt shows good photocatalytic activity. Large amounts of H_2 was generated in 70 hours and the amounts for around every 24 hours are 232, 213, 188 μmol, respectively. The implication here is that the catalytic activity is decreasing overtime, which is in contrast to that previously reported. This could be due to loss of Pt, aggregation of the photocatalytic particles (both C_xN_y and Pt) or chemical degradation. The total number of moles of hydrogen (633 μmol) exceeds that of C_2N_3H (see Section 2.6.1) (298.5 μmol) indicating that the reaction is catalytic. However, if it is assumed that hydrogen is from the complete mineralisation of C_2N_3H, the reaction should follow Equation 2.2 indicating that in excess of 2.5 equivalents of H_2 per mole of C_2N_3H is required to confirm a truly catalytic reaction:

$$2C_2N_3H + 8H_2O = 5H_2 + 4CO_2 + 3N_2 \qquad (2.2)$$

With regard to the sample without Pt, very little H_2 is generated, a mere 3 μmol in 20 hours, which shows the critical role of the Pt cocatalyst.

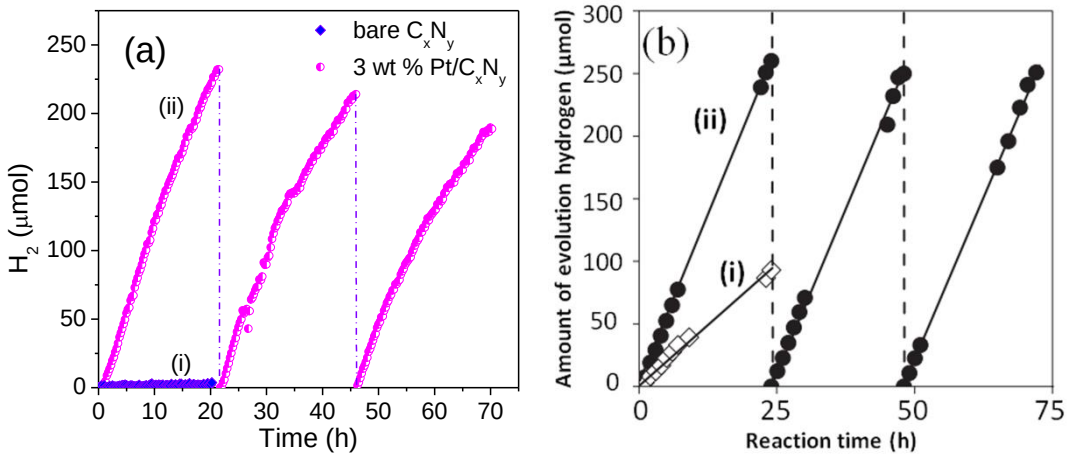

Figure 2.25: H_2 evolution of (a) 40 mg bulk C_xN_y under visible light by (i) bare C_xN_y and (ii) 3 wt % Pt loading C_xN_y, respectively; (b) 100 mg bulk g-C_3N_4 under visible light reported in the literature by (i) bare g-C_3N_4 and (ii) 3 wt % Pt loading g-C_3N_4, the same with Fig. 1.13 a.[18]

Fig. 2.25b shows the reported hydrogen evolution with 100 mg bulk g-C_3N_4 with and without 3 wt % Pt loading under visible light, respectively. From Fig. 2.25b we can compare hydrogen evolution in this thesis with the reported yield. Although the amount of C_xN_y used for H_2 evolution used is less than half of that in the reported experiment, similar amount of hydrogen was generated. The difference between the activities can be due to a number of factors relating to the experimental set-up, resulting in different irradiance and hence rate.

The rate reported in the literature is relatively stable without curvature, and the photodegradation is not observed in Fig. 2.25b. However, the considerable H_2 amount generated by g-C_3N_4 with no Pt is different to our experiment. In this literature and some other ones, g-C_3N_4 is regarded as a metal-free photocatalyst,[18, 42] but we have not observed any evidence of this. According to our data, although bare C_xN_y can produce a small quantity of hydrogen (Fig. 2.25a Curve i), we cannot consider it as an efficient photocatatylst.

The photocatalytic activity of C_xN_y/Mac-SiO_2 composites with various C_xN_y contents was studied, and compared to the same mass of Pt-loaded bulk C_xN_y. Fig. 2.26 shows the hydrogen evolution of C_xN_y/Mac-SiO_2 composites with different C_xN_y percentages and the control experiments, respectively. It is obvious that C_xN_y in Mac-SiO_2 produces far more H_2 than in the bulk phase, up to 20-30 times as much, depending on the loading. The reason for this significant increase should be attributed to the macroporous structure, which provides high surface area and potentially takes advantage of photonic properties. Even though C_xN_y in the composite is not homogenously coated on the wall of the macropores, the macroporous structure provides a support, and prevents the aggregation and formation of crystalline graphitic like structures. As can be seen from the graph, all the composites S1-S3 show comparable rates in the first 5 hours, but after that it starts to diverge as the activity

drops. Given that the surface areas (Table 2.6) are of a similar magnitude it may be expected that the activity of the samples should be similar. Loading more C_xN_y may simply increase the number of layers accommodated in the macropores and on the surface of the particles and not increase the amount of catalytically active surface area. At times longer than 5 h deviation is observed. The cause is not clear, however, the amount of C_xN_y is unlikely to be the cause because all samples behave similarly. The activity does not appear to scale with loading. This may be due to variation in the solution volume as reaction proceeds. Typically the reaction volume reduces by 30-50 % during a 24-hour period.

We primarily assume that this issue is attributable to the configuration of the photocatalytic equipment. Since some of the water evaporates, the concentration of the sacrificial agent and photocatalyst are changing throughout the photoreaction. If the photocatalyst in too concentrated the light does not penetrate the full volume of the reaction. Due to the time limit, we have not tested the relationship between the yield and sacrificial agent concentration and water content. If the photocatalytic activity is not the same even under the same concentration, other factors should be taken into consideration, such as the solution pH. More experiments are required to confirm these results and ideally examine other compositions. Nevertheless the increase in activity with respect to the bulk materials is clear, especially for the lowest loadings.

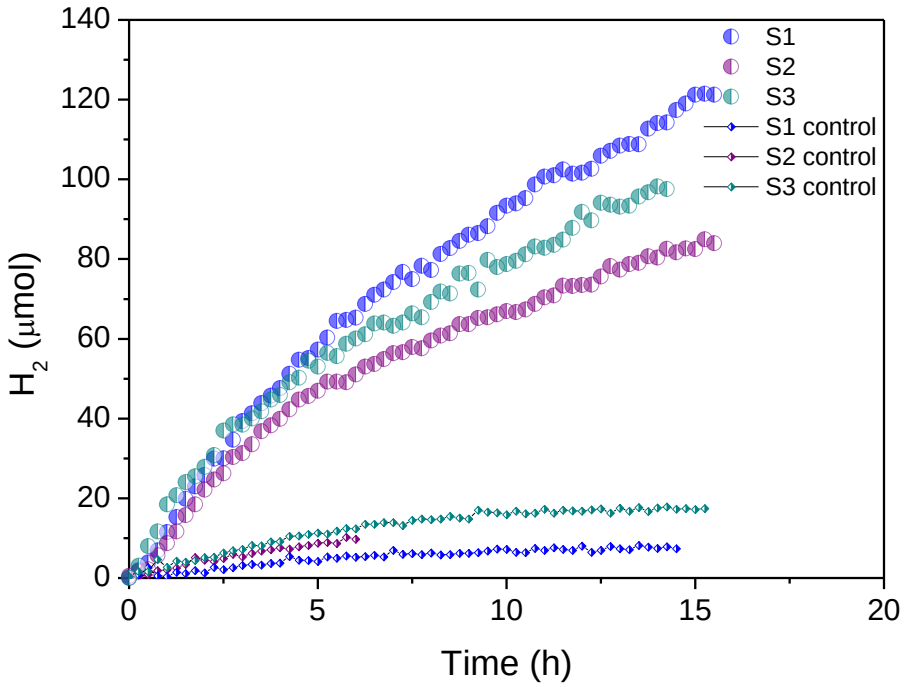

Figure 2.26: Hydrogen evolution of C_xN_y/Mac-SiO_2 composite with various C_xN_y contents, e.g. (blue) S1, (purple) S2 and (green) S3 and their control groups of 4.6 mg (S1), 8.9 mg (S2) and 19.7 mg (S3) C_xN_y with 3 wt % Pt.

For the C_xN_y/Mac-SiO_2 composite S1, repeated photocatalytic reactions were run to verify that it is acting as a photocatalyst. As can be seen from Fig. 2.27, hydrogen was generated consistently when irradiated with visible light, although the rate was not completely stable in these tests. Some reduction in rate is observed between the first two runs but then recovers somewhat in the third run. No hydrogen was generated in the dark, showing that the generated hydrogen is not from thermal decomposition and is a light activated process. From the elemental analysis of the sample, 4.59 mg of C_2N_3H is contained in the sample (Table 2.5). For 4.59 mg C_2N_3H, 170 μmol hydrogen would be generated according to Equation 2.2. In the actual experiment, about 300 μmol hydrogen is formed, exceeding the value 170 μmol. It shows that C_2N_3H is acting as a photocatalyst rather than photocorrosion or thermal decomposition occurring.

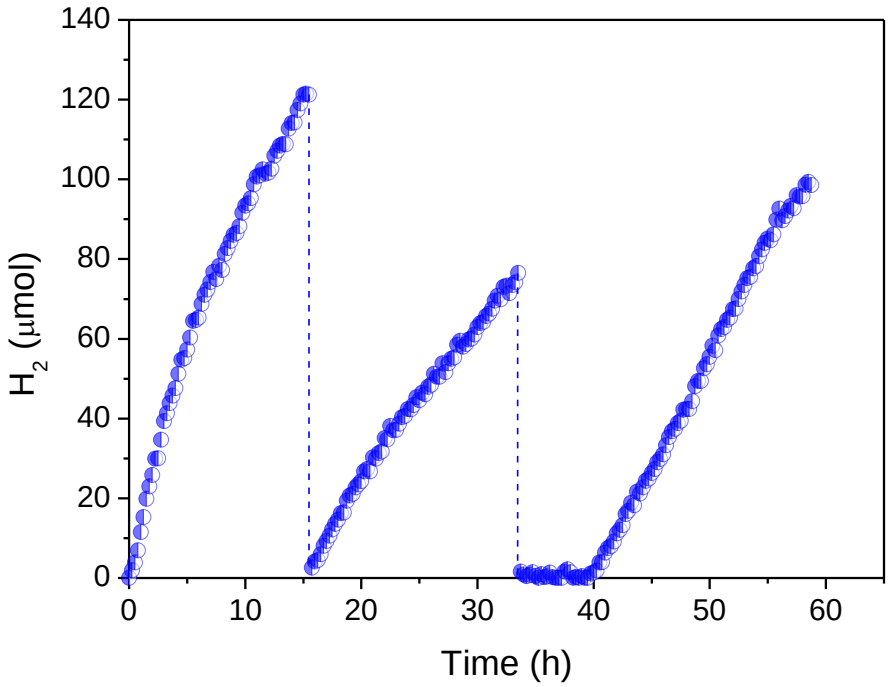

Figure 2.27: Hydrogen evolution of C_xN_y/Mac-SiO_2 composite Sample S1. During the 33.5-39.5 h the sample was run in the dark. The gas in the system was purged twice (the two dashes).

Unfortunately due to lack of time photocatalytic experiments with the Mac-ZrO_2 composites were not performed.

Chapter 3

The initial project was to investigate the use of metal silicides as photocatalysts. Unfortunately after several months it became clear that this project was based on a result reported in the literature that could not be repeated. In this chapter a brief account of the work is presented.

3.1 $TiSi_2$ and Other Silicides as Photocatalysts

Metal silicides have been reported as potentially promising materials for photocatalysis because they can absorb a wide range of visible light. Commercially available $TiSi_2$ has been reported as a photocatalyst for hydrogen generation from water splitting without the presence of cocatalyst and sacrificial agent.[74] According to Demuth's experiment, the band gap of $TiSi_2$ is from 3.4 to 1.5 eV, covering the wavelength range of visible light (Fig. 3.1).

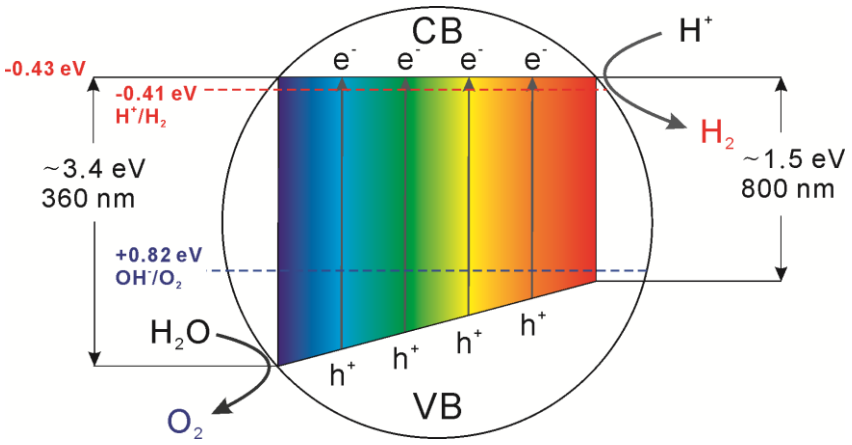

Figure 3.1: Band gap of $TiSi_2$-based semiconductor photocatalyst employed in Demuth's work. h^+ equals hole with positive charge.[74]

In Demuth's experiment, the photocatalytic activity is tested under halogen light. $TiSi_2$ powder was put in water and irradiated at 55 ^oC. Their result is shown in Fig. 3.2. As they counted H_2 yield by volume (mL), which is different with the commonly used by amount of substance (mol), the unit was converted according to the assumed a

standard atmosphere (V=22.4L/mol*n). As shown in Fig. 3.2, around 130 mL H_2 was produced in 800 h, which is approximately 5 mmol of gas under standard conditions. There was a reduction in rate in the first 300 hours, and then the rate became stable. In their report, they regarded the reduction part as the induction time, named as Phase A, and the stable region was named Phase B. In Phase A, a thermal chemical reaction with water and photocatalysis of $TiSi_2$ happened at the same time, and the catalysis centre was formed. The thermal decomposition of $TiSi_2$ is shown in Equation 3.1.

$$TiSi_2 + 6H_2O = TiO_2 + 2SiO_2 + 6H_2 \quad (3.1)$$

As seen in Equation 3.1, the thermal decomposition of $TiSi_2$ can result in the release of hydrogen, which should be treated carefully before obtaining the proof that $TiSi_2$ is a photocatalyst. To prove this, the overall H_2 yield should exceed the catalytic amount, i.e. the H_2 amount calculated by Equation 3.1 with the original $TiSi_2$ amount for the reaction. In the final part of Phase A, with the forming of TiO_2 and SiO_2, the passivation prevented $TiSi_2$ from further reaction with water. As a result, in Phase B, $TiSi_2$ only acted as a photocatalyst so that the rate of H_2 evolution kept stable. In Fig. 3.2, the red lines represent the H_2 yield while the blue ones the O_2. In Demuth literature, the reversible storage is also investigated. The O_2 curves meant that O_2 did not released from the catalyst until heated to 100 ^oC in the dark. The O_2 yield is not taken into consideration in this thesis.

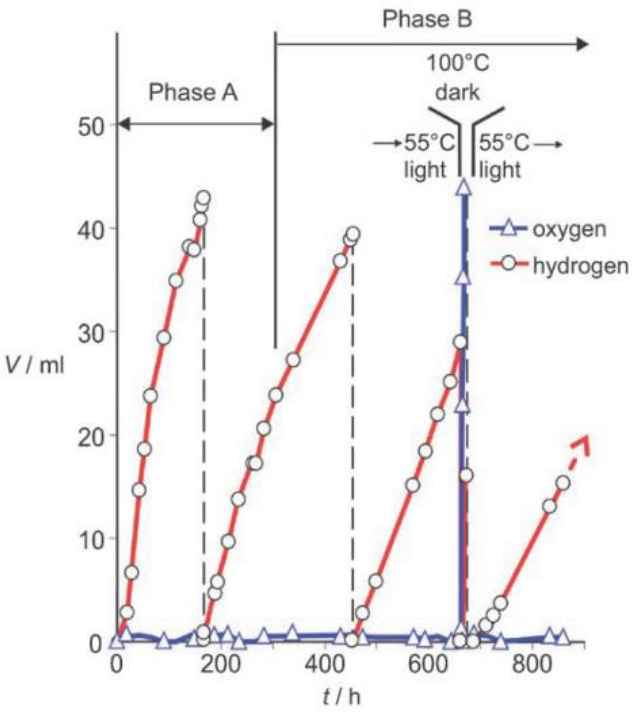

Figure 3.2: Hydrogen generation measurement in Demuth's work. In 800 h around 130 mL H_2 was produced, which approximately 5 mmol gas under standard conditions.[74]

It was also reported that temperature has a significant effect on the H_2 evolution, as shown in Fig. 3.3. The photocatalytic activity increased with raising the temperature, especially under light irradiance. Thus, a high temperature of 80 ^oC was employed in this thesis to accelerate the reaction.

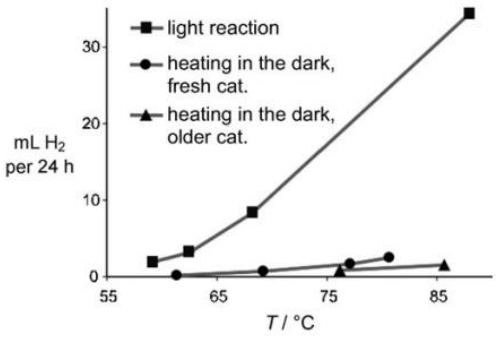

Figure 3.3: Temperature–dependent efficiency of water splitting as determined by H_2 evolution in Demuth's work.[74]

3.2 Photocatalysis Test to Identify the Authenticity of $TiSi_2$

In order to prove $TiSi_2$ to be a photocatalyst in most of these reactions, several photocatalytic reactions were carried on in this thesis. Firstly, the presence of light was controlled during the tests, in order to investigate whether the H_2 was generated in the dark. As shown Fig. 3.4, although the rate of H_2 generation showed some slight decrease in the dark, H_2 was released during the whole reaction. It cannot prove that $TiSi_2$ is a photocatalyst.

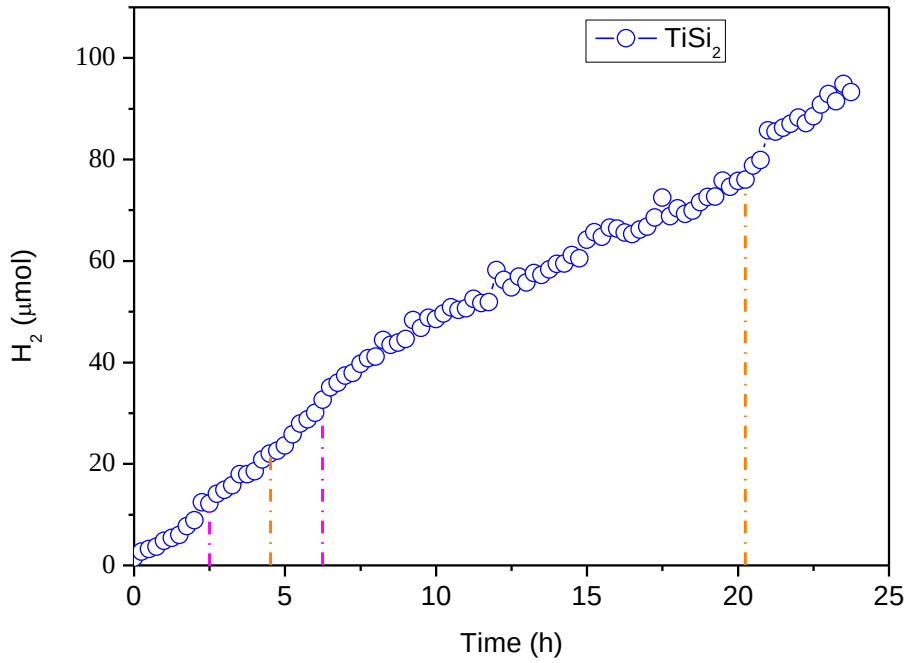

Figure 3.4: The amount of H_2 generated by $TiSi_2$ at 55 ^oC in water (on-off-on-off). Purple and orange dash lines represent turning off or on the lamp, respectively.

Since the H_2 generation did not cease with the lamp turned off, long-time reactions were carried out under visible light and in the dark. To make the reaction quicker, a higher temperature of 80 ^oC was employed in line with the literature.[74] As shown in Fig. 3.5, under constant irradiation of visible light for 75 h, 998.4 μmol H_2 was collected, less than half of the catalytic amount (2360 μmol).[74] The same experiment was done in the dark for comparison. The amount generated in the dark was about 1/10 of that under

visible light. The result indicates that light plays a key role in the H_2 generation and photoactivity is involved in the reaction. However, on the basis of these results it remains unsure whether it is photocatalysis or photocorrosion. Herein photocorrosion refers to the phenomenon that material used for photocatalysis is irreversibly degraded, activated by irradiance.

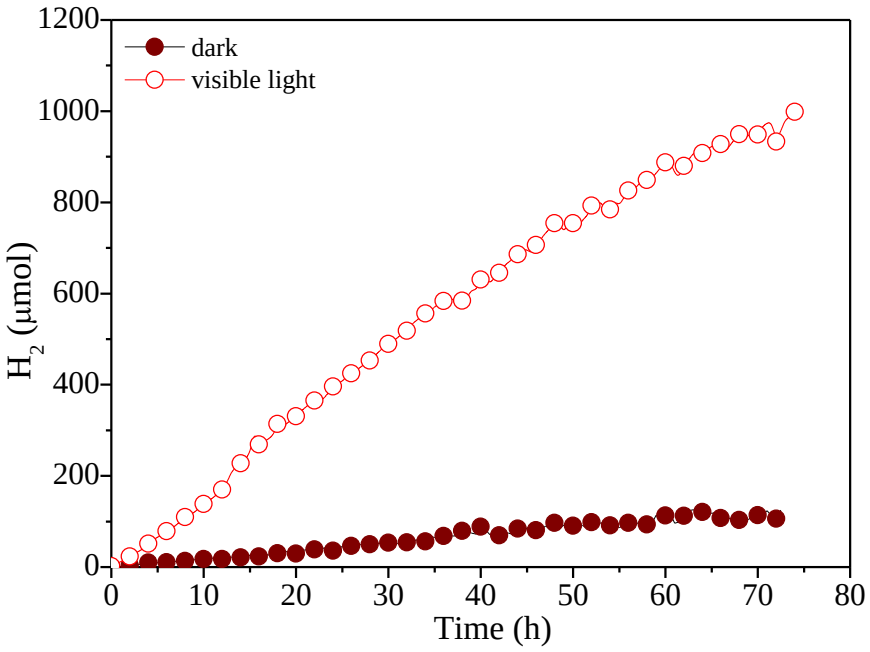

Figure 3.5: The amount of H_2 generated at 80 ^{o}C in water under visible light in 75 h and dark in 72 h.

To compare our result with Demuth's experiment (Table 3.1), similar amount of H_2 was generated in 72 h. However, the amount of catalyst used in Demuth's experiment is ambiguous. In their literature, they said they used 2 g $TiSi_2$ and then wrote: "The relatively large amount of $TiSi_2$ is chosen to provide for sufficient oxygen storage during irradiation. For catalytic purposes alone, 3.5% of this amount is sufficient."[74] It becomes confusing how much $TiSi_2$ were used in the photocatalysis reaction shown in Fig. 3.2. The vast majority of reactions in this report are not run for times giving substoimetric amounts of hydrogen. If the H_2 was generated from 2 g catalyst, their total yield (130 mL) is far less than the catalytic amount (theoretical H_2 yield calculated using Equation 3.1), which cannot prove it is photocatalytic. It is more

reasonable for 70 mg (3.5%) to be the employed amount, rather than 2 g, because it is similar with our production in 75 h and the total yield just exceeds the catalytic amount (4.03 mmol) if 70 mg $TiSi_2$ was used. If 2 g catalyst were used, there is a possibility that given long enough time to carry on the reaction, the yield would eventually exceed the catalytic amount. However, it is shown that 800 hours were occupied in Demuth's experiment. If this was the only way to prove it, it would indicate that $TiSi_2$ is not an efficient photocatalyst and is not worth investigation.

Table 3.1 Comparison between Demuth's and H_2 evolution experiment in this thesis.

	Demuth's experiment	Our experiment
H_2 evolution after 75 h	Estimated 0.89-1.34 mmol (20-30 mL)	0.998 mmol
Irradiance	Unknown (halogen light)	1 W/cm^{-2} (xenon lamp)
Amount of catalyst	2 g or 70 mg	40 mg
Catalytic amount	115.34 mmol (2 g $TiSi_2$) or 4.03 mmol (70 mg $TiSi_2$)	2.36 (mmol)
Total yield	5 mmol (130 mL)	0.998

Considering that the rate can be increased by increasing the photocatalyst amount, 150 mg $TiSi_2$ was used for the photocatalytic reaction. The configuration was changed for this reaction. Instead of analysing the yield by GC, an upside-down burette was put in a water channel to collect H_2 directly (Fig. 3.6). Fig. 3.7 shows the amount of H_2 generated in visible light at 80 ^oC in water using this system. As can be seen from the graph, H_2 was generated quickly in the first 30 min, and then levelled off at around 20 mL. The reaction ceased after the 15^{th} hour. In this reaction, the yield was still far less than the catalytic amount, which made it more doubtful whether $TiSi_2$ is a photocatalyst.

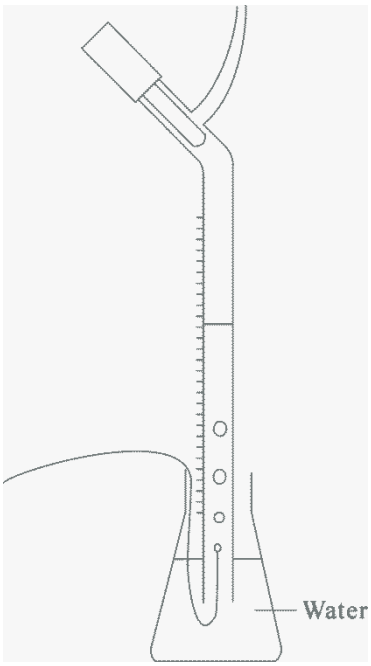

Figure 3.6: The set-up diagram consisting of burette and a tube.

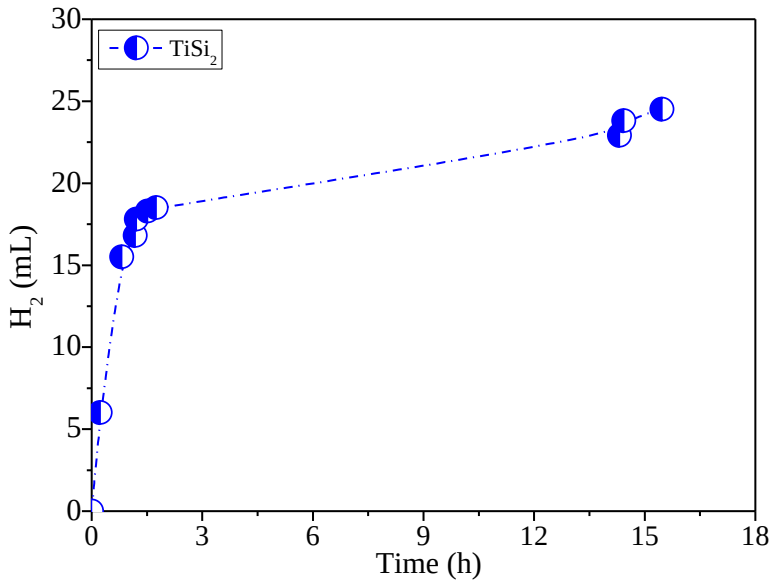

Figure 3.7: The amount of H_2 generated in visible light at 80 ^oC in water (150 mg $TiSi_2$). To measure the gas by calculating the volume, gas was collected in an upside down burette (Fig. 3.6).

3.3 Other Characterisations of Metal Silicides

Some other characterisations were tested, such as the diffuse reflectance and absorbance of some metal silicides, and short-time photoactivity of $TiSi_2$ and $ZrSi_2$ under UV or visible light.

In order to test the absorbance capacity of different silicides, the band gap of these materials were measured by diffuse reflectance and absorbance in this project. Fig. 3.8 shows the diffuse reflectance and absorbance spectrum of the silicides. As shown in the graph, these materials can absorb light within the range of visible light, which is in accordance with the literature.[74] Among them, $ZrSi_2$ and $TiSi_2$ exhibit the best absorbance, followed by $MoSi_2$, $TaSi_2$, and Ni_2Si.

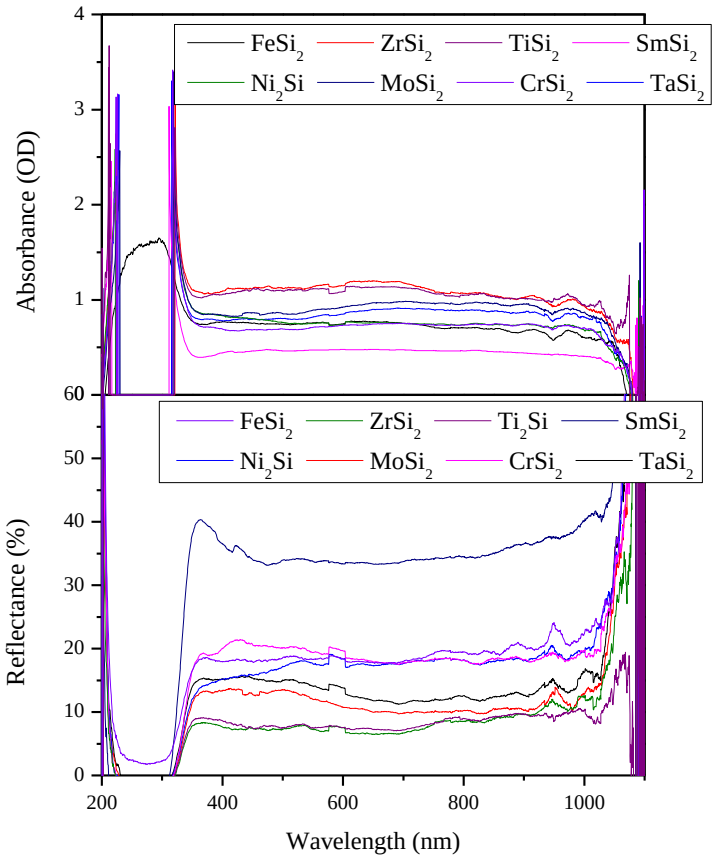

Figure 3.8: UV-vis diffuse reflectance and absorbance spectra of the silicides.

Fig. 3.9 shows the amount of H_2 generated from $ZrSi_2$ at 55 ^oC in water. In the first 15 hours the reaction was run under visible light, and then in the dark. It is obvious to see the rate declined after the lamp was turned off, showing the same trend with $TiSi_2$. Besides, it should be noted that $ZrSi_2$ can also generate considerable amount of H_2, even higher than $TiSi_2$, but again only in substoichiometric quantities.

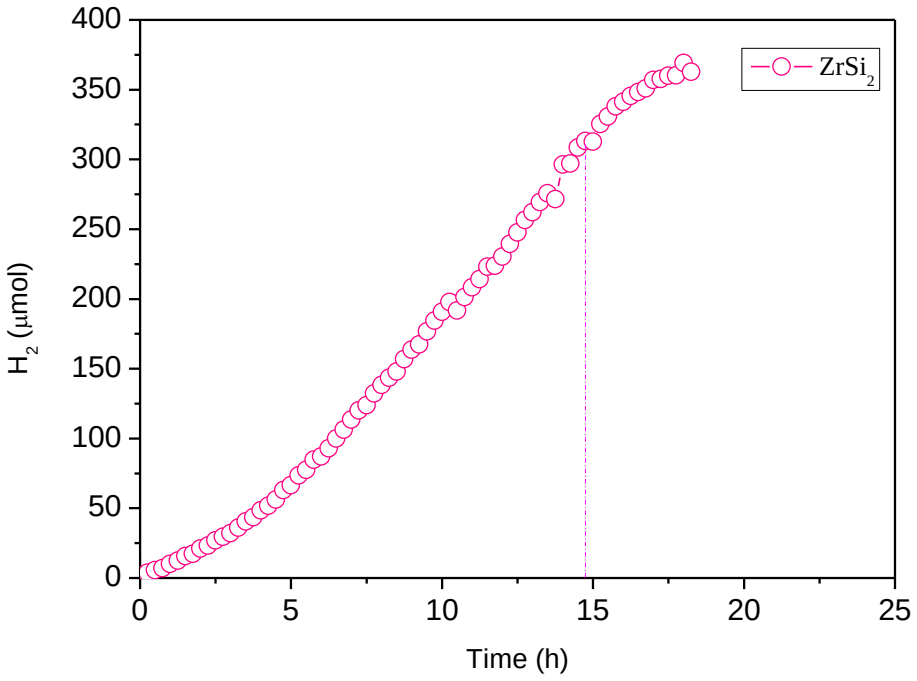

Figure 3.9: The amount of H_2 generated by $ZrSi_2$ at 55 ^oC in water (on-off). Purple dash line represents turning off the lamp.

Conclusions and Future Work

Chapter 4

Bulk C_xN_y, C_xN_y/Mac-SiO_2 and C_xN_y/Mac-ZrO_2 composites have been synthesised. Heating cyanamide to 550 ^oC for 4 h is the optimised method to synthesise bulk C_xN_y and coat C_xN_y onto macroporous materials. The "g-C_3N_4" made in this thesis are actually C_2N_3H, which is close to Liebig's "melon" and is commonly referred to as g-C_3N_4. The C/N ratio and NMR spectra of C_xN_y/Mac-SiO_2 are similar to those of C_xN_y, suggesting that the composition of C_xN_y is the same with bulk C_xN_y made in this thesis. The structural motif is tri-s-triazine but the extended planar structure is not rigorously defined.

Electron microscopy methods (TEM and EELS) show that C_xN_y sheets are present at the surface and throughout the macroporous structure and that the coverage is not homogeneous. The photonic stop band of Mac-SiO_2 indicates that above ca. 10 wt % C_xN_y/Mac-SiO_2 degrades the photonic properties and supports the conclusion that coating is heterogeneous. SEM and PXRD of samples loaded above ca. 10 wt % C_xN_y/Mac-SiO_2 also show some potential blocking of the macropores and structural features indicative of layers of C_xN_y similar to bulk C_xN_y.

For Mac-SiO_2 addition of C_xN_y shows a significant reduction in surface area, whereas Mac-ZrO_2 shows a slight increase at lower C_xN_y loadings, which is reflective of the structure and porosity of the walls of the macroporous structure.

Photocatalysis using a triethanolamine as a sacrificial reductant shows that for the composite materials, considerable H_2 evolution is obtained even for very low loadings. For example, after 5 h 6.6% C_xN_y/Mac-SiO_2 exhibits photocatalytic acitivity, 20 times

greater than the corresponding control using bulk C_xN_y. The activity per gram of active catalyst is 2.6 mmol g^{-1} h^{-1}, which compares to 1 mmol g^{-1} h^{-1} and 4.6 mmol g^{-1} h^{-1}, for mesoporous and macroporous "g-C_3N_4", respectively.[58, 59] TEM and SEM of the catalyst after reaction indicates that significant degradation has not occurred.

Further work should include some further characterisation, such as XPS. Due to the time limit, characterisation of C_xN_y/Mac-ZrO_2 composites is incomplete, especially for the H_2 evolution. The photocatalytic reactions require repetition and refinement of the experimental set-up may be required to reduce solvent loss or alternatively run reactions for less than 5 h multiple times. Different methods of deposition could also be attempted in order to achieve a homogeneous coating.

In addition, the relationship between the photonic properties and H_2 evolution could be investigated. Only one size of Mac-SiO_2 materials was used in this thesis. Since the size of the macropore can be tuned by changing the size of the template, C_xN_y/Mac-SiO_2 with different sizes of macropores should be tested to match the stop band position with the band gap of C_xN_y.

We have also shown that under our conditions $TiSi_2$ is not a photocatalyst for water splitting under visible light. Hydrogen is produced on photolysis, but substoichiometric hydrogen production under a variety of conditions strongly suggests photocorrosion and not photocatalysis. All the authors of the lead reference were contacted by email or postal mail. Authors responsible for the physical characterisation methods responded with information relevant only to characterisation of the $TiSi_2$ material. The authors responsible for the catalytic reactions did not respond.

Experimental

Chapter 5

5.1 Materials and Reagents

Cyanamide, dicyandiamide, melamine, 99.9% tetraethyl orthosilicate, 99.9% chloroplatinic acid hydrate, zirconium acetate solution were supplied by Sigma Aldrich. Titanium silicide, zirconium silicide, nickel silicide, chromium silicide were supplied by ESPI Metals. Tantalum silicide, samarium silicide, molybdenum silicide, iron silicide were supplied by Strem Chemicals. All chemicals were used as received.

5.2 Characterisation Methods

Powder X-ray Diffraction (PXRD)

Bulk C_xN_y and C_xN_y/Mac-SiO_2 composites were analysed using a Bruker-AXS D8 Advance instrument fitted with a Lynxeye detector. Cu Kα radiation (λ=1.5406 Å) is used to acquire the data between 10 and 35° 2θ, with an increment 0.02 time per step 2θ.

Fourier Transform Infrared Spectroscopy (FT-IR)

FT-IR spectra were measured on a Thermo Nicolet Avatar 370 FT-IR with a desiccant air dryer to remove CO_2. KBr was used to disperse the sample and the mixture was pressed into a 13mm disk using a hydraulic press.

Diffuse Reflectance UV-Vis Spectroscopy (DRUVS)

The diffuse reflectance and absorbance spectra were obtained using an Ocean Optic Inc. HR2000+ High Resolution Spectrometer, with scan average of 10, boxcar width of 30. The light sources are Helium and Deuterium lamps by Photonic Solutions Ltd.

DH-2000-BAL.

Scanning Electron Microscopy (SEM)

SEM images were acquired on a FEI Sirion scanning electron microscope, fitted with an EDAX Phoenix EDS X-ray spectrometer. Powdered samples were put on an adhesive carbon tape mounted on an aluminium stub.

Transmission Electron Microscopy (TEM)

TEM images were obtained from JEOL JEM-2010 transmission electron microscope, with 200kV ultrahigh resolution analytical electron microscope. Small amounts of samples were dispersed in methanol. After grounding for 1 min, the solutions were sonicated for 5 min. 4 or 5 drops were added to a copper grid and dried in air.

Electron Energy Loss Spectroscopy (EELS, Elemental Mapping)

Elemental mapping was performed at the Institute of Materials Research, University of Leeds.

Nuclear Magnetic Resonance Spectroscopy (NMR)

Solid state NMR data was acquired at the EPSRC National Solid-State NMR service at Durham.

Brunauer-Emmett-Teller (BET) Surface Area Measurement

Surface area values of the samples were measured using a Micromeritics Tristar 3000 from the nitrogen adsorption isotherm. The samples were pre-dried under nitrogen for 6 hours.

Photocatalysis Equipment

The apparatus used for photoreaction and analysis of products has been described

previously.[75] Reactions were performed in a solution of water and triethanolamine in 1:9 vol % and the apparatus maintained at a temperature of 40 ^{o}C. Illumination was performed using a 300 W Xe lamp fitted with a 15 cm IR filter and a wideband $AlMgF_2$ coated mirror followed by a 400 nm long band pass filter. Gas analysis was performed using a Shimadzu Corporation GC. Gases were separated on a 25 cm long column packed with 5 Å molecular sieves and detection was performed using a thermal conductivity detector (TCD). The gas samples were analyzed using the following conditions; 20 mL/min flow rate of Ar gas, 90 ^{o}C column temperature and 120 ^{o}C detector temperature. Under these conditions the retention time of H_2 is 1.5 min, O_2 2.5 min and N_2 3 min.

The GC system is shown in Fig. 5.1.

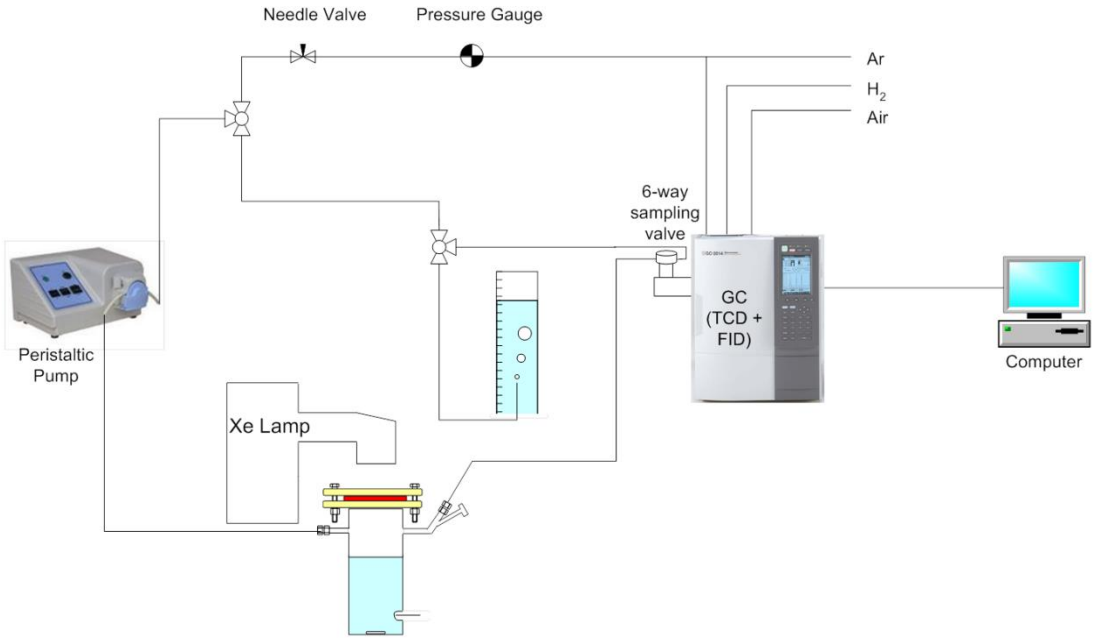

Figure 5.1: GC system of photocatalytic H_2 evolution.

5.3 Materials Synthesis

5.3.1 Macroporous SiO_2 and ZrO_2

A colloidal templating method was used to synthesis macroporous SiO_2 and ZrO_2

according to a literature report.[64] Polystyrene emulsion was centrifuged at 4.0 krpm for 4 h, and the solid was dried at 50 ^{o}C in air. Then the polystyrene was crushed into granules. 1 g polystyrene granules were put into a Size 3 sinter funnel and mixed with 20 mL ethanol for 30 min.

For Mac-SiO_2, the precursor solution was mixed with 3 mL tetraethyl orthosilicate (TEOS), 2 mL ethanol, 1.5 mL deionized water and 0.5 mL 1 M hydrochloric acid with vigorous stirring. When the solution became clear and cool, it was ready to add the precursor to polystyrene. Before that, the ethanol in the sinter funnel was removed by vacuum. The precursor solution was added around the edge of sinter funnel slowly and gently. After soaking for 1 h, the solution was removed by vacuum and the solid was dried overnight. Finally, the solid was transferred to an alumina crucible and calcined at 550 ^{o}C for 10 h, with a heating rate of 1^{o}C/min.

With regard to Mac-ZrO_2, the precursor solution was mixed with 3 mL zirconium acetate solution and 3 mL methanol. And the final mixture was heated to 450 ^{o}C for 4 h, with a heating rate of 1 ^{o}C/min.

5.3.2 Bulk C_xN_y

150 mg cyanamide and dicyandiamide were put in two 2 mL glass vials, respectively, and heated to 550 ^{o}C for 4 h with a heating rate of 2.3 ^{o}C/min, with a flow of nitrogen. To optimise the calcination condition, cyanamide was heated to 600 and 650 ^{o}C, and in another case cyanamide was heated to 550 ^{o}C ~~dwelling~~ for a further 10 h. The samples after cooling were orange and yellow chunks (from CA and DCDA, respectively). The chunks were ground into powders in acetone for characterisation. The yield is 53.3% by mass.

5.3.3 Coating C_xN_y onto Mac-SiO_2 and Mac-ZrO_2

Cyanamide was weighed in a 2 mL glass vial and dissolved in 2 mL ethanol and the

precursor solution was added to a 10 mL glass vial containing macroporous materials. After the solvent was evaporated, the mixture was heated to 550 ^{o}C for 4 h, with a heating rate of 2.3 ^{o}C/min. The amounts of raw materials were shown in Table 5.1.

Table 5.1: The amount of raw materials corresponding to the final C_xN_y content in this thesis

Composites	Name/ C_xN_y content	Cyanamide (mg)	Macroporous materials (mg)
C_xN_y /Mac-SiO_2	S0 / 0%	20	120
	S1 / 6.6%	40	120
	S2 / 12.8%	52.5	90
	S3 / 28.2%	90	90
	0%	5	15
	2.2%	10	30
	6.6%	15	30
	12.1%	20	30
	15.4%	80	120
	47.5%	40	15
C_xN_y /Mac-ZrO_2	Z1 / 3.6%	30	90
	Z2 / 22.7%	75	90

5.4 Deposition of Pt Cocatalyst

3 wt % Pt was deposited onto C_xN_y and its composites (3 wt % Pt relative to mass of C_xN_y contents). The C_xN_y contents in these composites were determined according to the elemental analysis (see Table 2.5). Chloroplatinic acid hydrate (H_2PtCl_6•n H_2O) was chosen as the Pt deposition precursor. The precursor was weighed in a 10 mL vial under nitrogen and dissolved in 2 mL deionized water. After the sample was added into the solution, the mixture was heated to 90 ^{o}C until the solvent was evaporated.

The dried sample was then heated to 200 ^{o}C for 1 h, with a heating rate of 1 ^{o}C/min under a flow of hydrogen with a rate of 60 mL/min.

Appendices

Appendix A Raw materials of C_xN_y/Mac-SiO_2 and C_xN_y/Mac-ZrO_2

Appendix B PXRD pattern of the aluminium sample holder used in this thesis

Appendix C UV-vis diffuse reflectance spectra of C_xN_y/Mac-SiO_2

Appendix D Calculation of size distribution of Pt nanoparticles on C_xN_y/Mac-SiO_2 (S1)

Appendix E BET surface area measurement

Appendix A

The amount of raw materials corresponding to the final C_xN_y content in our experiment (Table 5.1)

Composites	Name/ C_xN_y content	Cyanamide (mg)	Macroporous materials (mg)
C_xN_y /Mac-SiO_2	S0 / 0%	20	120
	S1 / 6.6%	40	120
	S2 / 12.8%	52.5	90
	S3 / 28.2%	90	90
	0%	5	15
	2.2%	10	30
	6.6%	15	30
	12.1%	20	30
	15.4%	80	120
	47.5%	40	15
C_xN_y /Mac-ZrO_2	Z1 / 3.6%	30	90
	Z2 / 22.7%	75	90

Appendix B

PXRD pattern of the aluminium sample holder used in this thesis.

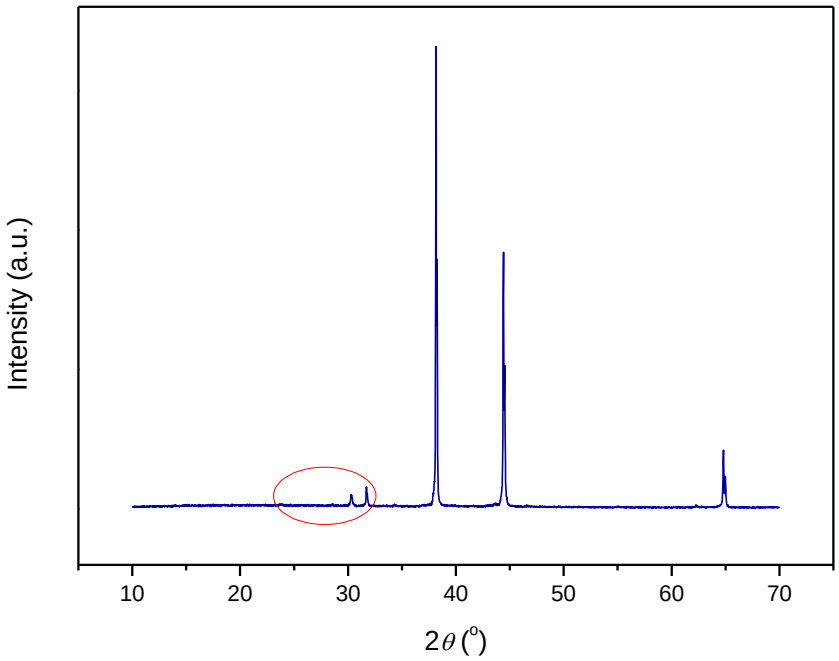

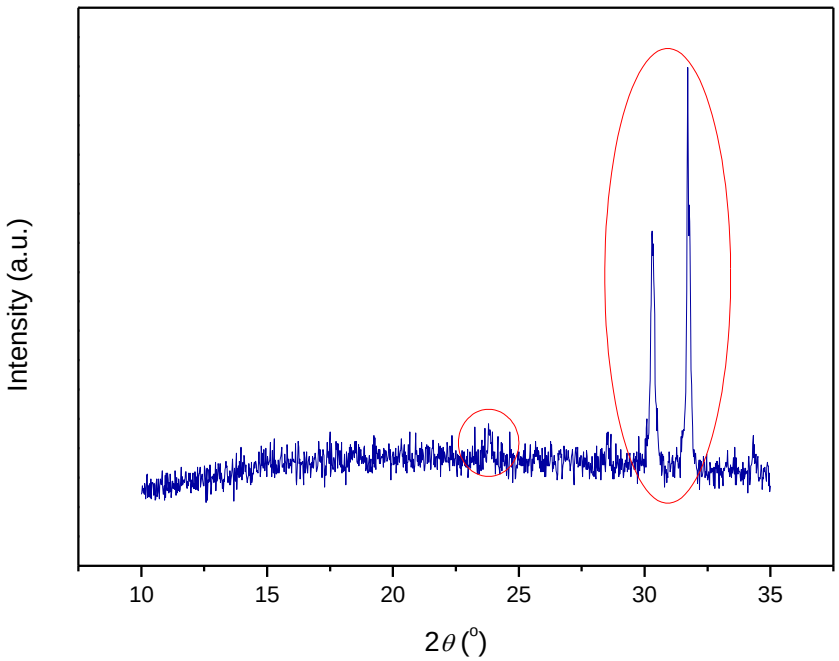

Appendix C

UV-Vis diffuse reflectance spectra of C_xN_y/Mac-SiO_2 composites (S1-S3).

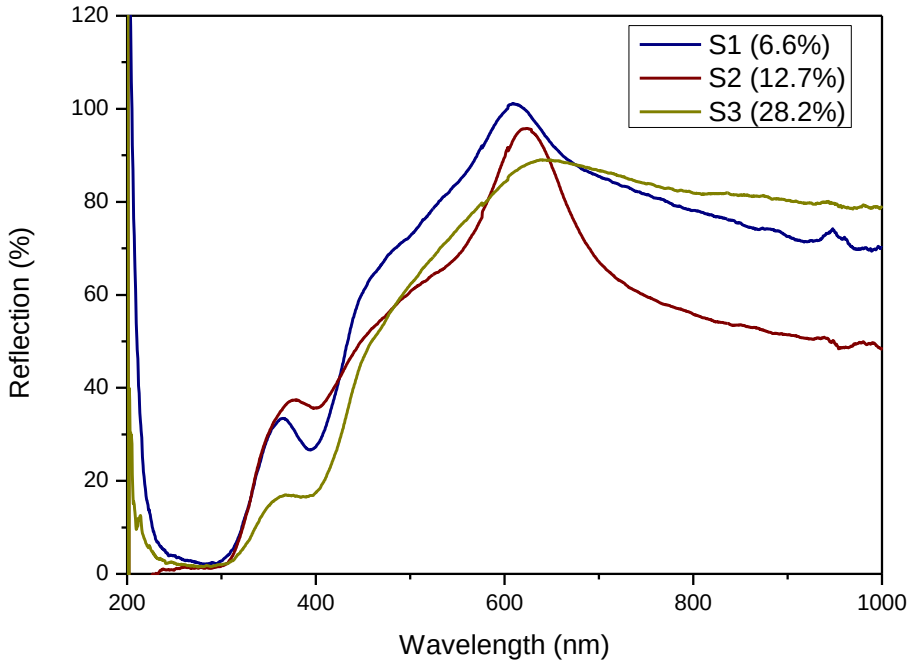

Appendix D

Calculation of size distribution of Pt nanoparticles on C_xN_y/Mac-SiO_2 (S1).

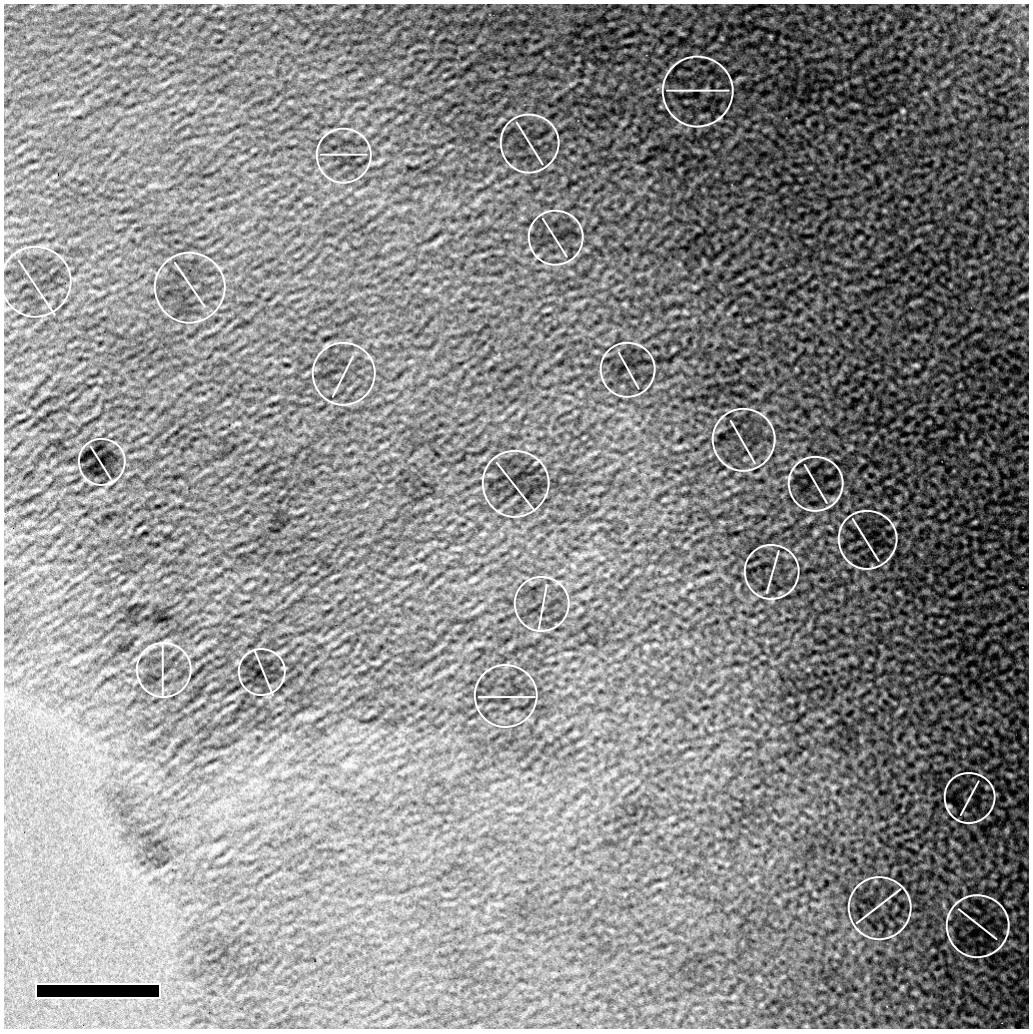

No.	Size /nm	No.	Size /nm	No.	Size /nm
1	2.621	8	1.815	15	1.954
2	2.151	9	2.1	16	1.774
3	1.858	10	1.92	17	1.764
4	1.995	11	2.473	18	1.995
5	2.504	12	1.663	19	1.554
6	1.524	13	2.262	20	2.246
7	1.806	14	1.806	21	1.956

Appendix E

BET surface area measurement nitrogen desorption and adsorption figure for Mac-SiO_2, Mac-ZrO_2, C_xN_y/Mac-SiO_2, C_xN_y/Mac-ZrO_2 and bulk C_xN_y.

Mac-SiO_2 and C_xN_y/Mac-SiO_2

Mac-SiO_2

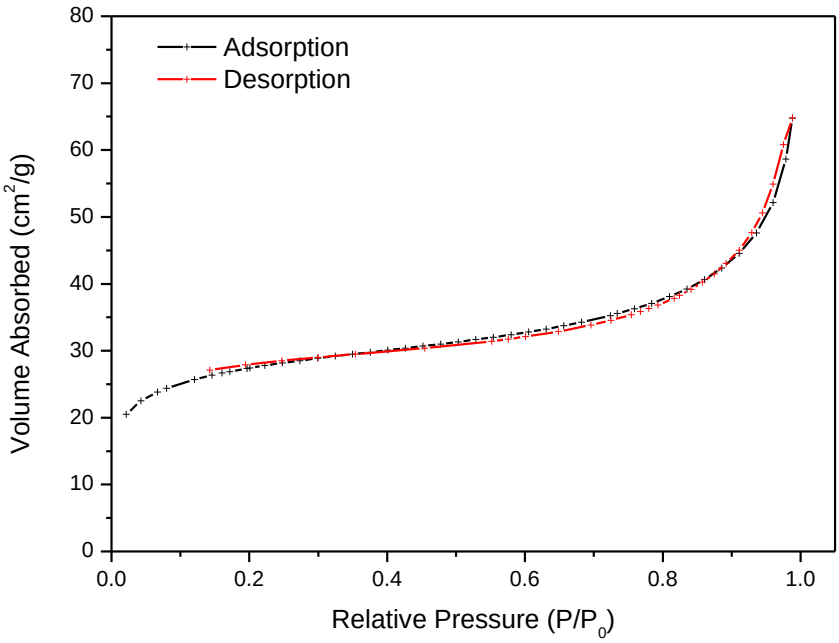

C_xN_y/Mac-SiO_2 (S1: 6.6%)

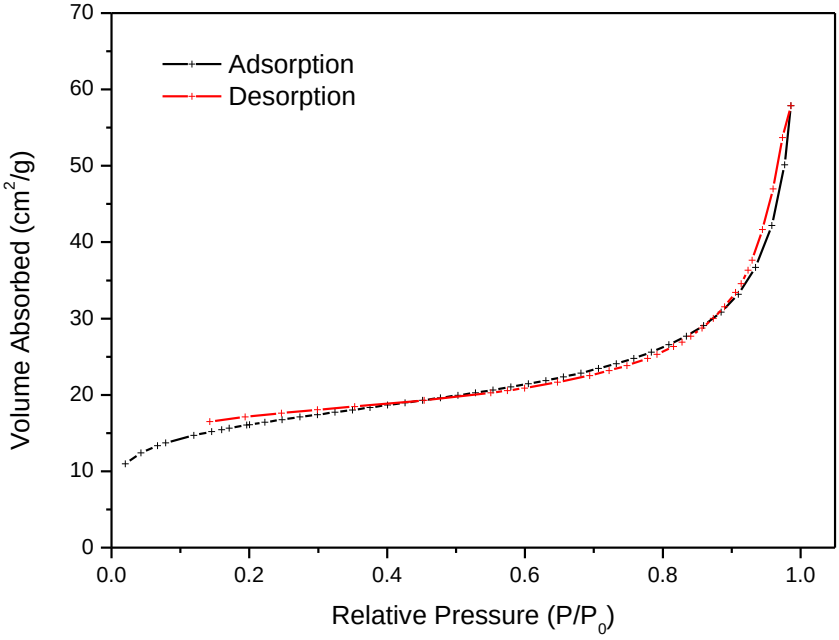

C_xN_y/Mac-SiO_2 (S2: 12.7%)

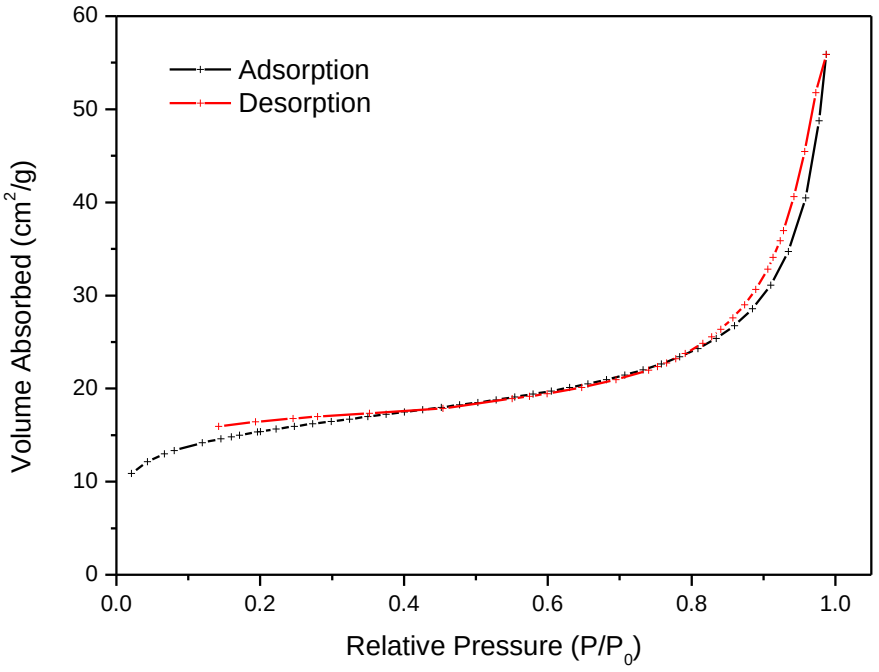

C_xN_y/Mac-SiO_2 (S3: 28.2%)

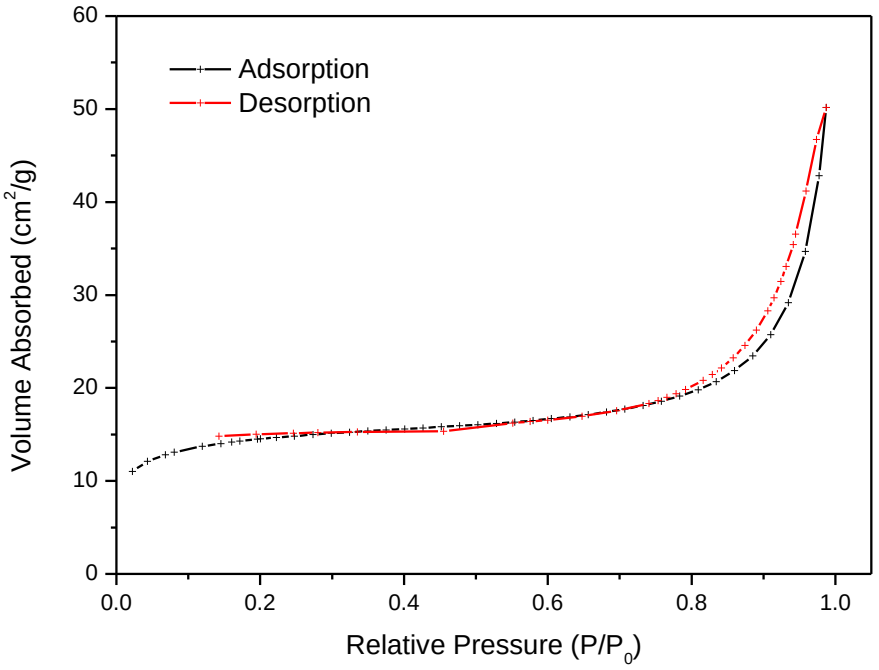

Mac-ZrO_2 and C_xN_y/Mac-ZrO_2

Mac-ZrO_2

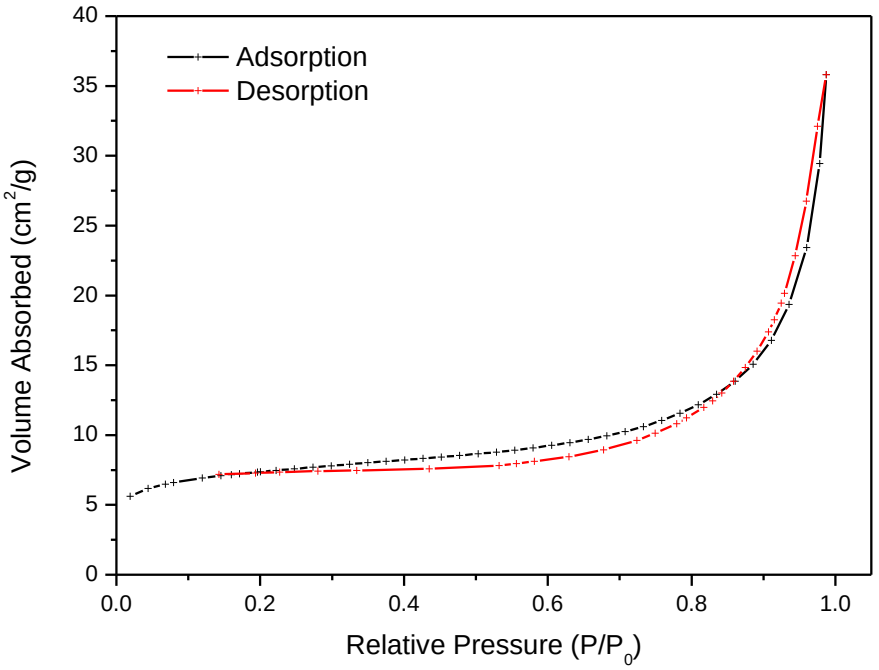

C_xN_y/Mac-ZrO_2 (Z1: 3.6%)

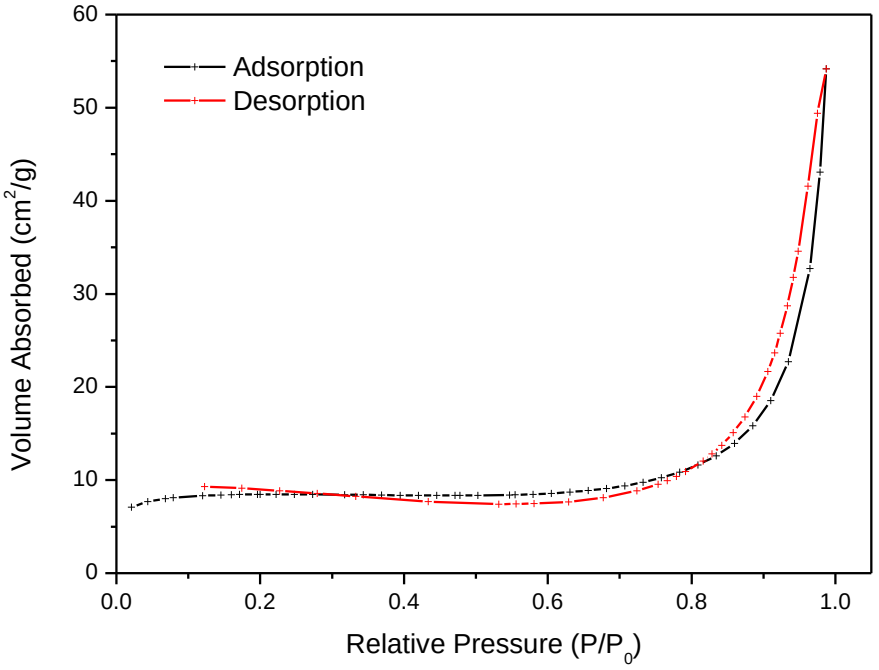

C_xN_y/Mac-SiO_2 (Z2: 22.7%)

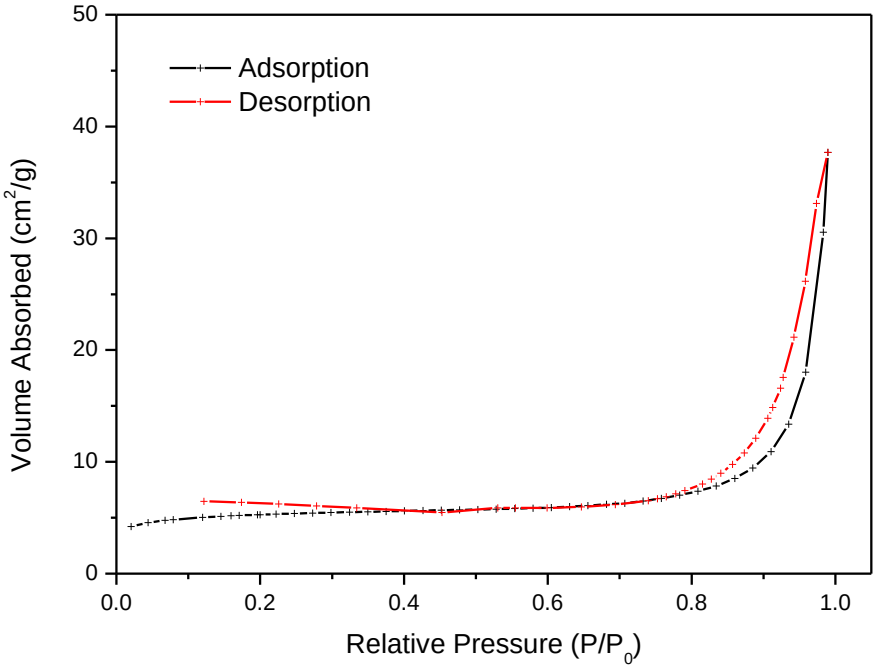

Bulk C_xN_y

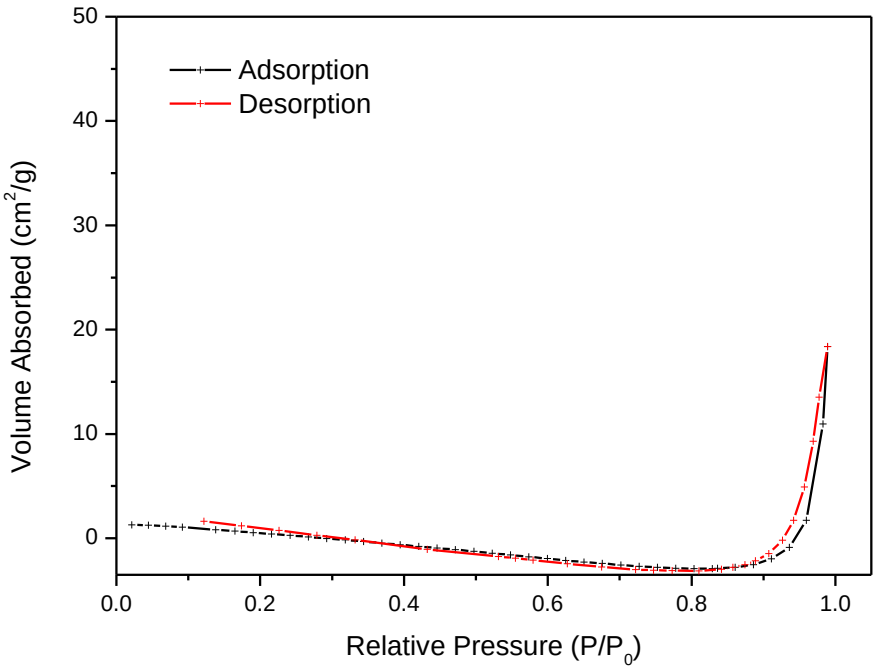

Abbreviations

3DOM= Three-dimensional Ordered Macroporous

BET= Brunauer-Emmett-Teller

CA= cyanamide

CB= conduction band

CHN= CHN combustion analyser

CNT= carbon nanotube

C_xN_y= carbon nitride synthesised in this thesis

CPMAS= cross polarisation magic angle spinning

DCDA= dicyandiamide

DRUVS= Diffuse Reflectance UV-Vis Spectroscopy

EDTA= ethylenediaminetetraacetic acid

EDX= Energy-Dispersive X-ray spectroscopy

EELS= Electron Energy Loss Spectroscopy

E_g= Band gap energy

FB= forbidden band

FT-IR= Fourier Transform Infrared Spectroscopy

GC= Gas Chromatography

g-C_3N_4= graphitic carbon nitride

Mac-SiO_2= macroporous silica

Mac-ZrO_2= macroporous zirconia

MWNT= multi-walled nanotube

NHE= Normal hydrogen electrode

NMR= Nuclear Magnetic Resonance Spectroscopy

PMMA= poly(methyl methacrylate)

PS= polystyrene

P(St-MMA-AA)= poly(styrene-methyl methacrylate-acrylic acid)

PXRD= Powder X-ray Diffraction

SEM= Scanning Electron Microscopy

SSNMR=Solid-State Nuclear Magnetic Resonance Spectroscopy

SWNT= single-walled nanotube

TCD= Thermal conductivity detector

TEA= triethanolamine

TEM= Transmission Electron Microscopy

TEOS= tetraethyl orthosilicate ($Si(OEt)_4$)

UV= ultrovoilet

UV-Vis=Ultrovoilet-Visible Spectroscopy

VB= valence band

Vis= visible light

References

1. K. R. Catchpole, M. J. McCann, K. J. Weber and A. W. Blakers, *Sol. Energ. Mat. Sol. C.*, 2001, **68**, 173-215.
2. D. Y. Bao, *Atca Energiae Solaris Sinica*, 1995, **16**, 114-120.
3. N. K. Liu, B. S. Zhu and J. S. Luo, *Semiconductor Physics*, Publishing house of electronics industry (China), 2008.
4. A. Fujishima and K. Honda, *Nature*, 1972, **238**, 37-38.
5. X. B. Chen, S. H. Shen, L. J. Guo and S. S. Mao, *Chem. Rev.*, 2010, **110**, 6503-6570.
6. A. Kudo and Y. Miseki, *Chem. Soc. Rev.*, 2009, **38**, 253-278.
7. K. Maeda, *J. Photochem. Photobiol. C-Photochem. Rev.*, 2011, **12**, 237-268.
8. W. Erbs, J. Desilvestro, E. Borgarello and M. Graetzel, *J. Phys. Chem.*, 1984, **88**, 4001-4006.
9. X. Y. Chen, T. Yu, X. X. Fan, H. T. Zhang, Z. S. Li, J. H. Ye and Z. G. Zou, *Appl. Surf. Sci.*, 2007, **253**, 8500-8506.
10. S. Karuppuchamy, H. Matsui, K. Kira, M. A. Hassan and M. Yoshihara, *Ceram. Int.*, 2012, **38**, 1515-1521.
11. T. Murase, H. Irie and K. Hashimoto, *J. Phys. Chem. B*, 2004, **108**, 15803-15807.
12. V. R. Reddy, D. W. Hwang and J. S. Lee, *Korean J. Chem. Eng.*, 2003, **20**, 1026-1029.
13. S. Yamada, A. Y. Nosaka and Y. Nosaka, *J. Electroanal. Chem.*, 2005, **585**, 105-112.
14. G. K. Mor, O. K. Varghese, M. Paulose, K. Shankar and C. A. Grimes, *Sol. Energ. Mat. Sol. C.*, 2006, **90**, 2011-2075.
15. J. S. Chen and X. W. Lou, *Electrochem. Commun.*, 2009, **11**, 2332-2335.
16. H. Arakawa and K. Sayama, *Catal. Surv. Jpn.*, 2000, **4**, 75-80.
17. J. H. Yang, H. J. Yan, X. Zong, F. Y. Wen, M. Y. Liu and C. Li, *Philos. Trans. R. Soc. A-Math. Phys. Eng. Sci.*, 2013, **371**.
18. X. C. Wang, K. Maeda, A. Thomas, K. Takanabe, G. Xin, J. M. Carlsson, K. Domen and M. Antonietti, *Nat. Mater.*, 2009, **8**, 76-80.
19. K. Maeda and K. Domen, *J. Phys. Chem. Lett.*, 2010, **1**, 2655-2661.
20. K. Maeda, K. Teramura, D. L. Lu, T. Takata, N. Saito, Y. Inoue and K. Domen, *Nature*, 2006, **440**, 295-295.
21. X. Chen and S. S. Mao, *Chem. Rev.*, 2007, **107**, 2891-2959.
22. E. Borgarello, J. Kiwi, M. Gratzel, E. Pelizzetti and M. Visca, *J. Am. Chem. Soc.*, 1982, **104**, 2996-3002.
23. H. Kato and A. Kudo, *J. Phys. Chem. B*, 2002, **106**, 5029-5034.
24. D. W. Hwang, H. G. Kirn, J. S. Lee, J. Kim, W. Li and S. H. Oh, *J. Phys. Chem. B*, 2005, **109**, 2093-2102.

25. D. H. Kim, D. K. Choi, S. J. Kim and K. S. Lee, *Catal. Commun.*, 2008, **9**, 654-657.
26. X. B. Chen and C. Burda, *J. Am. Chem. Soc.*, 2008, **130**, 5018-5019.
27. S. Iijima, *Nature*, 1991, **354**, 56-58.
28. R. H. Baughman, A. A. Zakhidov and W. A. de Heer, *Science*, 2002, **297**, 787-792.
29. Z. X. Cai and X. P. Yan, *Nanotechnology*, 2006, **17**, 4212-4216.
30. S. W. Lee and W. M. Sigmund, *Chem. Commun.*, 2003, 780-781.
31. J. M. Planeix, N. Coustel, B. Coq, V. Brotons, P. S. Kumbhar, R. Dutartre, P. Geneste, P. Bernier and P. M. Ajayan, *J. Am. Chem. Soc.*, 1994, **116**, 7935-7936.
32. B. Xue, P. Chen, Q. Hong, J. Y. Lin and K. L. Tan, *J. Mater. Chem.*, 2001, **11**, 2378-2381.
33. K. Dai, T. Y. Peng, D. N. Ke and B. Q. Wei, *Nanotechnology*, 2009, **20**.
34. K. S. Novoselov, A. K. Geim, S. V. Morozov, D. Jiang, Y. Zhang, S. V. Dubonos, I. V. Grigorieva and A. A. Firsov, *Science*, 2004, **306**, 666-669.
35. Y. S. Fu, H. Q. Chen, X. Q. Sun and X. Wang, *Appl. Catal., B*, 2012, **111**, 280-287.
36. J. W. Zhu, G. Y. Zeng, F. D. Nie, X. M. Xu, S. Chen, Q. F. Han and X. Wang, *Nanoscale*, 2010, **2**, 988-994.
37. Y. M. Li, X. J. Lv, J. Lu and J. H. Li, *J. Phys. Chem. C*, 2010, **114**, 21770-21774.
38. Q. Li, B. D. Guo, J. G. Yu, J. R. Ran, B. H. Zhang, H. J. Yan and J. R. Gong, *J. Am. Chem. Soc.*, 2011, **133**, 10878-10884.
39. Q. J. Xiang, J. G. Yu and M. Jaroniec, *J. Am. Chem. Soc.*, 2012, **134**, 6575-6578.
40. Y. Zheng, J. Liu, J. Liang, M. Jaroniec and S. Z. Qiao, *Energy Environ. Sci.*, 2012, **5**, 6717-6731.
41. J. S. Zhang, J. H. Sun, K. Maeda, K. Domen, P. Liu, M. Antonietti, X. Z. Fu and X. C. Wang, *Energy Environ. Sci.*, 2011, **4**, 675-678.
42. Y. J. Cui, Z. X. Ding, P. Liu, M. Antonietti, X. Z. Fu and X. C. Wang, *Phys. Chem. Chem. Phys.*, 2012, **14**, 1455-1462.
43. J. V. Liebig, *Ann. Pharm*, 1834, **10**.
44. A. Thomas, A. Fischer, F. Goettmann, M. Antonietti, J. O. Muller, R. Schlogl and J. M. Carlsson, *J. Mater. Chem.*, 2008, **18**, 4893-4908.
45. F. Goettmann, A. Fischer, M. Antonietti and A. Thomas, *New J. Chem.*, 2007, **31**, 1455-1460.
46. M. J. Bojdys, J. O. Muller, M. Antonietti and A. Thomas, *Chem. Eur. J.*, 2008, **14**, 8177-8182.
47. Y. C. Zhao, D. L. Yu, H. W. Zhou, Y. J. Tian and O. Yanagisawa, *J. Mater. Sci.*, 2005, **40**, 2645-2647.
48. B. V. Lotsch, M. Doblinger, J. Sehnert, L. Seyfarth, J. Senker, O. Oeckler and W. Schnick, *Chem. Eur. J.*, 2007, **13**, 4969-4980.
49. H. J. Yan, *Chem. Commun.*, 2012, **48**, 3430-3432.
50. C. E. Redemann and H. J. Lucas, *J. Am. Chem. Soc.*, 1940, **62**, 842-846.

51. S. B. Yang, Y. J. Gong, J. S. Zhang, L. Zhan, L. L. Ma, Z. Y. Fang, R. Vajtai, X. C. Wang and P. M. Ajayan, *Adv. Mater.*, 2013, **25**, 2452-2456.
52. A. Corma, *Chem. Rev.*, 1997, **97**, 2373-2419.
53. M. E. Davis, *Nature*, 2002, **417**, 813-821.
54. S. Hwang, S. Lee and J. S. Yu, *Appl. Surf. Sci.*, 2007, **253**, 5656-5659.
55. Y. S. Jun, W. H. Hong, M. Antonietti and A. Thomas, *Adv. Mater.*, 2009, **21**, 4270-4274.
56. M. Groenewolt and M. Antonietti, *Adv. Mater.*, 2005, **17**, 1789-1792.
57. E. Z. Lee, Y. S. Jun, W. H. Hong, A. Thomas and M. M. Jin, *Angew. Chem. Int. Edit.*, 2010, **49**, 9706-9710.
58. X. F. Chen, Y. S. Jun, K. Takanabe, K. Maeda, K. Domen, X. Z. Fu, M. Antonietti and X. C. Wang, *Chem. Mater.*, 2009, **21**, 4093-4095.
59. Y.-S. Jun, J. Park, S. U. Lee, A. Thomas, W. H. Hong and G. D. Stucky, *Angew. Chem. Int. Edit.*, 2013, **52**, 11083-11087.
60. X. C. Wang, X. F. Chen, A. Thomas, X. Z. Fu and M. Antonietti, *Adv. Mater.*, 2009, **21**, 1609-1612.
61. X. F. Chen, J. S. Zhang, X. Z. Fu, M. Antonietti and X. C. Wang, *J. Am. Chem. Soc.*, 2009, **131**, 11658-11659.
62. Q. J. Xiang, J. G. Yu and M. Jaroniec, *J. Phys. Chem. C*, 2011, **115**, 7355-7363.
63. L. Ge, F. Zuo, J. K. Liu, Q. Ma, C. Wang, D. Z. Sun, L. Bartels and P. Y. Feng, *J. Phys. Chem. C*, 2012, **116**, 13708-13714.
64. R. C. Schroden, M. Al-Daous, C. F. Blanford and A. Stein, *Chem. Mater.*, 2002, **14**, 3305-3315.
65. A. Stein, B. E. Wilson and S. G. Rudisill, *Chem. Soc. Rev.*, 2013, **42**, 2763-2803.
66. C. W. Cheng, S. K. Karuturi, L. J. Liu, J. P. Liu, H. X. Li, L. T. Su, A. I. Y. Tok and H. J. Fan, *Small*, 2012, **8**, 37-42.
67. A. Stein, F. Li and N. R. Denny, *Chem. Mater.*, 2008, **20**, 649-666.
68. L. Ge, *Mater. Lett.*, 2011, **65**, 2652-2654.
69. A. B. Jorge, D. J. Martin, M. T. S. Dhanoa, A. S. Rahman, N. Makwana, J. W. Tang, A. Sella, F. Cora, S. Firth, J. A. Darr and P. F. McMillan, *J. Phys. Chem. C*, 2013, **117**, 7178-7185.
70. S. C. Yan, Z. S. Li and Z. G. Zou, *Langmuir*, 2009, **25**, 10397-10401.
71. B. T. Holland, C. F. Blanford, T. Do and A. Stein, *Chem. Mater.*, 1999, **11**, 795-805.
72. W. Bensch and W. Bergholz, *Semicond. Sci. Technol.*, 1990, **5**, 421-428.
73. A. Y. Jeong, S. M. Goo and D. P. Kim, *J. Sol-Gel Sci. Technol.*, 2000, **19**, 483-487.
74. P. Ritterskamp, A. Kuklya, M. A. Wustkamp, K. Kerpen, C. Weidenthaler and M. Demuth, *Angew. Chem. Int. Edit.*, 2007, **46**, 7770-7774.
75. N. S. Hondow, Y. H. Chou, K. Sader, R. Brydson and R. E. Douthwaite, *J. Phys. Chem. C*, 2010, **114**, 22758-22762.